UNIVERSITY OF CALIFORNIA, SAN DIEGO

Airborne Observations and Numerical Modeling of Fetch-Limited Waves in the Gulf of Tehuantepec

A dissertation submitted in partial satisfaction of the
requirements for the degree Doctor of Philosophy
in
Oceanography

by

Leonel Romero

Committee in charge:

Professor W. Kendall Melville, Chair
Professor Charles Cox
Professor Robert T. Guza
Professor Walter Munk
Professor Sutanu Sarkar
Lecturer Eric Terrill

2008

The dissertation of Leonel Romero is approved, and it is acceptable in quality and form for publication on microfilm:

_____

_____

_____

_____

_____

_____

Chair

University of California, San Diego

2008

DEDICATION

This work is dedicated to my parents, Elisa Gonzalez Avalos and Leonel Romero Echevarria.

TABLE OF CONTENTS

LIST OF FIGURES

LIST OF TABLES

ACKNOWLEDGMENTS

I would like to thank Sarah Gille for her guidance during my early stages as research assistant at Scripps. I would like to thank my thesis advisor Ken Melville for his guidance and support during the course of my thesis work. I am particularly grateful for having the opportunity to participate in the field experiment in Mexico. I am also grateful for having the opportunity to interact with and learn from from Walter Munk and Chip Cox, both of whom share a special interest in surface waves.

We acknowledge the collaboration of Carl A. Friehe, and Djamal Khelif at the University of California, Irvine, in planning and conducting the GOTEX experiments. We are grateful to Allen Schanot, Henry Boynton, Lowell Genzlinger, Ed Ringleman, and the support staff at the NCAR Research Aviation Facility. We would like to thank Bill Krabill, Bob Swift, Jim Yungel, John Sonntag and Robbie Russell at NASA/EG&G, for access to the ATM, its deployment and initial data processing. We acknowledge the collaboration of Graciella Raga, Darrel Baumgardner and students from the 'Universidad Nacional Autonoma de Mexico'. We thank the management and staff at the Huatulco airport for their support during the field experiment. We acknowledge the assistance of Jim Lasswell, and Axel Pierson at Scripps Institution of Oceanography in preparing equipment and logistical support during the field experiments. L.R. is grateful to Jessica Kleiss for fruitful discussions during the analysis of the data. We are thankful to Paul Hwang for useful comments and suggestions on the data analysis procedures before the field campaign. We thank Terri Paluszkiewicz whose encouragement and support was critical in making this research possible.

We thank Bruce Cournuelle and Caroline Papadopoulos for allowing us to carry out the simulations on the computer cluster at Scripps Institution of Oceanography. LR is thankful to Jose Henrique Alves for useful suggestions on the choice of numerical framework for the simulations. LR is thankful to Jessica M. Kleiss for her comments on this manuscript. This work was supported by grants

to WKM from the National Science Foundation, the Office of Naval Research, and BP.

VITA

2002	B.S., Physics, University of California, San diego
2001–2008	Research Assistant Scripps Institution of Oceanography, University of California, San Diego
2008	Ph.D., Physical Oceanography Scripps Institution of Oceanography, University of California, San Diego.

FIELDS OF STUDY

Studies in Applied Mathematics
Professors S. G. Llewellyn-Smith, F. A. Williams, and W. R. Young

Studies in Data Analysis
Professors R. Pinkel and S. T. Gille

Studies in Fluid Dynamics
Professors P. Cessi, R. Salmon, S. Sarkar, C. D. Winant, and T. Bewley

Studies in Physical Oceanography
Professors P. Robbins, D. Roemmich, and L. D. Talley

Studies in Waves
Professors R. T. Guza, M. C. Hendershott, and W. K. Melville

ABSTRACT OF THE DISSERTATION

Airborne Observations and Numerical Modeling of Fetch-Limited Waves in the Gulf of Tehuantepec

by

Leonel Romero
Doctor of Philosophy in Oceanography
University of California, San Diego, 2008
Professor W. Kendall Melville, Chair

We present airborne observations of fetch-limited waves generated during strong offshore winds, ranging between 10 and 25 m s^{-1}, in the Gulf of Tehuantepec. The measurements were collected over a wide range of fetches, from young to fully-developed seas, and include one- and two-dimensional wavenumber spectra, wind velocities, and atmospheric turbulent fluxes. The observed evolution of the wave field is compared to numerical simulations using a recently proposed wave dissipation formulation. In particular, we compare the observed and computed evolution of the directional spectra for fetch-limited conditions under realistic wind forcing. The thesis is composed of two main chapters, both of which are self contained and can be read independently of one another. The first chapter focuses on the analysis of the wind and wave measurements collected in the Gulf of Tehuantepec during February, 2004. It provides a description of the environmental conditions, the instrumentation, as well as the techniques used in the analysis for the characterization of the wind-wave spectrum with respect the wave age or fetch. The results are discussed in the context of previous observations and current numerical wind-wave prediction models. The second chapter describes the comparison of the measured wavenumber spectra with numerical simulations using state-of-the-art wind-wave models. It provides general background information on the physics and

the development of numerical wind-wave models. The model is first implemented and tested under the idealized conditions of spectral evolution in one spatial direction with stationary uniform winds. The two-dimensional simulations are carried out over the Gulf of Tehuantepec for two research flights with the assumed steady wind forcing based on the airborne wind measurements, QuikSCAT scatterometer winds, and reanalysis model winds from NCEP/NARR. The computed wave spectra are directly compared to the airborne observations over a wide range of wave ages. The comparison between the observations and the numerical simulations highlights some of the issues associated with the source term balance in the tail of the spectrum. The performance of the model suggests that the Alves and Banner (2003) dissipation is a good first step for realistic simulations of the wind-wave spectrum. The possible reasons for differences between the measurements and the simulations are discussed.

I

Airborne Observations of Fetch-Limited Waves in The Gulf of Tehuantepec

I.1 Abstract

We present airborne observations of fetch-limited waves generated during strong offshore winds, ranging between 10 and 25 m s^{-1}, in the Gulf of Tehuantepec. The measurements were collected over a wide range of fetches, from young to fully-developed seas, and include one- and two-dimensional wavenumber spectra, wind velocities, and turbulent fluxes. The evolution of the standard integral parameters of the spectrum, the spectral peak wavenumber k_p and elevation variance $\langle \eta^2 \rangle$, are in good agreement with the well established growth rates from previous observations under stable atmospheric stratification. Measurements of wavenumber spectra have an advantage over frequency spectra because, at leading order, they are not subject to Doppler shifting due to long-wave short-wave interactions. The characterization of the directional spectrum highlights the approximate self-similar nature of the wave field. The tail of the observed one-dimensional k_1 spectra

$\phi_1(k_1)$, where the unit vector $\hat{k}_1$ corresponds to the direction at the spectral peak, exhibits a single power-law of k_1^{-3} over a wide range of wavenumbers, between $2 < k/k_p < 40$, filling the existing gap, at wavelengths between 17.5 and 1.5 m, for the available measurements of wavenumber spectra in the literature. We present the first quantification of the transition between the equilibrium and saturation ranges for the omnidirectional spectrum in the wavenumber domain. Within the equilibrium range, the omnidirectional spectrum $\phi(k)$ is approximately proportional to $k^{-5/2}$, and is followed by the saturation range, at higher wavenumbers, where $\phi(k) \sim k^{-3}$. This transition occurs at a wavenumber k_o, in the range of $9k_p$ to $23k_p$, varying with the effective wave age c_p/u_{*_e}. While the energy density within the equilibrium range shows a dependence on c_p/u_{*_e}, the saturation range is approximately independent of the wind forcing. Within the saturation range, the measurements suggest that the two-dimensional wavenumber spectrum $F(\mathbf{k})$ is approximately proportional to k^{-4}. Nevertheless, at these scales, the one-dimensional saturation in the direction orthogonal to the wind is on average 30% larger than that in the downwind direction, suggesting that the directional distribution is slightly bimodal. At lower wavenumbers, the directional spreading and the width of the spectrum in the direction orthogonal to the wind are both weakly dependent on the wave age. The resolved bimodal directional distribution at wavenumbers higher than the spectral peak, characterized through the amplitude and separation of the lobes, is also weakly dependent on the wave age. Unlike previous studies, these measurements provide a consistent scaling for the average separation and amplitude of the lobes, both parameters collapse when scaled by $(c_p/u_{*_e})^{1/2}$. The one-dimensional fetch-limited k_1 spectrum is well parameterized by a double power-law and the JONSWAP peak enhancement function with dependence on the effective fetch and friction velocity. The measurements show that the peakedness factor enhances the spectral peak for young seas, decreasing with increasing wave age, and becoming smaller than unity near full development, which

results in a peak reduction. Our results are discussed in the context of previous observations and current numerical wind-wave prediction models.

I.2 Introduction

Wind-waves are important for air-sea interaction as they influence the exchange of mass, momentum, and energy between the ocean and the atmosphere (Donelan, 1990; Melville, 1996). As a wave field develops, the wind provides wave energy and momentum to the ocean, some of which can propagate away from the generation area in the form of swell, while the remainder is lost locally (primarily due to wave breaking) to generate currents and turbulence. Donelan (1998) used field measurements of the wave growth (Donelan et al., 1992) and the parameterization of wind input from field and laboratory measurements by Donelan (1987) to show that less than 5% of the total energy and momentum supplied by the wind is retained by the surface waves; however, recent models suggest that at short fetches it may be 20% or more (Romero and Melville, 2008b). Surface waves extract momentum from the atmosphere and influence the drag coefficient by supporting wave-induced stresses (Janssen, 1989). Banner and Melville (1976) and Banner (1990b) showed experimentally that air-flow separation over steep breaking waves can enhance the momentum transfer when compared to attached flows. Swell traveling faster than the wind may result in a momentum flux from waves to wind (Grachev and Fairall, 2001).

In the mid 1900's the study of surface waves gained a lot of interest after the pioneering work by Sverdrup and Munk (1947). In the past 60 years, the use of various observational, theoretical, and experimental investigations have resulted in a better understanding of many processes involved in the generation and evolution of surface waves (Mitsuyasu, 2002). For example, it is now possible to predict wind-sea wave heights, periods, and direction fairly well for practical applications at global scales (Komen et al., 1994; TheWiseGroup, 2007). However, numerous

physical processes and properties of wind-waves remain poorly understood, including wave generation by wind, directional properties of the spectrum at finite fetch, evolution of the spectrum under high winds (>15 m s^{-1}) , and deep-water wave breaking (TheWiseGroup, 2007).

In this study we present the analysis of state-of-the-art wind-wave measurements collected from the NSF/NCAR C-130 aircraft during the Gulf of Tehuantepec Experiment (GOTEX) in February, 2004. The Gulf of Tehuantepec is characterized by strong offshore winds that occur primarily during the boreal winter (Romero-Centeno et al., 2003) when cold weather systems move south into the Gulf of Mexico creating significant pressure differences across a mountain gap (in the Tehuantepec Isthmus) forcing an offshore wind-jet (known as 'Tehuano') over the Pacific Ocean.

Mesoscale numerical simulations of the Gulf of Tehuantepec by Steenburgh et al. (1998) showed a wind-jet that reached a maximum speed of 25 m s^{-1} and turned anticyclonically as it emerged out of Chivela Pass. Figure I.1 shows the typical structure of the fully developed wind-jet from QuikScat scatterometer winds, around 12:05 UTC on February 17th, 2004. The wind-jet is narrowest and strongest nearshore with a mean orientation due south, turning anticyclonically and extending out over the Pacific for 500 kilometers or more. Work by Schultz et al. (1998), estimated that in a typical year there are 10-12 wind events, each lasting from 2 to 6 days. Thus, the high probability and predictability of offshore wind events in the Gulf of Tehuantepec make this an ideal location to study air-sea interaction processes.

In this study we present our analysis of the evolution of the directional wavenumber spectrum of fetch-limited waves during Tehuano conditions. Preliminary results focused on the incidence of extreme waves have been reported elsewhere (Melville et al., 2005). In Section I.3 we introduce the variables and notation, and provide a brief summary of other relevant wind-wave studies. In

Section I.4 we describe the experiment, measurements, and methods used in the analysis. In Section I.5 we present the results, which are compared with available wind-wave observations. In Section I.6 we present a parameterization of the observed one-dimensional wavenumber spectra. In Section I.7 we discuss our results.

I.3 Background

I.3.A Definitions

The ocean surface elevation can be approximated to first order as a linear superposition of sinusoidal wave trains. Following Phillips (1977), for a stationary and homogeneous wave field, the ocean surface can be described in terms of the three-dimensional spectrum $\chi(\mathbf{k},\omega)$, defined as the Fourier transform of the covariance of the surface displacement $Z(\mathbf{r},t) = \overline{\eta(\mathbf{x},t)\eta(\mathbf{x}+\mathbf{r},t+\tau)}$:

$$\chi(\mathbf{k},\omega) = (2\pi)^{-3} \int\int Z(\mathbf{r},t) e^{-i(\mathbf{k}\cdot\mathbf{r}-\omega\tau)} d\mathbf{r} d\tau, \tag{I.1}$$

where η is the displacement from the mean sea level, $\mathbf{k}$ is the wavenumber vector and ω is the radial frequency. By definition, the integral of $\chi(\mathbf{k},\omega)$ over all wavenumbers and frequencies equals the variance ($\langle\eta^2\rangle = \int\int \chi(\mathbf{k},\omega) d\mathbf{k} d\omega$), which is proportional to the sum of the potential and kinetic energy densities, $E = \rho_w g \langle\eta^2\rangle$, where g is the gravitational acceleration and ρ_w is the water density.

In practice, most field observations of wind-wave spectra are limited to only measuring projections of $\chi(\mathbf{k},\omega)$. Following Banner (1990a) these include:

the frequency spectrum:

$$\psi(\omega) = \int_{-\infty}^{\infty} \chi(\mathbf{k},\omega) d\mathbf{k} \tag{I.2}$$

the directional frequency spectrum:

$$\varphi(\omega,\theta) = 2\int_{0}^{\infty} \chi(k,\theta,\omega) k dk \tag{I.3}$$

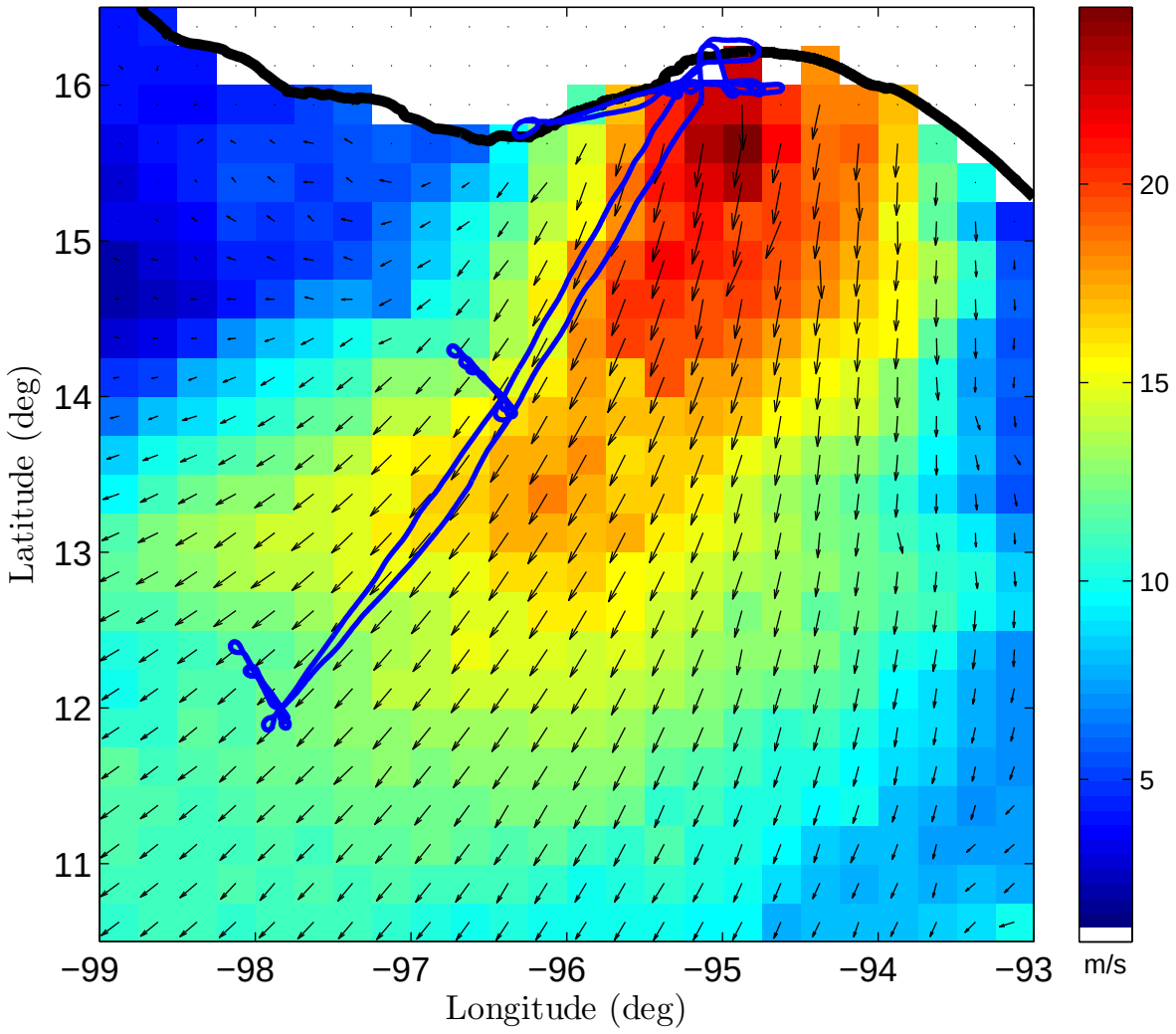

Figure I.1: QuikScat winds for Feb. 17, 2004. The figure shows the typical structure of the wind jet during Tehuano conditions over the Gulf of Tehuantepec. The solid blue line corresponds to the flight track for research flight 05.

the directional wavenumber spectrum:

$$F(k,\theta) = 2\int_0^\infty \chi(k,\theta,\omega)d\omega \tag{I.4}$$

the omnidirectional wavenumber spectrum:

$$\phi(k) = \int_{-\pi}^{\pi} F(k,\theta)kd\theta \tag{I.5}$$

k_1 and k_2 spectra:

$$\phi_1(k_1) = \int_{-\infty}^{+\infty} F(k_1,k_2)dk_2 \tag{I.6}$$

$$\phi_2(k_2) = \int_{-\infty}^{+\infty} F(k_1,k_2)dk_1, \tag{I.7}$$

where $k = (k_1^2 + k_2^2)^{1/2}$, and $\theta = \arctan(k_2/k_1)$.

For waves obeying the linear deep-water dispersion relationship, $\omega^2 = gk$, measured frequency spectra can be converted to the wavenumber domain according to:

$$F(k,\theta) = \frac{1}{k}\frac{\partial\omega}{\partial k}\varphi(\omega,\theta) \tag{I.8}$$

$$= \frac{g^{1/2}}{2k^{3/2}}\varphi(\omega,\theta). \tag{I.9}$$

However, temporal point measurements (e.g. pitch and roll buoys) are greatly affected by the Doppler shift caused by surface currents and the orbital motions of longer waves on the shorter waves (Kitaigordskii et al., 1975; Phillips, 1981). The computations by Banner (1990a) showed that the Doppler shift induced by steep dominant waves can significantly reduce the spectral slope at high frequencies. The problems arising from single point measurements can be significantly reduced by using spatial measurements such as airborne observations of the ocean surface topography, which essentially capture a snap-shot of the surface wave field not affected at leading order by the Doppler shift induced by currents and the motion of the dominant waves.

I.3.B Previous Wind-Wave Studies

Because the development of wind generated wave fields can be influenced by water depth, coastal topography, surface currents, and the spatial structure and steadiness of the wind field, the ideal conditions to study the development of a wave field are either fetch or duration-limited (Young, 1999). Fetch-limited conditions are defined as steady and homogeneous winds blowing off an infinite and straight coastline, and duration-limited conditions correspond to steady and homogeneous winds blowing over an infinite area from some initial time. Using similarity arguments, Kitaigorodskii (1962) proposed that under ideal conditions the main controlling parameters of the wind-wave spectrum are the gravitational acceleration g, the friction velocity u_*, and the fetch X, or duration, depending on the conditions. However, in practice most field observations of wind waves typically measure the horizontal surface winds and not u_*, thus relying on either bulk parameterizations of the drag coefficient (e.g. Wu, 1982), or on the surface wind speed (typically at 10m above the mean sea surface, U_{10}) as the scaling velocity for the analysis of the wind-wave spectrum.

The measurements of fetch-limited waves by Hasselmann et al. (1973), collected during the Joint North Sea Wave Project (JONSWAP), are considered a milestone in the study of wind-generated ocean waves with some of the most important outcomes being the parameterization of the frequency spectrum and the empirical fetch relationships [following Sverdrup and Munk (1947) and Bretschneider (1952), the so called SMB curves], which relate the dimensionless energy density $\tilde{\varepsilon} = \frac{g^2\langle\eta^2\rangle}{{U_{10}}^4}$ and peak frequency $\tilde{\nu} = \frac{U_{10}f_p}{g}$ to the dimensionless fetch $\tilde{\chi} = \frac{gX}{U_{10}^2}$, where f_p is defined in Hz.

Since the work by Hasselmann et al. (1973) several field investigations have been carried out to study the evolution of fetch-limited wind-wave spectra, primarily in the frequency domain, in wind speeds ranging from 5 to 15 m s^{-1}, e.g. Kahma (1981), Donelan et al. (1985), Dobson et al. (1989), Donelan

et al. (1992). However, the various growth rates reported had considerable scatter. Kahma and Calkoen (1992) reanalyzed various open ocean and lake observations of fetch-limited waves, including the JONSWAP data and Lake Ontario measurements by Donelan et al. (1985), and found a significant reduction in the scatter by sorting the data into stable and unstable conditions, according to the atmospheric stratification. Unlike Janssen et al. (1987), Kahma and Calkoen (1992) found little change when scaling the fetch relations with u_*, which they estimated using a bulk parameterization of the drag coefficient.

More recently Hwang et al. (2000a,b) reported on the analysis of airborne observations of directional wavenumber wind-wave spectra with good directional resolution for a quasi-steady and a decaying wave field under mild forcing conditions, having wind speeds of 10 m s^{-1}. In this study, we present similar airborne observations of directional wavenumber spectra over a wide range of fetches in strong winds, between 10 and 20 m s^{-1}, as well as estimates of u_* from wind measurements collected at an altitude between 30 to 50 m above the mean sea level.

I.4 The Experiment

Data were collected from the NSF/NCAR C-130 aircraft, which allows large spatial coverage over hundreds of kilometers in a relatively short amount of time. The aircraft was equipped with fast response (25 Hz) instrumentation to measure the standard atmospheric variables, including the temperature, humidity, and vector winds, including the turbulent fluxes (Brown et al., 1983). The sea surface elevation was measured with two laser-based instruments, the NASA/EG&G Airborne Topographic Mapper (ATM), which is a conically-scanning LIDAR, and a fixed nadir-looking RIEGL laser measurement system (model: LD90-3800EHS-FLP). In this study we present the analysis of wavenumber spectra from measurements collected on the 17th, 19th, 26th and 27th of February 2004, which

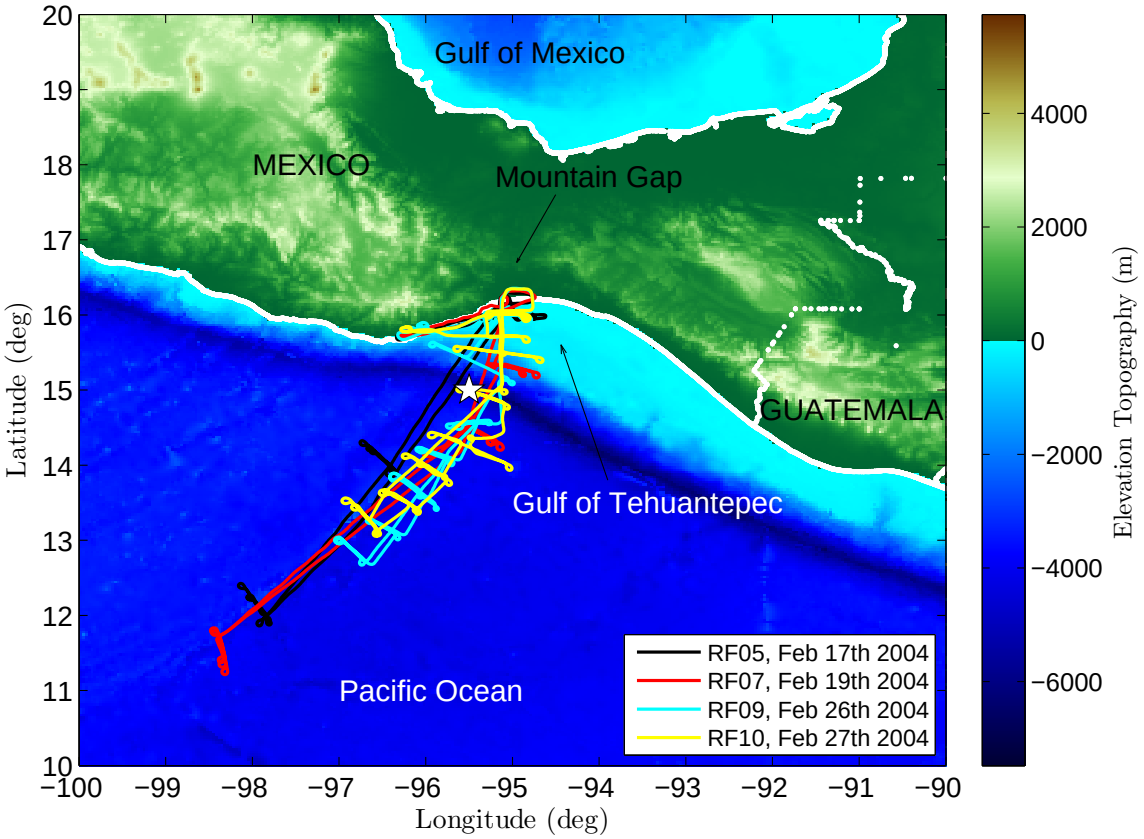

Figure I.2: GOTEX flight tracks from research flights 05, 07, 09, and 10. The white star corresponds to the location of wind time series shown in Figure I.3.

correspond to research flights (RFs) 05, 07, 09, and 10, with the flight tracks shown in Figure I.2. Figure I.3 shows the time history of the surface winds over the last two weeks of February 2004 at (15°N ,95.5°W) in the Gulf of Tehuantepec. The wind speed and direction were obtained from the National Centers for Environmental Prediction (NCEP) North American Regional Reanalysis (NARR), and the QuikSCAT scatterometer. The flight periods for RF 05, 07, 09 and 10 are shown with solid gray lines. The time series shows two main wind events, with the strongest between the 15th and 20th and the other between the 26th and 29th of February. In contrast to RF 07 and 09, which were conducted during the final and initial stages of a wind event, respectively, RF 05 and 10 were carried out during

quasi-steady wind conditions. In order to minimize the uncertainties associated with the unsteadiness of the wind field, for RF07 we only considered the morning measurements which are limited to the downwind leg between the coast and the furthest point offshore, and for RF09 we considered both morning and afternoon measurements but only within 200km off the coast.

I.4.A Sea Surface Topography

The ATM is a conical scanning LIDAR developed by NASA/EG&G, which is principally used to monitor ice sheets and glaciers in polar regions (Krabill et al., 1995). The ATM was previously deployed by Hwang et al. (2000a,b) to measure the directional properties of surface waves at Duck, North Carolina. During GOTEX, the ATM's conical scanning angle was 15^o with a pulse repetition and sampling frequency $f_s = 5$ kHz and a scanning frequency f_{sc}= 20 Hz. The ATM operated primarily at a nominal altitude of 400 m above the mean sea surface. For this configuration the radius of the scanning pattern on the sea surface, R, is approximately 100 m. Assuming no pulse return dropouts, the maximum horizontal separation between consecutive measurements in the along-flight direction is given by the ratio of the horizontal aircraft speed v_a to the scanning frequency f_{sc}. For the typical value of $v_a \approx 100$ m s^{-1}, the horizontal resolution in the along-flight direction is 5 m. The cross-track resolution is approximately 2.5 m, given by the ratio of the perimeter of the circular scan at the surface ($P = 2\pi R \approx 628$) and the number of pulses along the scan, $N = f_s/f_{sc}$= 250. The angle of dispersion of the laser is 1 mrad which corresponds to an ocean surface footprint of 0.4 m when flying at an altitude of 400 m. According to Krabill and Martin (1987), the calibrated absolute error per pulse in the elevation measured by the ATM is 8 cm, which includes a 3 cm (rms) range error, 5 cm for positioning through differential GPS, and 5cm for altitude induced errors.

The fixed LIDAR altimeter (RIEGL) provided reliable backscatter when

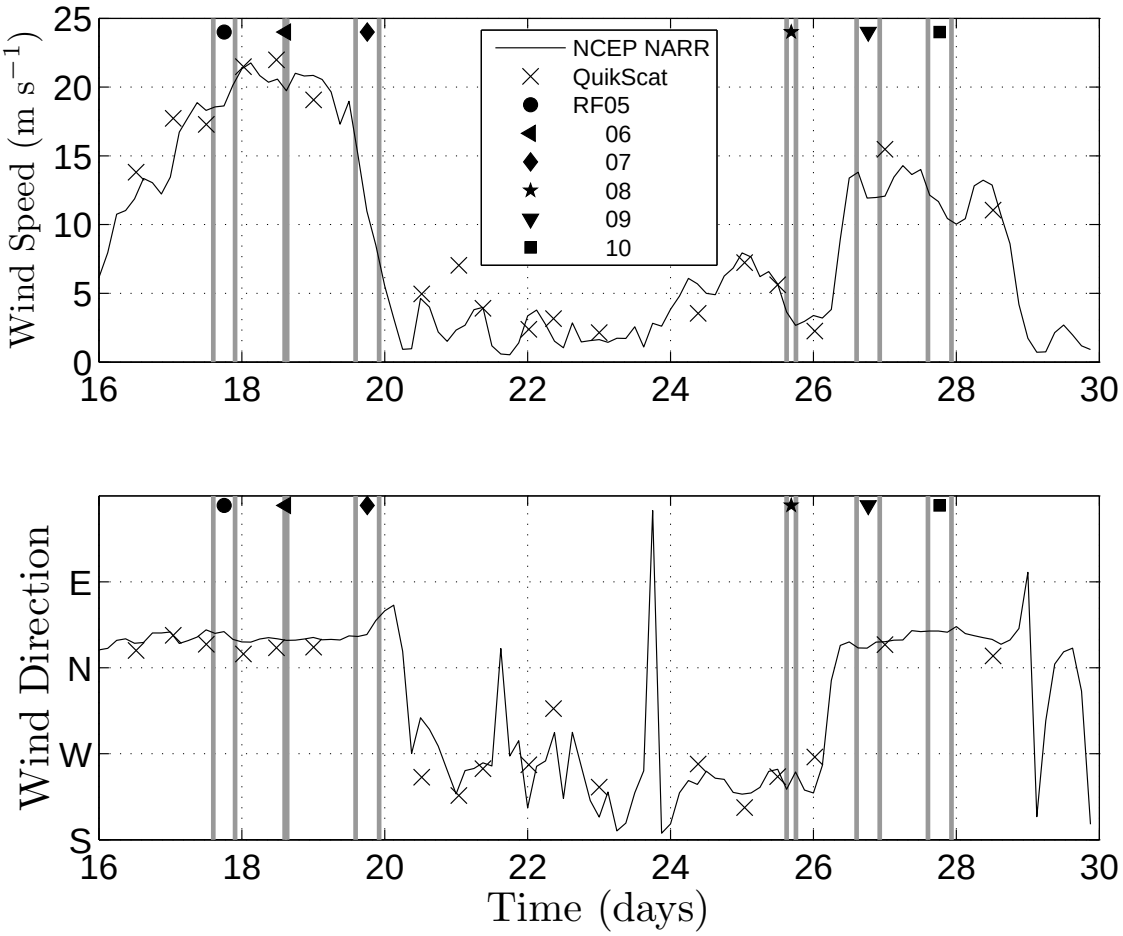

Figure I.3: Time series for February 2004 of surface wind speed and direction from scatterometer QuikSCAT and model NCEP/NARR wind products at (15^{o}N, 95.5^{o}W). The gray dashed lines correspond to the flight periods for RF05, 07, 09 and 10.

flying at altitudes between 30 and 200 m above the mean sea level. The RIEGL was set to sample the ocean surface at 5 kHz, and had a typical pulse return rate of approximately 65%. All available pulse returns within a time interval of 0.01 s were averaged to a single value. Thus, the effective data rate was 100 Hz, resulting in a horizontal resolution of approximately 1 m and a typical data dropout rate of about 5%. Data dropouts were filled in through linear interpolation. Due to a beam divergence of 1.6 mrad by 1.8 mrad , the RIEGL footprint on the sea surface was at most 32 cm by 36 cm, which is smaller than the Nyquist wavelength of 2 m.

Before estimating the one-dimensional spectra from RIEGL measurements, the aircraft motion must be removed from the raw signal. This was done following Walsh et al. (1985), in which the sea surface displacement η relative to the mean sea surface elevation is given by:

$$\eta = h - r\cos\varphi_T - \langle h - r\cos\varphi_T \rangle \tag{I.10}$$

$$\varphi_T^2 = \varphi_r^2 + \varphi_p^2, \tag{I.11}$$

where h is the aircraft altitude, r is the LIDAR range, φ_r and φ_p are the pitch and roll angles, respectively, and the brackets on the right side represent an spatial average over the record length. h is obtained from the Differential Global Positioning System (DGPS) with an accuracy of ± 10 cm. The net rms elevation error is approximately 11cm, which includes the RIEGL's range accuracy of 5cm and the DGPS uncertainty.

The spatial profiles of the sea surface elevation obtained from the RIEGL measurements were either roughly aligned with or perpendicular to the mean wind direction, giving one-dimensional k_1 and k_2 spectra with respect to the wind. The wavenumber spectrum was estimated using standard Fourier techniques from spatial series 5km long tapered with a Hann window. The Doppler shift induced in the k_1 spectra due to the relative motion between the the waves and the aircraft was corrected as described in Section (I.4.B).

I.4.B Directional Wavenumber Spectra

The ATM data along the circular scan were separated into forward and rear scans, and each data subset was binned in a horizontal spatial grid of 5m by 5m. Since the typical dropout rate was approximately 30%, yielding an effective sampling rate of 3.5kHz, available pulses within each cell were averaged together and empty cells were interpolated from neighboring points using a 2-dimensional gaussian interpolator with an isotropic decorrelation length scale of 10m. Figures (I.4a,b) show the typical ATM sampling pattern over the ocean surface separated into the forward and rear sections of the scan. There are occasional dropout regions which are approximately 10m wide and 50m long. Figures (I.4c,d) show the sampling points over the 5m by 5m regular grid within the areas marked with solid lines in Figures (I.4a,b), respectively. In the middle section of the scan about half of the grid cells contain no data, the rest of the cells contain 1 to 2 data points each. Towards the edge of the swath, almost every cell contains at least two data points, except for the regions of dropout.

Once the data were gridded and interpolated on a regular grid, the directional spectrum was directly obtained by computing the two-dimensional FFT. The typical data segments used to compute a single spectrum were 200m wide by 5000m long. Before Fourier transforming, data were detrended, tapered with a 2-dimensional Hann window dynamically adjusted to match the meandering of the ATM swaths, and padded with zeros such that the total number of nodes was 64×1024 with spectral resolutions $dk_y = 2\pi/320 = 0.0196$ rad m^{-1} and $dk_x = 2\pi/5120 = 0.0012$rad m^{-1} in the cross-track and along-track directions, respectively. The variance lost due to zero padding and data tapering was corrected accordingly in the spectral domain. Following Walsh et al. (1985), each spectrum was corrected for the Doppler shift induced due to the relative motion between the phase speed of the waves (c) and the aircraft velocity, assuming the linear dispersion relationship. The change in wavenumber component (δk_x) in the along-track

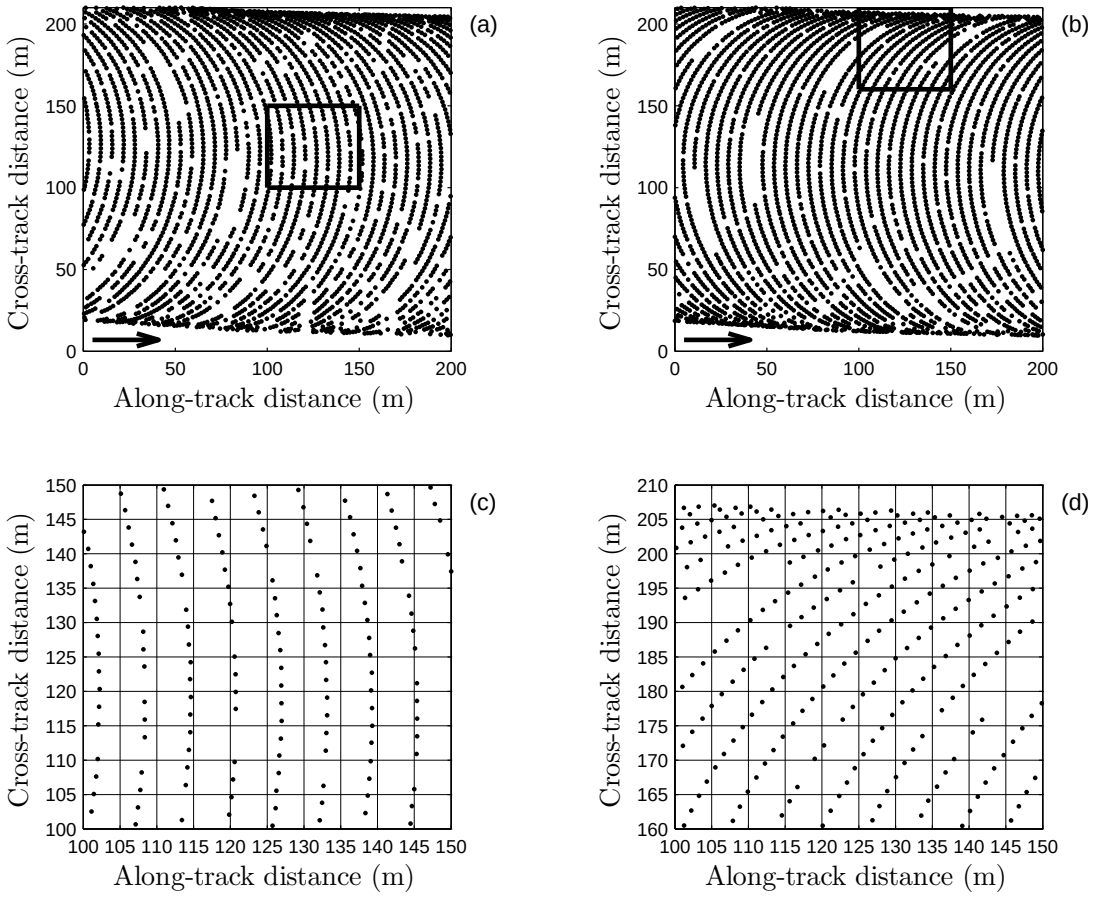

Figure I.4: Typical ATM circular scan over the ocean surface. (a,b) forward and rear sections of the scan, respectively. The black arrows point in the direction of the mean aircraft motion. (c,d) 5m by 5m binning grid over the areas shown with solid lines in panels (a,b), respectively.

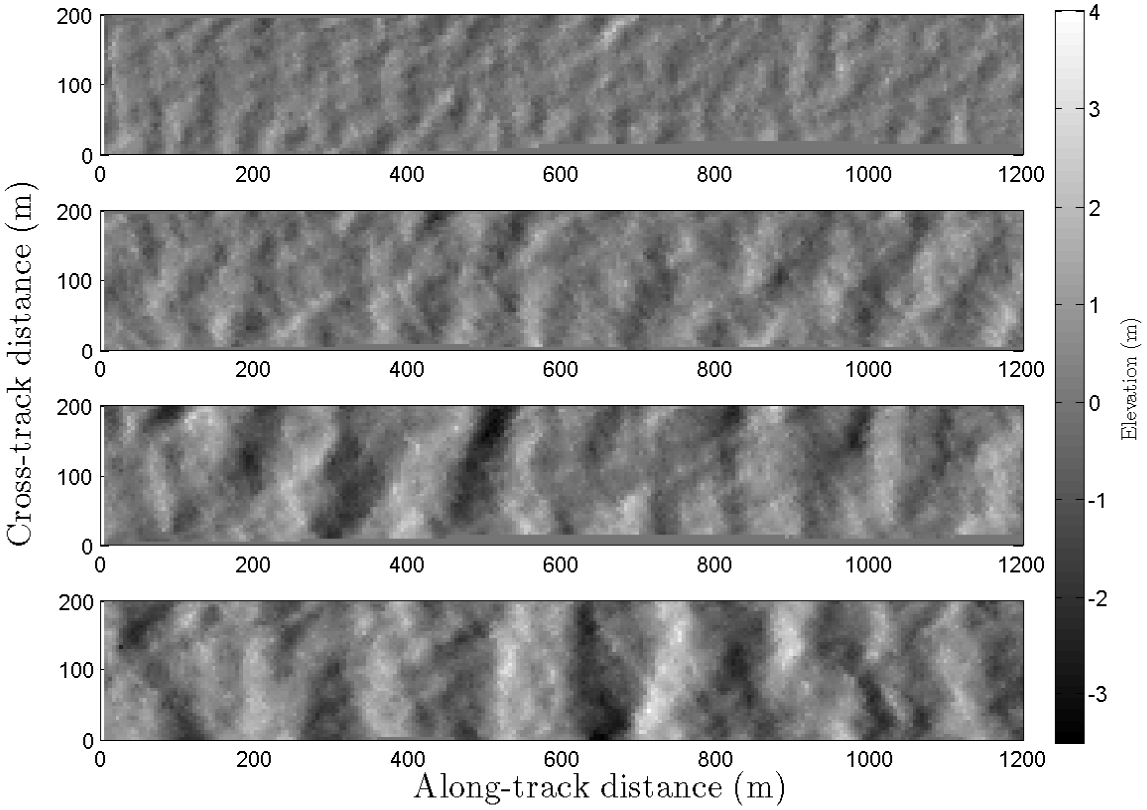

Figure I.5: Typical ATM sea surface topography measurements collected during RF05 at fetches of 24, 64, 205, and 345km , respectively, from top to bottom.

direction is given by the ratio of the wave frequency to the aircraft velocity:

$$\delta k_x = \frac{\omega}{v_a}, \tag{I.12}$$

where $\omega^2 = gk\tanh(kh)$, according to the linear dispersion relation. Thus in deep water, the relative shift $\delta k_x/k = c/v_a$ is greater for longer waves as their speeds become a non-negligible fraction of the aircraft velocity. In this study we used the ocean-floor bathymetry product by Smith and Sandwell (1997) which combines satellite and available in situ measurements. Nevertheless, the wave our measurements are effectively in deep-water, since the continental slope drops off very steeply within the Gulf.

For consistency in the analysis, a number of spectra were averaged together so that the total distance covered by each spectrum contains approximately 150 dominant waves at all fetches. In addition, each average spectrum was smoothed with a two-dimensional gaussian filter with dynamic dimensions and characteristic length so that the total number of degrees of freedom (DOFS) were the same (480) for all spectra used in the analysis. Thus the uncertainty at the 95% confidence interval corresponds to 25% of the spectral variance (Young, 1995). Finally, all spectra were rotated so that the unit unit vector $\hat{k}_1$ corresponds to the direction of the dominant waves, which was typically within a few degrees from the mean wind direction. For all the directional spectra analyzed, the difference between the dominant wave direction and the wind had a mean value of 11^o, and a standard deviation of 12^o, implying that the dominant waves are on average to the right of the wind. In this study the directional spectra analyzed correspond to measurements from either downwind or upwind flight tracks, except for one spectrum which was obtained from crosswind measurements. Figures I.6 and I.7 shows typical development of two-dimensional wave number spectra of the sea surface elevation and slope, respectively, with increasing fetch.

Before proceeding with the analysis of the data, the limitations and range of validity of the measurements must be taken into consideration. From visual

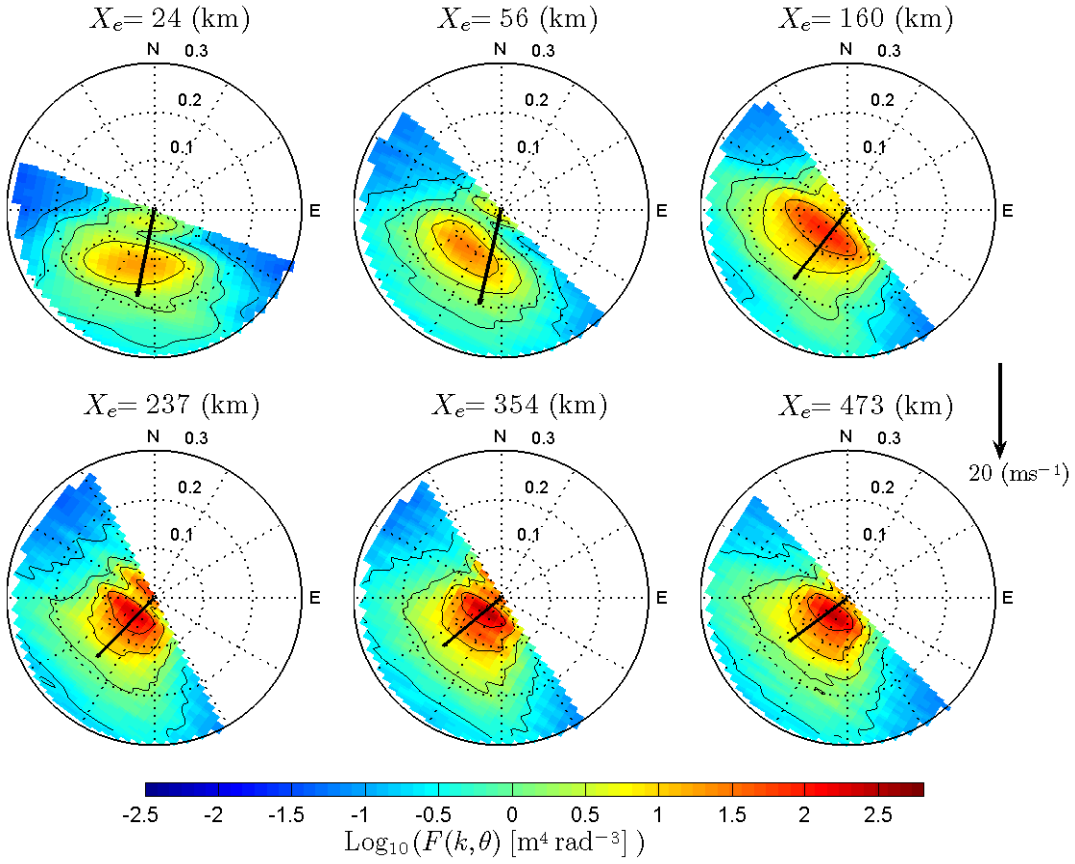

Figure I.6: Typical directional wavenumber spectra of the sea surface elevation $F(k, \theta)$ for RF05. The corresponding fetches are 24, 56, 160, 240, 354, and 473km, respectively, from left to right. The black arrows correspond to the surface wind vectors (U_{10_N}, θ_w).

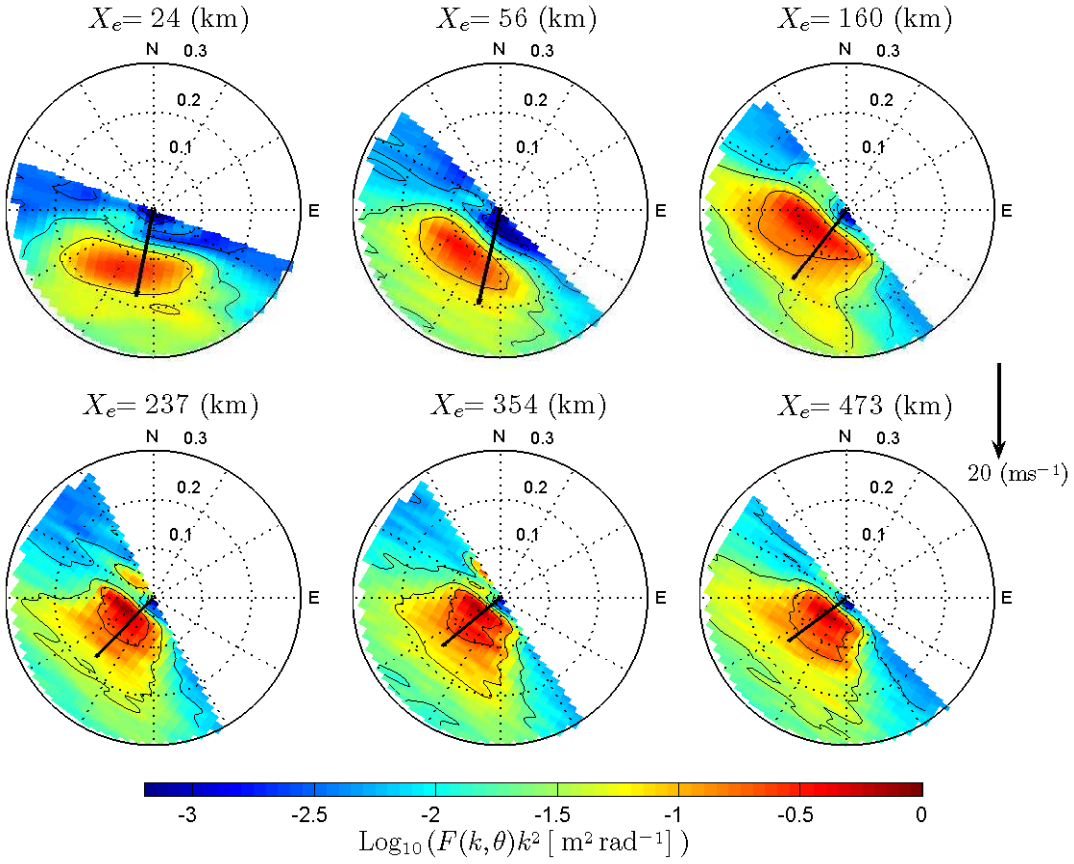

Figure I.7: Typical directional wavenumber spectra of sea surface slope $F(k,\theta)k^2$ for RF05. The corresponding fetches are 24, 56, 160, 240, 354, and 473km, respectively, from left to right. The black arrows correspond to the surface wind vectors (U_{10_N}, θ_w).

examinations of the one-dimensional k_1 and k_2 spectra, the upper limits before reaching the noise floor were determined to be 0.35 and 0.5 rad m^{-1}, corresponding to wavelengths of 18.0 and 12.6m, for the k_1 and k_2 components, respectively. These values are reasonable considering the occasional dropout segments along the scan, see Figures (I.4b,c).

The azimuthal directional resolution $d\theta$ of the measured spectra in the (k_1, k_2) plane with spectral resolutions dk_1 and dk_2, respectively, corresponds to:

$$d\theta = \frac{dk_1 dk_2}{k dk}, \tag{I.13}$$

setting $dk = dk_1$, the directional resolution becomes:

$$d\theta = \frac{dk_2}{k}. \tag{I.14}$$

From equation (I.14) the corresponding directional resolutions for the range of measured spectral peak wavenumbers (i.e., from 0.05 to 0.25 rad m^{-1}) and the upper limit of 0.35 rad m^{-1}, the corresponding directional resolutions are 22.5^o, 4.5^o, and 3.2^o, respectively. Thus for short dominant waves our measurements have good directional resolution with little information about the tail of the spectrum. Conversely, the measurements of long dominant waves have less directional resolution at the peak of the spectrum but cover a wide range of scales (up to $7k_p$) within the tail.

The circular ATM scanning pattern, see Figure I.4, results in a temporal lag between the sampling points in the cross-track direction. Although approximately 87% of the data have time-lags of 0.5s or less, the lag between the data in the central region and the edge of the swath is approximately 1 s (Hwang et al., 2000a). In order to asses the impact of the time-lag in the directional spreading of the measured spectra, we assume the linear dispersion relation to estimate the spatial lag between the central region and the edge of the swath. Considering both limits of the range of dominant waves resolved, 0.05 to 0.25 rad m^{-1}, and the upper limit of 0.35 rad m^{-1} before the noise floor, the spatial lags δx between

the center and edge of the swath over 1s are 14, 6.3, and 5.3m, respectively, which correspond to azimuthal errors $\delta\theta = \delta x/100$ of about 8^o, 3.6^o and 3^o, respectively. For the range of wavenumbers resolved $\delta\theta$ is always less than $d\theta$, thus the effect of the time-lag on the directional spreading is expected to be small.

I.4.C Surface Winds and Friction Velocity

The instantaneous wind velocities measured by the aircraft are decomposed into the mean and fluctuating components:

$$u = U + u' \tag{I.15}$$

$$v = V + v' \tag{I.16}$$

$$w = W + w', \tag{I.17}$$

where u, v, and w correspond to the two horizontal and vertical velocity components, respectively. U, V and W correspond to the temporal average of each component which translates to a spatial average due to the horizontal motion of the aircraft. The wind stress τ can be directly obtained from the horizontal Reynolds stresses:

$$\tau = \rho u_*^2 = \rho\sqrt{< u'w' >^2 + < v'w' >^2}, \tag{I.18}$$

where ρ is the air density, and the angle brackets correspond to temporal averages. In this study all estimates of u_* are from time averages of 50 s, which correspond to spatial averages over approximately 5 km. In this study we only consider the estimates of u_* collected from the lowest altitude runs, typically at approximately 30 m above the mean sea level, except for RF05 when the low altitude runs were around 50 m.

The wind profile below the aircraft can be estimated by:

$$U(z) = \frac{u_*}{\kappa}\left(\ln\frac{z}{z_o} - \Psi(z/L)\right), \tag{I.19}$$

where $\kappa \sim 0.4$ is von Karman's constant, z_o is the roughness length, $\Psi(z/L)$ is an empirical stratification function, L is the Monin-Obukhov length,

$$L = -u_*^3 \Theta_v / \kappa g \overline{w'\theta_v'}, \tag{I.20}$$

and Θ_v and θ_v' are the mean and fluctuating virtual potential temperature (Jones and Toba, 2001).

Under stable stratification $z/L < 0$,

$$\Psi(z/L) = 2\ln\left(\frac{1+\Phi_m^{-1}}{2}\right) + \ln\left(\frac{1+\Phi_m^{-2}}{2}\right) - 2\tan^{-1}(\Phi_m^{-1}) + \pi/2, \tag{I.21}$$

where $\Phi_m = (1 - c_- z/L)^{-1/4}$, $c_- \sim 17$. For unstable conditions, $z/L > 0$:

$$\Psi(z/L) = -c_+ z/L, \tag{I.22}$$

$c_+ \sim 4.5$ (Jones and Toba, 2001).

For neutral conditions $L = \infty$ and $\Psi = 0$, thus the equivalent neutral wind is defined as:

$$U_N(z) = \frac{u_*}{\kappa} \ln \frac{z}{z_o}. \tag{I.23}$$

Combining the equations above, the neutral wind speed at 10m above the mean sea level U_{10_N} can be obtained from measurements of $U(z_r)$, u_* and L at a reference level z_r:

$$U_{10_N} = U_N(10) = U(z_r) + \frac{u_*}{\kappa}\left\{\ln\frac{10}{z_r} + \Psi(z_r/L) - \Psi(10/L)\right\}. \tag{I.24}$$

The vertical wind profile in equation (I.24) is based on the assumption of spatial homogeneity and temporal stationarity, and no stress divergence, $\partial\tau/\partial z$ =0. The momentum budget on the GOTEX measurements reported by Friehe et al. (2006) showed that the flux divergence was significant nearshore (nearly balanced by the pressure gradient), but small at long fetches. However in this study, the stress divergence will be neglected because extrapolation of wind stress between 30 to 10m above the mean sea level, based on the stress divergence estimates between

30 and 800m reported by Friehe et al. (2006), would only increase the stress by about 10% which is small compared to the 35% rms percent error of the measured stress divergence.

I.5 The Evolution of the Wind-wave Spectrum

I.5.A Integral Parameters

Turning and spatially inhomogeneous winds, with speeds in the range from 10 to 20 m s^{-1}, in the presence of opposing swell make the Gulf of Tehuantepec an interesting place to study the evolution of fetch-limited waves. This section provides a brief summary of previous wind-wave studies, followed by our findings on the analysis of the evolution of the integral parameters, $\langle \eta^2 \rangle$ and the peak frequency f_p with respect to the fetch and measured friction velocity. In this study, f_p was estimated from the peak wavenumber k_p using the linear dispersion relationship for deep-water waves and $\langle \eta^2 \rangle$ was computed only over the wind-sea part of the spectrum. The energy of the opposing swell was filtered out using a threshold on the one-dimensional saturation $B_1 = \phi_1(k_1)k_1^3$ by finding the lowest wavenumber component k_s where B_1 is just below the threshold value $B_{1_{sea}} = 3 \times 10^{-4}$. Figure I.11 shows sample spectra and their respective values of k_s.

To our knowledge, no field study to date has found a significant effect on the overall evolution of the fetch-limited waves in the presence of swell. Kahma and Calkoen (1992) found essentially no change in the wave growth observed for data sets with or without the presence of swell. Field studies by Dobson et al. (1989) and, more recently, by Ardhuin et al. (2007) did not find a significant effect of the opposing swell on the evolution of waves with fetch. By contrast, laboratory experiments by Donelan (1987) reported reduced growth rates when paddle generated waves were imposed in the direction of the wind. Ardhuin et al. (2007) suggest that the larger steepness of the paddle generated waves in the

laboratory experiments when compared to the smaller steepness of ocean swell, could account for the reduced growth rates observed by Donelan (1987).

Table I.1: Wind and wave conditions for RF 05. The time is given in UTC, X_e is the effective fetch, U_{10_N} is the neutral wind speed at 10-m elevation, u_* is the friction velocity, θ_w is the wind direction, θ_p is the dominant wave direction, u_{*_e} is the effective u_*, and $\overline{u}_{*e}$ is the fetch-averaged u_{*_e}. k_p is the spectral peak wavenumber.

Dataset	**Time** (h:m:s)	**Lat** (deg)	**Lon** (deg)	X_e (km)	U_{10_N} (m s^{-1})	u_* (m s^{-1})	θ_w (deg)	θ_p (deg)	u_{*_e} (m s^{-1})	$\overline{u}_{*e}$ (m s^{-1})	k_p (rad m^{-1})	$\langle\eta^2\rangle$ (m^2)
						RF05						
1	15:13:43	16.12	-95.14	7	18.14	0.747	8	7	0.746	0.746	0.265	0.056
2	15:14:02	16.07	-95.14	12	18.13	0.747	9	12	0.746	0.746	0.191	0.119
3	15:14:57	16.03	-95.13	17	18.11	0.748	10	17	0.742	0.745	0.142	0.201
4	15:15:53	15.96	-95.13	24	18.09	0.748	11	21	0.736	0.743	0.133	0.235
5	15:17:01	15.87	-95.14	33	18.06	0.749	13	27	0.726	0.738	0.118	0.337
6	15:18:07	15.82	-95.18	40	18.04	0.75	14	40	0.674	0.727	0.098	0.352
7	15:19:27	15.74	-95.23	51	18.01	0.751	16	41	0.68	0.717	0.088	0.369
8	15:21:12	15.63	-95.3	63	17.97	0.753	18	61	0.556	0.686	0.079	0.425
9	15:39:03	14.48	-95.98	198	17.3	0.647	41	53	0.633	0.649	0.054	0.778
10	15:41:53	14.33	-96.08	217	17.18	0.659	42	53	0.646	0.649	0.059	0.784
11	15:58:25	13.34	-96.69	336	15.44	0.723	49	53	0.721	0.675	0.069	0.967
12	16:00:05	13.19	-96.79	354	15.16	0.681	50	56	0.677	0.675	0.044	0.881
13	16:04:01	13.02	-96.93	378	14.8	0.625	52	47	0.623	0.671	0.049	0.923
14	16:07:08	12.85	-97.08	402	14.45	0.571	54	56	0.571	0.665	0.054	0.979
15	17:34:27	12.41	-97.55	473	14.8	0.515	54	48	0.513	0.642	0.059	0.82
16	17:54:01	13.21	-96.97	358	17.53	0.644	48	65	0.617	0.707	0.044	0.898
17	17:57:08	13.32	-96.89	346	17.34	0.633	48	54	0.63	0.71	0.064	0.79
18	19:17:21	14.23	-96.27	231	16.68	0.84	44	63	0.799	0.748	0.064	0.757
19	19:35:34	14.96	-95.85	154	17.86	0.721	38	55	0.688	0.724	0.069	0.64
20	19:38:25	15.07	-95.79	141	17.99	0.773	35	58	0.711	0.727	0.064	0.606
21	19:55:51	15.75	-95.39	65	19.75	0.892	18	52	0.741	0.744	0.088	0.406
22	19:59:02	15.88	-95.31	50	19.88	0.862	13	46	0.72	0.744	0.118	0.276
23	20:00:08	15.92	-95.28	45	19.92	0.852	11	47	0.688	0.747	0.147	0.238
24	20:01:58	15.99	-95.24	35	19.99	0.834	8	30	0.772	0.772	0.157	0.195
25	20:11:01	16.12	-95	9	20.35	0.747	353	11	0.71	0.71	0.187	0.141

Table I.2: Wind and wave conditions for RF 07 and 09; see Table I.1 for details.

Dataset	**Time** (h:m:s)	**Lat** (deg)	**Lon** (deg)	X_e (km)	U_{10_N} (m s^{-1})	u_* (m s^{-1})	θ_w (deg)	θ_p (deg)	u_{*_e} (m s^{-1})	$\overline{u}_{*e}$ (m s^{-1})	k_p (rad m^{-1})	$\langle\eta^2\rangle$ (m^2)
						RF07						
1	14:59:33	16.13	-95.13	6	15.98	0.612	3	25	0.57	0.57	0.287	0.012
2	15:00:12	16.09	-95.13	11	16.07	0.602	4	22	0.572	0.57	0.251	0.038
3	15:00:51	16.04	-95.13	15	16.1	0.552	4	19	0.533	0.559	0.191	0.056
4	15:01:03	16	-95.13	20	15.74	0.582	6	22	0.559	0.559	0.166	0.089
5	15:02:09	15.95	-95.13	25	15.57	0.586	7	20	0.569	0.561	0.147	0.107
6	15:02:47	15.91	-95.13	29	15.44	0.585	7	29	0.545	0.558	0.145	0.13
7	15:03:49	15.84	-95.14	37	15.27	0.581	9	28	0.549	0.557	0.124	0.171
8	15:05:06	15.75	-95.17	47	15.06	0.572	11	29	0.545	0.554	0.104	0.212
9	15:06:41	15.64	-95.21	59	14.84	0.561	13	27	0.544	0.552	0.092	0.265
10	15:24:12	14.5	-95.5	189	13.35	0.464	28	17	0.455	0.485	0.064	0.445
11	15:26:46	14.33	-95.54	209	13.08	0.468	30	27	0.468	0.483	0.062	0.515
12	15:46:03	13.46	-96.42	343	11.78	0.431	41	42	0.431	0.463	0.057	0.494
13	16:10:12	12.44	-97.56	509	11.41	0.41	53	56	0.409	0.445	0.051	0.41
						RF09						
1	15:27:08	15.79	-95.26	65	18.01	0.718	17	44	0.642	0.642	0.113	0.249
2	15:28:25	15.72	-95.31	75	18.1	0.691	24	47	0.635	0.641	0.103	0.215
3	15:29:43	15.64	-95.36	85	17.74	0.639	29	41	0.626	0.639	0.098	0.252
4	15:31:21	15.54	-95.42	97	15.99	0.583	30	45	0.563	0.63	0.103	0.294
5	16:06:41	15.03	-95.16	144	16.68	0.69	23	16	0.686	0.648	0.064	0.678
6	16:09:46	14.8	-95.14	168	16.02	0.668	26	12	0.649	0.648	0.059	0.655
7	16:50:27	14.37	-95.46	228	16.05	0.692	29	34	0.689	0.659	0.049	0.783
8	16:53:02	14.2	-95.53	247	15.14	0.634	32	39	0.629	0.657	0.074	0.796
9	17:32:33	13.96	-95.8	285	14.37	0.595	35	30	0.593	0.648	0.049	0.777
10	21:24:12	15.87	-95.32	55	17.55	0.688	17	47	0.592	0.592	0.113	0.215
11	21:25:27	15.78	-95.31	62	17.77	0.694	20	38	0.659	0.599	0.098	0.298

Table I.3: Wind and wave conditions for RF 10; see Table I.1 for details.

Dataset	**Time** (h:m:s)	**Lat** (deg)	**Lon** (deg)	X_e (km)	U_{10_N} (m s^{-1})	u_* (m s^{-1})	θ_w (deg)	θ_p (deg)	u_{*_e} (m s^{-1})	$\overline{u}_{*e}$ (m s^{-1})	k_p (rad m^{-1})	$\langle\eta^2\rangle$ (m^2)
						RF10						
1	15:23:45	15.9	-95.14	32	17.08	0.628	3	34	0.543	0.543	0.125	0.18
2	15:25:02	15.81	-95.13	40	17.22	0.65	5	28	0.596	0.554	0.106	0.246
3	15:26:19	15.72	-95.12	49	17.37	0.671	6	23	0.642	0.57	0.101	0.303
4	15:27:53	15.61	-95.13	62	17.54	0.698	7	9	0.698	0.596	0.089	0.392
5	16:11:44	15.39	-95.14	85	18.19	0.772	10	16	0.767	0.643	0.074	0.564
6	16:13:35	15.26	-95.13	99	18	0.756	11	18	0.75	0.658	0.067	0.725
7	16:15:48	15.1	-95.13	116	17.76	0.736	13	11	0.735	0.669	0.061	0.799
8	17:01:34	14.6	-95.11	170	16.42	0.693	18	8	0.683	0.674	0.049	0.738
9	17:54:00	14.16	-95.63	242	14.34	0.598	35	34	0.598	0.651	0.052	0.658
10	17:56:33	14	-95.71	261	14.17	0.603	36	44	0.597	0.647	0.054	0.704
11	18:43:49	13.68	-95.84	299	13.57	0.55	39	34	0.548	0.635	0.048	0.586
12	18:47:07	13.51	-96	323	13.31	0.524	41	30	0.515	0.626	0.049	0.63
13	19:29:04	13.33	-96.27	358	13.5	0.487	47	44	0.486	0.612	0.051	0.666
14	19:33:01	13.18	-96.44	383	13.03	0.463	48	46	0.463	0.602	0.048	0.724
15	21:33:56	15.91	-95.31	35	14.32	0.499	24	47	0.459	0.459	0.182	0.074
16	21:34:36	15.87	-95.3	40	14.36	0.516	23	23	0.516	0.465	0.166	0.075
17	21:35:56	15.78	-95.29	46	14.45	0.549	23	45	0.509	0.471	0.128	0.168
18	21:36:36	15.73	-95.29	50	14.5	0.566	23	43	0.533	0.475	0.129	0.158

The issues associated with inhomogeneous winds and slant-fetches (winds not orthogonal to the coastline) have been addressed in other studies. Donelan et al. (1985) obtained measurements in Lake Ontario using a wave-gauge array under fetch-limited conditions and avoided the effects of both inhomogeneous winds and slant-fetch by fitting the wave growth and frequency downshift against U_e/c_p, where c_p corresponds to the phase speed of the dominant waves and the effective wind speed U_e is the surface wind component in the dominant wave direction: $U_e = U_{10}\cos(\theta_w - \theta_p)$, where U_{10} is the surface wind speed at 10m above the mean sea level, θ_w is the wind direction, and θ_p is the direction of the dominant waves. Another way to account for spatial changes in wind speed was introduced by Dobson et al. (1989), using an average wind speed as the velocity scaling parameter for the fetch relationships:

$$\overline{U}_{10} = \frac{1}{X}\int_0^X U_{10}(X)dX. \tag{I.25}$$

Donelan et al. (1992), used an array of instruments located along a line with increasing fetch to measure the differential wave growth between stations in Lake St. Clair, and derived an empirical model allowing the determination of the growth rate from a fetch-dependent wind speed. For a wind speed increasing with fetch, the model predicts a reduced growth rate at short fetches (compared to a constant wind speed) but still reaches the limiting value for a Pierson-Moskowitz spectrum for fully developed seas.

For this study, the evolution of the spectral integral parameters is analyzed as follows. Since the wind and ATM measurements were collected at different flight altitudes not coincident in space and time, the measurements of u_* from low altitude flight tracks, typically at 30m above mean sea level, were interpolated onto the ATM sampling locations. For each pair of available directional spectra, the distance between the sampling locations dX and the average direction of the wind and dominant waves were estimated. u_* and dX are projected along the dominant

wave direction, corresponding to the local effective friction velocity

$$u_{*_e} = u_* cos(\theta_w - \theta_p) \tag{I.26}$$

and the effective displacement $dX_e = dX cos(\theta_X - \theta_p)$, where θ_X is the orientation of dX. The fetch-averaged effective friction velocity $\overline{u}_{*e}$ is estimated by:

$$\overline{u}_{*ej} = \frac{1}{X_{e_j}} \sum_{i=0}^{j} u_{*_e i} dX_{e_i}, \tag{I.27}$$

where the net effective fetch $X_{e_j} = \sum_{i=0}^{j} dX_{e_i}$, and the index i corresponds to the observation number ordered with increasing fetch (e.g. i= 0 is the observation closest the the coast). Tables I.1,I.2, and I.3 show the various wind and wave parameters of the directional spectra used in the analysis for RF 05, 07, 09, and 10. The maximum values of u_{*_e} were observed during RF05 when the maximum surface winds, at 50 m above the mean sea level, reached 25 m s^{-1}. Figures I.8-I.9 show the dimensionless energy and peak frequency against the dimensionless effective fetch. Although we are in fact measuring the spectral peak wavenumber, we plot the peak frequency for convenience, because previous measurements were collected in the frequency domain. Figures I.8a,b show $\overline{\varepsilon} = \langle \eta^2 \rangle g^2 / \overline{u}_{*_e}^4$ and $\overline{\nu} = f_p \overline{u}_{*_e} / g$, respectively, against $\overline{\chi} = X_e g / \overline{u}_{*_e}^2$, where f_p is in Hz. Similarly, Figure I.9a,b show $\varepsilon = \langle \eta^2 \rangle g^2 / u_{*_e}^4$ and $\nu = f_p u_{*e} / g$, respectively, against $\chi = X_e g / u_{*_e}^2$. The scatter of the data is reduced when u_{*_e} is used as the scaling velocity. The observed energy growth rates, regardless of the scaling velocity, are in agreement with the reanalysis by Kahma and Calkoen (1992) for stable atmospheric stratification. Similarly, most of the wind and wave measurements during GOTEX were obtained during stable conditions due to the strong upwelling and cooler surface waters induced by the offshore flow.

The power-law fits shown in Figures I.8 and I.9 are:

$$\overline{\varepsilon} = 4.1 \times 10^{-3} \overline{\chi}^{0.74} \tag{I.28}$$

$$\overline{\nu} = 0.22 \overline{\chi}^{-0.22} \tag{I.29}$$

$$\varepsilon = 1.6 \times 10^{-3} \chi^{0.81} \tag{I.30}$$

$$\nu = 0.28 \chi^{-0.23}. \tag{I.31}$$

Although the measurements cover a wide range of nondimensional fetches, most of the data are concentrated at intermediate fetches. For RF07 and RF10 ε and ν exceed the Pierson-Moskowitz limits (Komen et al., 1984), reaching the limiting values for fully developed seas reported in the reanalysis by Alves et al. (2003).

I.5.B One-dimensional Spectra

Figures I.10a,b show the typical evolution of $\phi(k)$ and $\phi_1(k_1)$, respectively, with increasing nondimensional fetch. Both sets of one-dimensional spectra show a peak followed by regions exhibiting power-law behaviors, approximately proportional to $k^{-5/2}$ or k_1^{-3}, respectively. The region immediately after the spectral peak of $\phi(k)$ is commonly referred to as the equilibrium range.

An equilibrium range $\propto k^{-5/2}$ has been consistently reported in analytical, observational, and numerical studies of wind-waves. Zakharov and Filonenko (1967) derived a solution for weakly nonlinear waves where the frequency spectrum is proportional to ω^{-4} (or $\phi(k) \propto k^{-5/2}$ according to the linear dispersion relationship for deep-water waves), assuming an isotropic spectrum for a range of frequencies which maintain a constant flux of energy having energy input and dissipation at low and high frequencies, respectively: a "Kolmogorov" model. The model of the equilibrium range by Phillips (1985), which assumes that the nonlinear energy flux, wind forcing, and dissipation due to whitecapping are proportional and of comparable magnitude, also predicts $\phi \propto k^{-5/2}$. Donelan et al. (1985), using a wave gauge array in Lake Ontario, reported an equilibrium range of the frequency

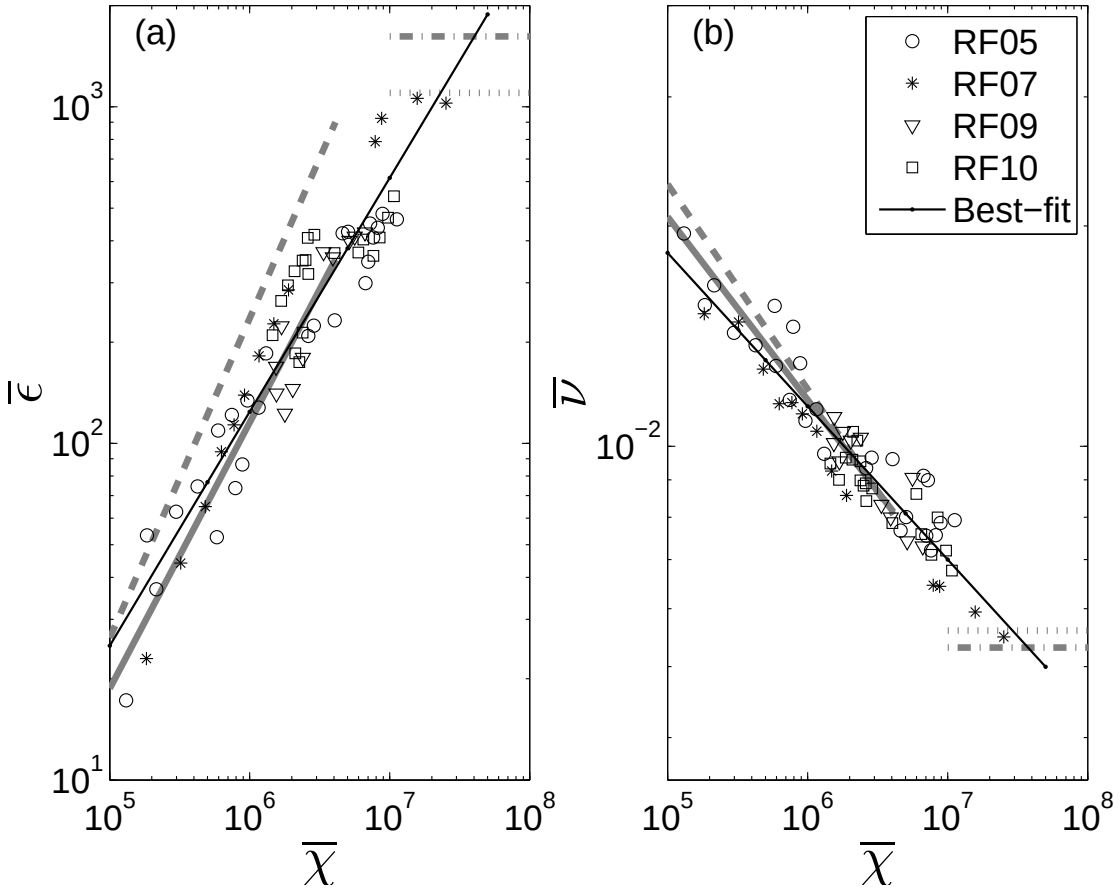

Figure I.8: Non-dimensional energy and peak frequency against non-dimensional fetch for RF 05, 07, 09 and 10. The scaling velocity is the fetch-averaged effective friction velocity $\overline{u}_{*e}$ calculated according to equation I.27. The solid gray line (gray dashed line) shows the empirical curves from Kahma and Calkoen (1992) for stable (unstable) atmospheric stratification. The limits for fully developed seas for a Pierson-Moskowitz spectrum, see Komen et al. (1984), and those by Alves et al. (2003) are shown in gray as dashed-dotted and dotted lines, respectively.

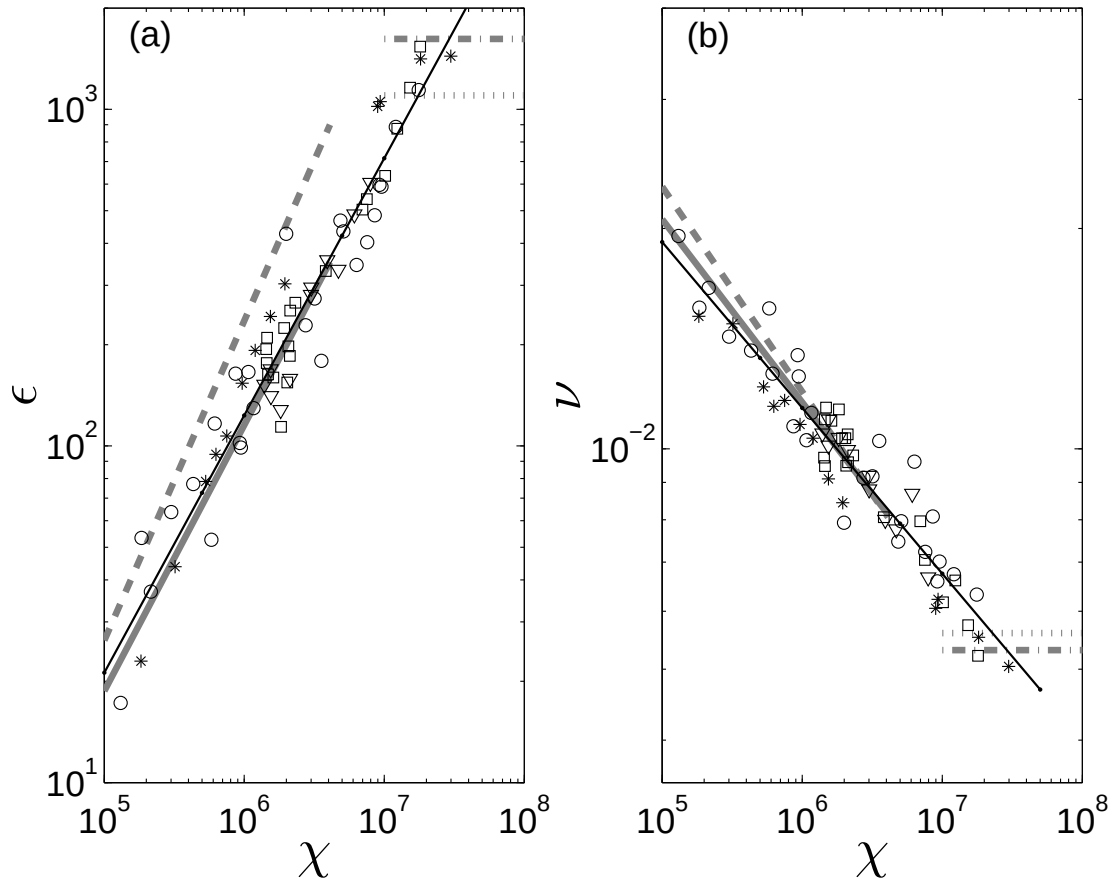

Figure I.9: Non-dimensional energy and peak frequency against non-dimensional fetch for RF 05, 07, 09 and 10. The scaling velocity corresponds to the local effective friction velocity u_{*e}, see equation I.26. The solid gray line (gray dashed line) shows the empirical curves from Kahma and Calkoen (1992) for stable (unstable) atmospheric stratification. The limits for fully developed seas for a Pierson-Moskowitz spectrum, see Komen et al. (1984), and those by Alves et al. (2003) are shown in gray as dashed-dotted and dotted lines, respectively.

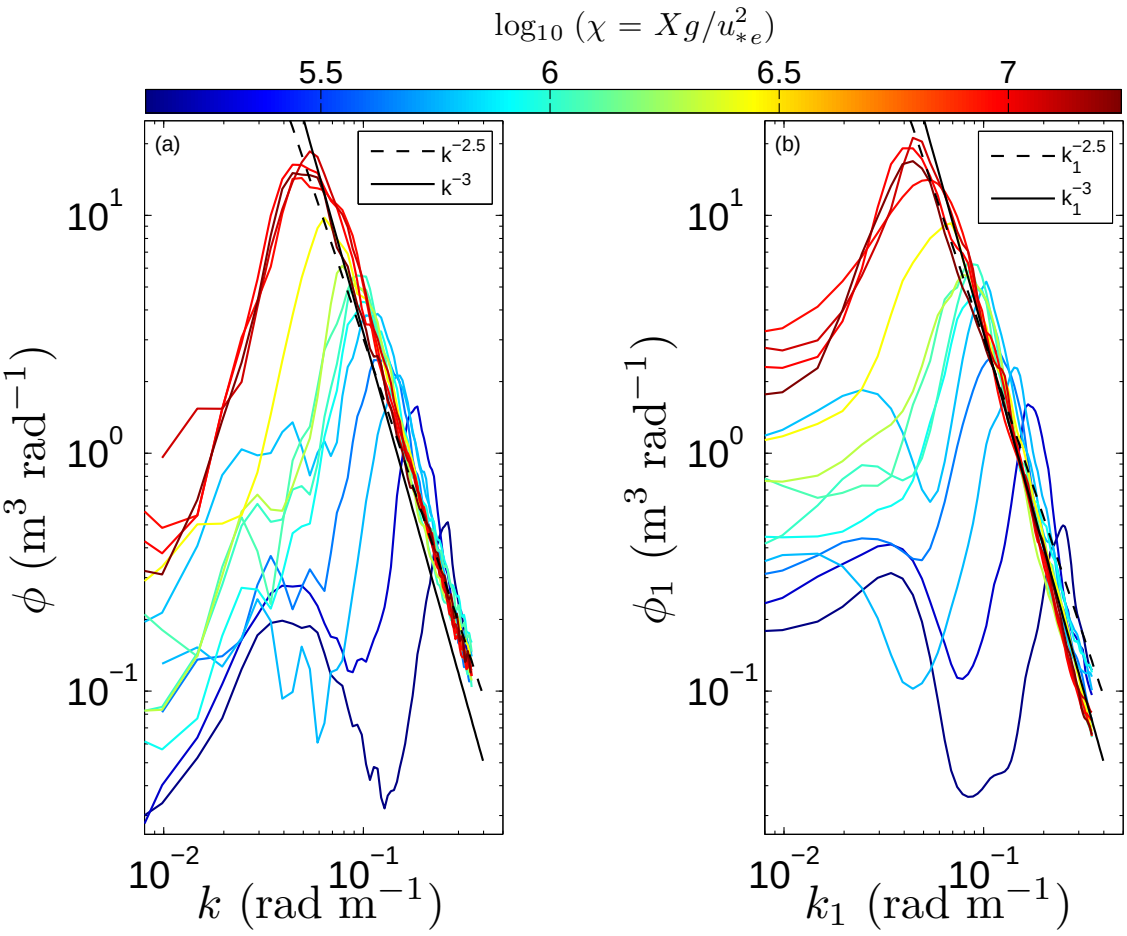

Figure I.10: Logarithmic plots of omnidirectional (a), and k_1 spectra (b), from sea surface topography measurements collected during RF05, on February 17th 2004. The dashed and solid black lines are reference spectral slopes proportional to $k^{-5/2}$ and k^{-3}, respectively. Data are color-coded according to the nondimensional fetch Xg/u_{*e}^2.

spectrum $\propto \omega^{-4}$. More recently, Hwang et al. (2000a) based on airborne observations, similar to those presented in this study, reported an equilibrium range where $\phi \propto k^{-5/2}$. Moreover, numerical investigations have also shown that in the absence of external forcing, there is a region of the spectrum which persistently evolves towards a power law $\propto k^{-5/2}$ (or ω^{-4}) regardless of the initial conditions (Onorato et al., 2002; Dysthe et al., 2003; Badulin et al., 2005).

Following Toba (1973), the equilibrium range can be defined as:

$$\phi(k) = \frac{\beta}{2} u_* g^{-1/2} k^{-5/2}, \tag{I.32}$$

where β is an empirical parameter, often referred as Toba's constant because early wave studies did not find a systematic trend with wave age, see for example the summary by Phillips (1985). However the measurements of frequency spectra by Donelan et al. (1985) and Resio et al. (2004), although not explicitly determined, imply that Toba's parameter is not a constant but a function of the wave age.

The study by Donelan et al. (1985), in lake Ontario, parameterized the equilibrium range of the frequency spectra as $\psi(\omega) = \alpha g^2 \omega_p^{-1} \omega^{-4}$, which, using the linear dispersion relationship gives:

$$\phi(k) = \frac{\alpha}{2} k_p^{-1/2} k^{-5/2}, \tag{I.33}$$

where $\alpha = 0.006(U_c/c_p)^{0.55}$, and $U_c = U_{10} cos(\theta_w - \theta_p)$. Likewise, Resio et al. (2004) proposed an alternative scaling for equation (I.32), by introducing a weak dependence on the phase speed at the spectral peak:

$$\phi(k) = \frac{\beta'}{2} (u_a^2 c_p)^{1/3} g^{-0.5} k^{-5/2}, \tag{I.34}$$

where u_a is a scaling velocity such as u_* or U_{10}. Resio et al. (2004) found a better agreement relating the equilibrium range to both the friction velocity and peak wavenumber than to the friction velocity alone.

The tail of $\phi(k)$ measured with the ATM is mostly proportional to $k^{-5/2}$, with the exception of a few cases when the spectral tail decays a little more rapidly.

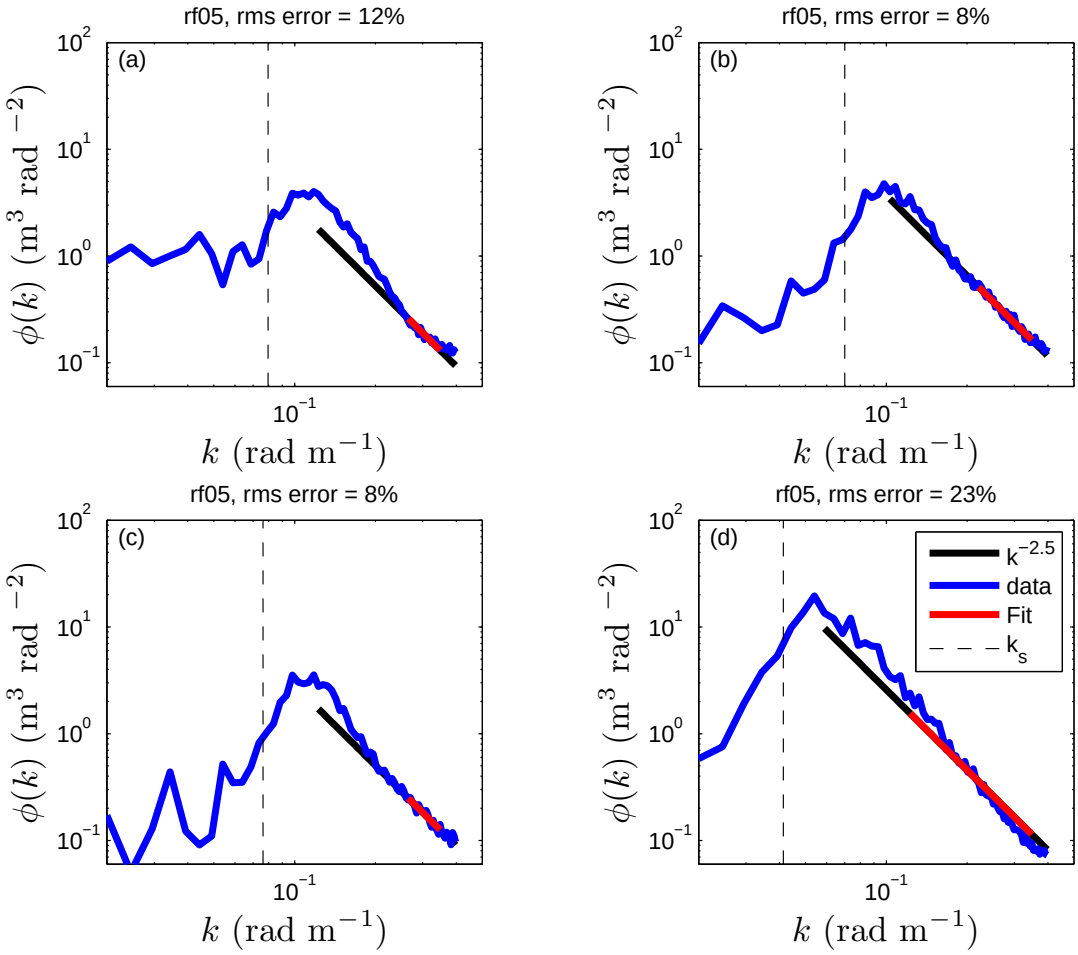

Figure I.11: Typical $k^{-5/2}$ power-law fits within the tail of the omnidirectional spectra. The red lines correspond to the fits to equation (I.32) within the range $2.25\ k_p < k < 0.35$, the black lines correspond to extrapolations of the fits towards both higher and lower wavenumbers. Panels (a-c) correspond to the typical fits with rms errors of 15% or less . Panel (d) shows a fitting case with rms error of 23%. The dashed gray line indicates the location of the wavenumber k_s separating the wind-sea part of the spectrum from the swell.

In order to determine β from equation (I.32), a dynamic range of wavenumbers is used. Following Donelan et al. (1985), the low wavenumber limit is set to $2.25k_p$, this is to avoid contamination from the spectral peak, and the upper limit was kept fixed at 0.35 rad m^{-1}, thus avoiding the noise floor. Figure I.11 shows the typical measurements of $\phi(k)$, including the fits to equation (I.32). Panels (a-c) correspond to cases where the rms error of the fit was 15% or less. Panel (d) corresponds to the case with the largest rms error of 23%. Careful examination of the data showed that cases with an rms error larger than 15% corresponded to situations where spectral slope of $\phi(k)$ was steeper than $k^{-5/2}$. However, this only occurred in 27% of all the spectra analyzed.

Figure I.12 shows Toba's parameter against the effective wave age (c_p/u_{*_e}), showing an increasing trend with increasing wave age. The range of values observed are in good agreement with those previously reported from measurements of frequency spectra as summarized by Phillips (1985) where $0.06< \beta <0.11$ (shown with dashed lines). The best power-law-fit gives:

$$\beta = 0.017(c_p/u_{*_e})^{0.54\pm0.02}, \tag{I.35}$$

where the uncertainty corresponds to the 95% confidence interval. The open squares correspond to our measurements of c_p and u_{*_e}, assuming that $u_* = u_{*_e}$, and the equilibrium range measurements by Resio et al. (2004) (See their Table 2 best-fit coefficients with $u_a = (u_*^2 c_p)^{1/3}$). GOTEX measurements agree qualitatively with Resio et al. (2004), with larger discrepancies towards lower values of c_p/u_{*_e}, and show good agreement with Hwang et al. (2000a) near full development, shown as an open star. Using our estimates of U_{10_N} and our measurements of u_{*_e}, β is obtained from the measurements by Donelan et al. (1985) and equation (I.33) (see Battjes et al., 1987), and is shown in open circles. Although, Donelan et al.'s measurements share a similar trend in β with increasing effective wave age when compared to the GOTEX measurements, the magnitude is higher on average by 70%. Finally, the dashed-dotted line with error bars corresponds to the mean and

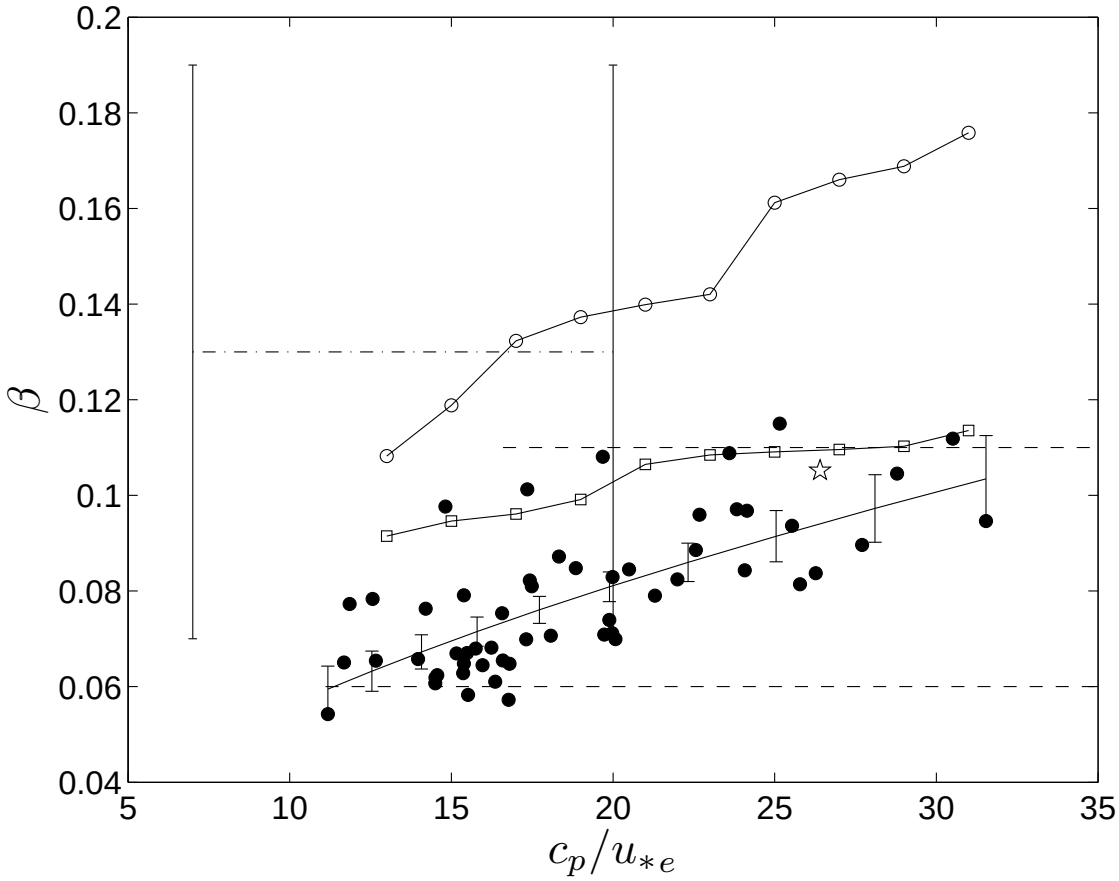

Figure I.12: Toba's parameter β versus the effective wave age c_p/u_{*_e}. The solid circles correspond to the ATM measurements. The open star is from the ATM measurements by Hwang et al. (2000a) for quasi-steady conditions. The dashed lined indicate the range of values from historical data summarized by Phillips (1985). The open squares are estimates obtained using the equilibrium range measurements by Resio et al. (2004) (see best-fit estimates in their Table 2 with scaling velocity $(u_*^2 c_p)^{1/3}$) and this study's measurements of u_* and c_p. The open circles are Donelan et al. (1985) measurements using equations I.33 and I.32. The dashed-dotted line with bars correspond to the mean and standard deviation from the reanalysis of the JONSWAP data by Battjes et al. (1987).

standard deviation of β from the reanalysis of the JONSWAP data by Battjes et al. (1987), which is comparable in magnitude to Donelan et al. (1985).

Figure I.14 shows a comparison of one-dimensional wavenumber spectra estimated from ATM and RIEGL measurements collected within 50km of each other at fetches of approximately 70, 250, and 500km. Panels (a) through (c) show k_1 and k_2 spectra from RIEGL measurements, along with neighboring ATM k_1 spectra. The ATM k_1 spectra blend well with the RIEGL spectra, showing a consistent power-law-fit of k_1^{-3} for a wide range of wavenumbers ($2 < k_1/k_p < 40$). At intermediate wavenumbers, the RIEGL k_2 spectra show a power law of approximately $k_2^{-5/2}$, followed by a transition to k_2^{-3} at higher wavenumbers. In this high wavenumber region, ϕ_2 approximately merges with ϕ_1, suggesting a loss of preferred directionality, or approach to isotropy, consistent with the observations by Banner et al. (1989) at higher wavenumbers where $F(\mathbf{k})$ is approximately k^{-4}. Figure I.14d shows the corresponding ATM omnidirectional spectra ϕ (solid black line), as well as approximations at higher wavenumbers (0.65-2 rad m^{-1}) estimated using the k_1 RIEGL spectra under the assumption of an isotropic directional distribution with $\phi \sim k^{-3}$ (red line). The combined RIEGL and ATM spectra imply a power law transition from the equilibrium range where $\phi \sim k^{-5/2}$ to the saturation range at high wavenumbers with $\phi \sim k^{-3}$, a similar power-law transition was found in broadband frequency measurements by Forristall (1981).

The k_1^{-3} power-law behavior within the tail of the k_1 spectrum, see Figure I.10, is consistent with previous observations of wavenumber spectra. Banner (1990a) compiled published measurements of the k_1 spectra, including stereophotographic measurements at high wavenumbers (Banner et al., 1989), and various airborne observations which include Barnett and Wilkerson (1967), Jackson et al. (1985a), and Schule et al. (1971). The collated data suggests that for wind conditions in the range of 7 to 15 m s^{-1}, the tail of the k_1 spectrum in the direction of the wind has a single k_1^{-3} power law over a wide bandwidth, with small variations in

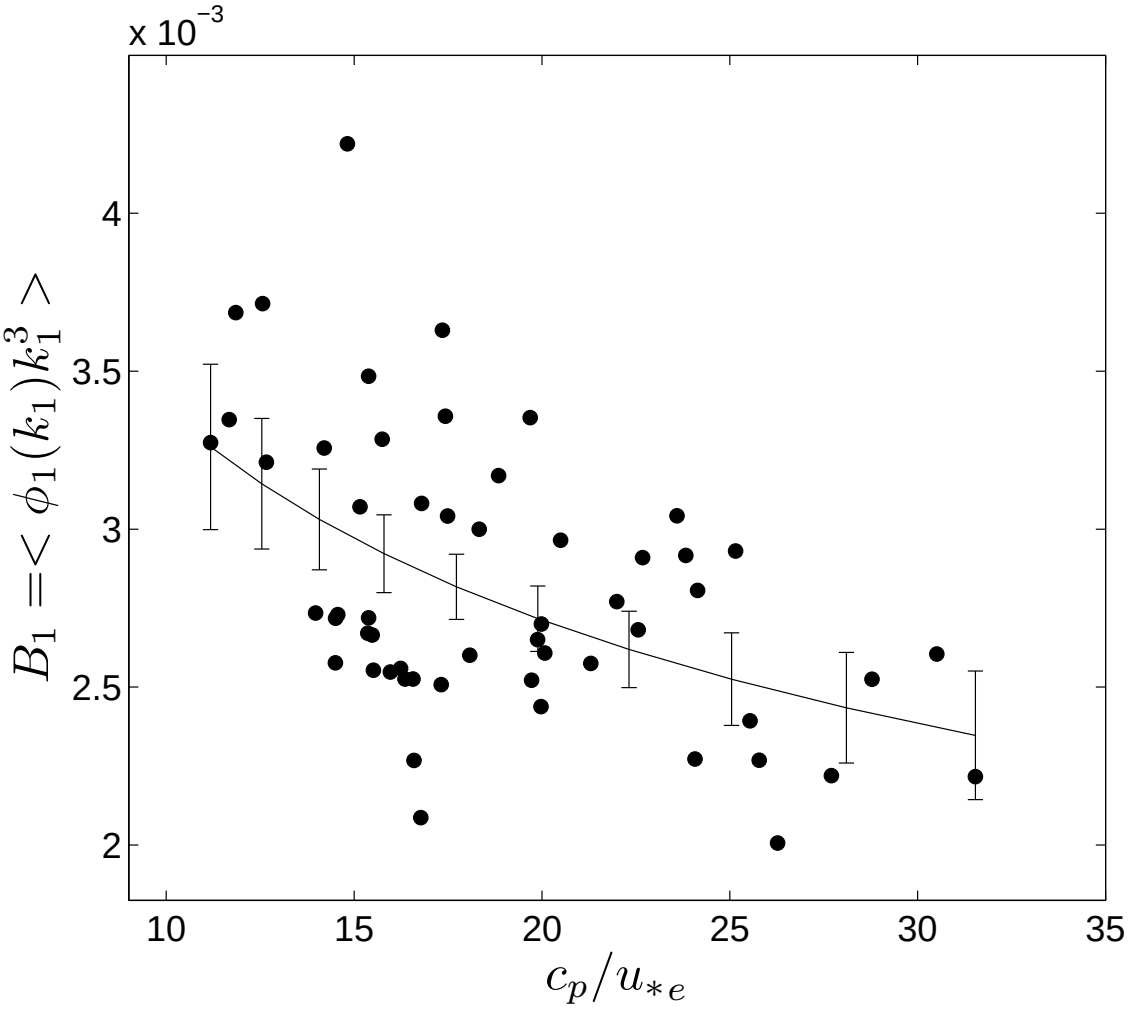

Figure I.13: Degree of saturation within the tail of the ATM k_1 spectra versus the effective wave age. The solid lines are the best-fit estimates with the 95% confidence intervals.

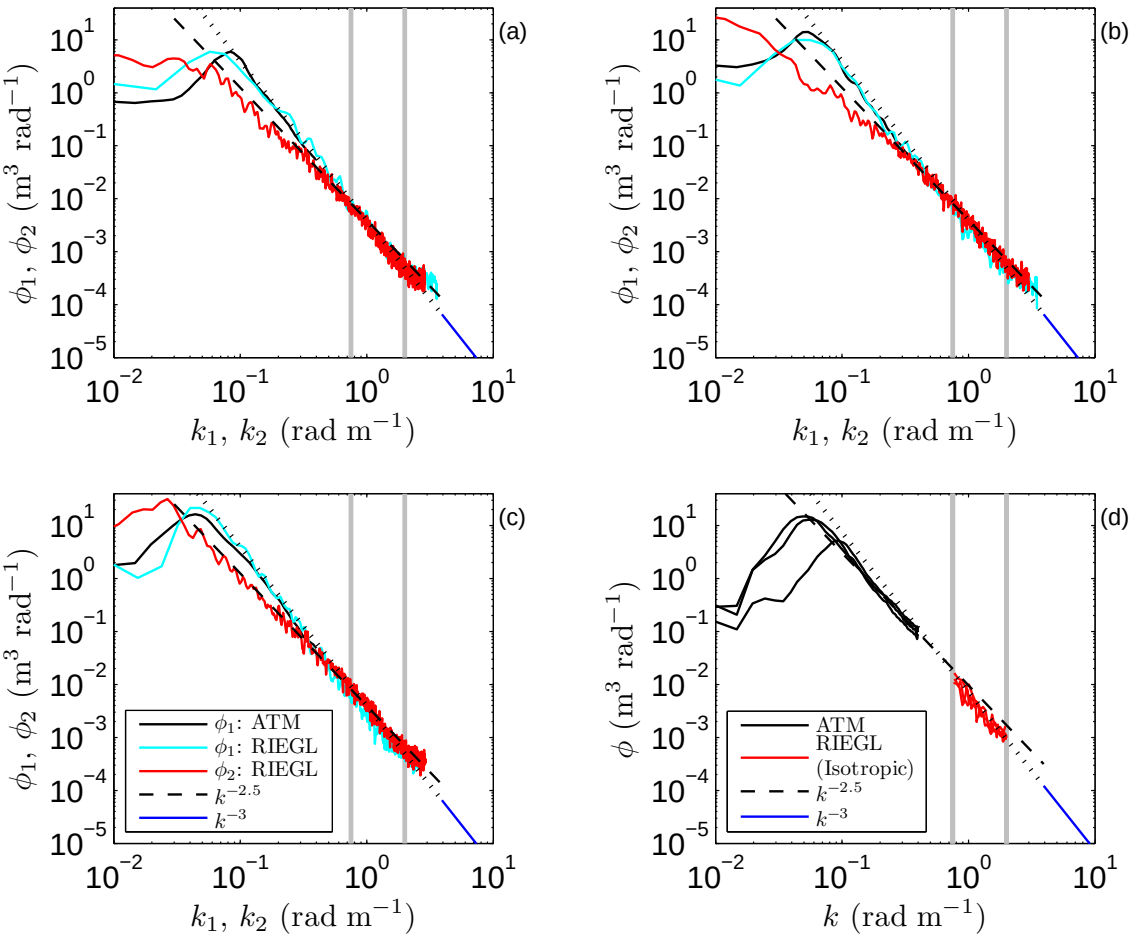

Figure I.14: Comparison of one-dimensional wavenumber spectra from measurements collected with the ATM and RIEGL during RF05. Panels (a)-(c) show one-dimensional k_1 and k_2 spectra, ϕ_1 and ϕ_2, from RIEGL and ATM measurements at fetches of approximately 70, 250, and 500km. Panel (d) shows corresponding omnidirectional spectra ϕ from the ATM measurements at the three fetches (solid black), and estimates at high wavenumbers (0.65-2 rad m^{-1}) obtained from k_1 RIEGL spectra assuming an isotropic directional spectrum $\propto k^{-4}$ (red). Reference spectral slopes $\propto k^{-5/2}$ and k^{-3} are shown as dashed and dashed-dotted lines, respectively. Measurements of Banner et al. (1989) at high wavenumbers are shown in blue and extrapolated to lower wavenumbers with dotted lines.

the proportionality constant B_1, or degree of saturation. Figure I.13 shows average estimates of B_1 over the interval $2.25k_p < k < 0.35$ rad m^{-1} from the ATM spectra plotted against the effective wave age u_{*_e}/c_p, where c_p is the linear phase speed at the spectral peak. Within this range, B_1 decreases with increasing wave age, varying between 3.7×10^{-3} for young waves and 2.5×10^{-3} near full development, in qualitative agreement with the saturation values reported by Schule et al. (1971) of 3×10^{-3}, and Barnett and Wilkerson (1967) of 4×10^{-3}.

At higher wavenumbers, the one-dimensional saturation for the k_1 and k_2 spectra B_i (i = 1,2) is calculated from RIEGL measurements within the range 0.75 $< k <$ 2 rad m^{-1}. Based on visual examinations of the spectra, it was found that within this range all of the k_2 spectra analyzed approximately followed the k_2^{-3} power-law behavior. Figure I.15a shows B_1 and B_2 against the nondimensional average wavenumber component $u_*^2\langle k_i\rangle/g$ ($i = 1, 2$), the reciprocal of the average local wave age squared. The data show that within this range of wavenumbers, the saturation is constant with no dependence on the local wave age, with $B_1 = 3.2 \pm 0.9 \times 10^{-3}$, being lower than $B_2 = 4.1 \pm 1.0 \times 10^{-3}$ by 22 %, is in excellent agreement with Melville and Matusov (2002) whose mean saturation values when computed over the same range of wavenumbers corresponds to $B_{1_{MM2}} = 3.2\times10^{-3}$. Note that the one-dimensional spectra reported in Melville and Matusov (2002) had an error of a factor of two, the saturation value given above has the correct magnitude. The dotted line shows the measurements by Banner et al. (1989) at higher wavenumbers ($1.25 < k < 10$ rad m^{-1}), which show slightly larger saturation values when compared to our measurements. The overall mean saturation for both the k_1 and k_2 spectra combined gives $B_{1,2} = 4 \pm 1 \times 10^{-3}$. The uncertainties of B_1, B_2, and $B_{1,2}$ correspond to two standard deviations.

By assuming an isotropic directional distribution within the saturation range with $F(k, \theta) \sim k^{-4}$ (Phillips, 1958) with $-\pi/2 < \theta < \pi/2$, the azimuth-

integrated spectrum becomes:

$$\phi(k) = Bk^{-3}, \tag{I.36}$$

where the azimuth-integrated saturation $B = 2B_{1,2}$ (Phillips, 1977). Following (Hwang and Wang, 2001), equations (I.36 and I.32) are solved for the wavenumber component k_o which separates the equilibrium and saturation ranges and is given by:

$$k_o = \left(\frac{2B}{\beta}\right)^2 \frac{g}{u_*^2}. \tag{I.37}$$

Figure I.15b shows k_o/k_p versus the effective wave age as estimated from equation (I.37), with k_o/k_p increasing from approximately 10 for young seas to about 23 at full development.

Forristall (1981) reported a transitional frequency component f_o, separating the analogous power-law transition in frequency spectra, which was exclusively related to u_*. The solid gray line in Figure I.15b corresponds to Forristall (1981)'s results using our measurements of k_p and u_{*_e}, assuming the linear dispersion relationship and that $u_{*_e} = u_*$. Forristal's results underpredict our estimates of k_o/k_p for young waves, and show qualitative agreement near full development. The solid black line was obtained from the best-fit of $\beta(c_p/u_{*_e})$ and equation (I.37).

The omnidirectional wavenumber spectrum can be used to estimate the mean-squared-slope (mss) of the ocean surface over a finite range of wavenumbers. According to Cox and Munk (1954), waves with a wavelength of approximately 30 cm or less contribute to more than fifty percent to the total mss. This was shown by analyzing sun-glitter photographs of the sea surface under normal and oil-slick conditions. Extrapolation of the measured omnidirectional spectra during GOTEX using Toba's scaling from equation I.32, from the 0.35 rad m^{-1} to the transition wavenumber k_o, and followed by the saturation spectrum from equation I.36, for wavenumbers as large as 21 rad m^{-1} which corresponds to a wavelength of 30 cm, yields a composite spectrum defined as $\phi_c(k)$. As shown in Figure I.16, the estimates of mss_c as given by:

$$mss_c = \int_{k_p}^{21 \text{ rad m}^{-1}} \phi_c(k) k^2 dk, \tag{I.38}$$

give values that are comparable to the extrapolation of the measurements by Cox and Munk (1954) in slick-covered conditions for a wind speed of 15 m s^{-1}, which corresponds to the average wind speed observed during GOTEX. The estimates of mss_c show a slight increase with increasing wave age during the early stages of wave development, reaching an asymptotic value around 0.035. The increase of mss with increasing wave age is associated with the increase in bandwidth of the wind-sea spectrum due to the downshift of the spectral peak.

I.5.C Other Moments of the Spectrum

Field observations and numerical investigations have shown that the directional wind-wave spectrum is narrowest near the peak and broader towards both lower and higher wavenumbers (Hasselmann et al., 1980; Hwang et al., 2000b; Banner and Young, 1994). One way to characterize the directional properties of the wave field is by computing the moments of the spectrum. Following Banner and Young (1994), the directional spreading σ_θ of a symmetric wind-wave spectrum

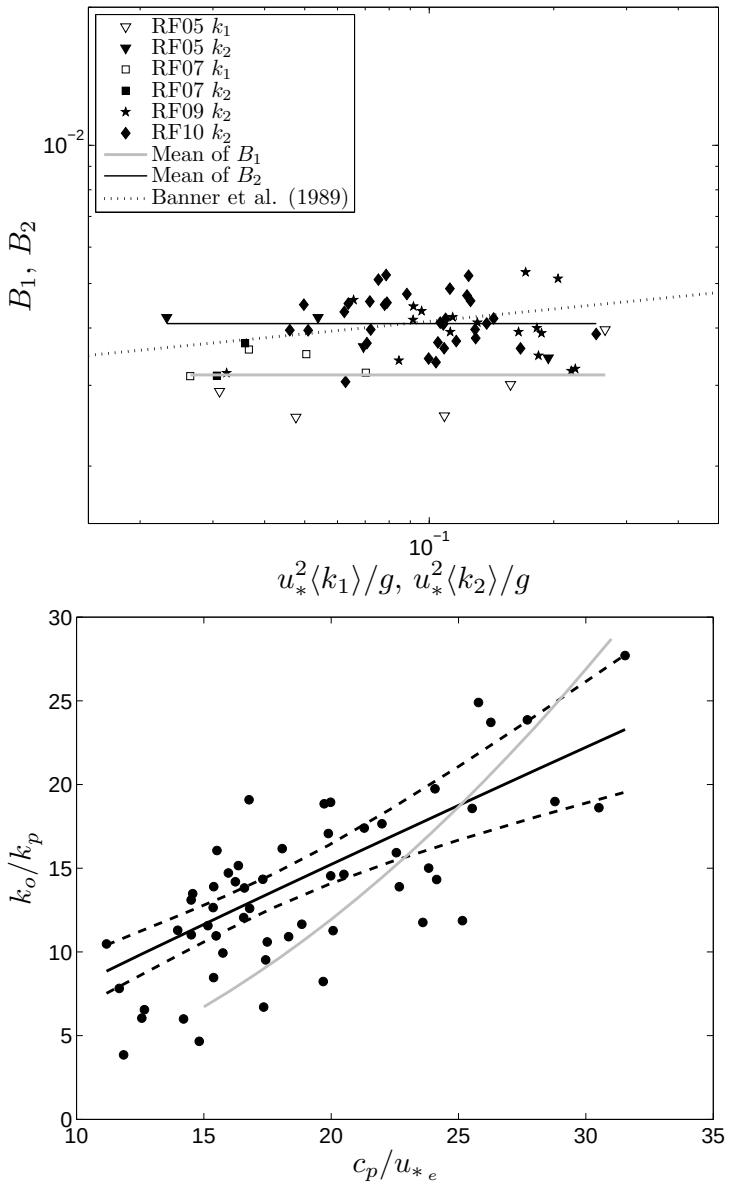

Figure I.15: a) One-dimensional mean saturation B_i versus the nondimensional mean wavenumber component $u_*^2\langle k_i\rangle/g$ (i =1,2), where k_1 and k_2 are the downwind and crosswind wavenumber components, respectively. The averaging interval corresponds to 0.75 rad m^{-1} $< k_i <$ 2 rad m^{-1}. b) Transition wavenumber k_o/k_p between the equilibrium and saturation ranges for the omnidirectional spectra, plotted versus c_p/u_{*_e}. The solid black line shows the estimates using the best-fit to Toba's parameter, including the 95% confidence interval.

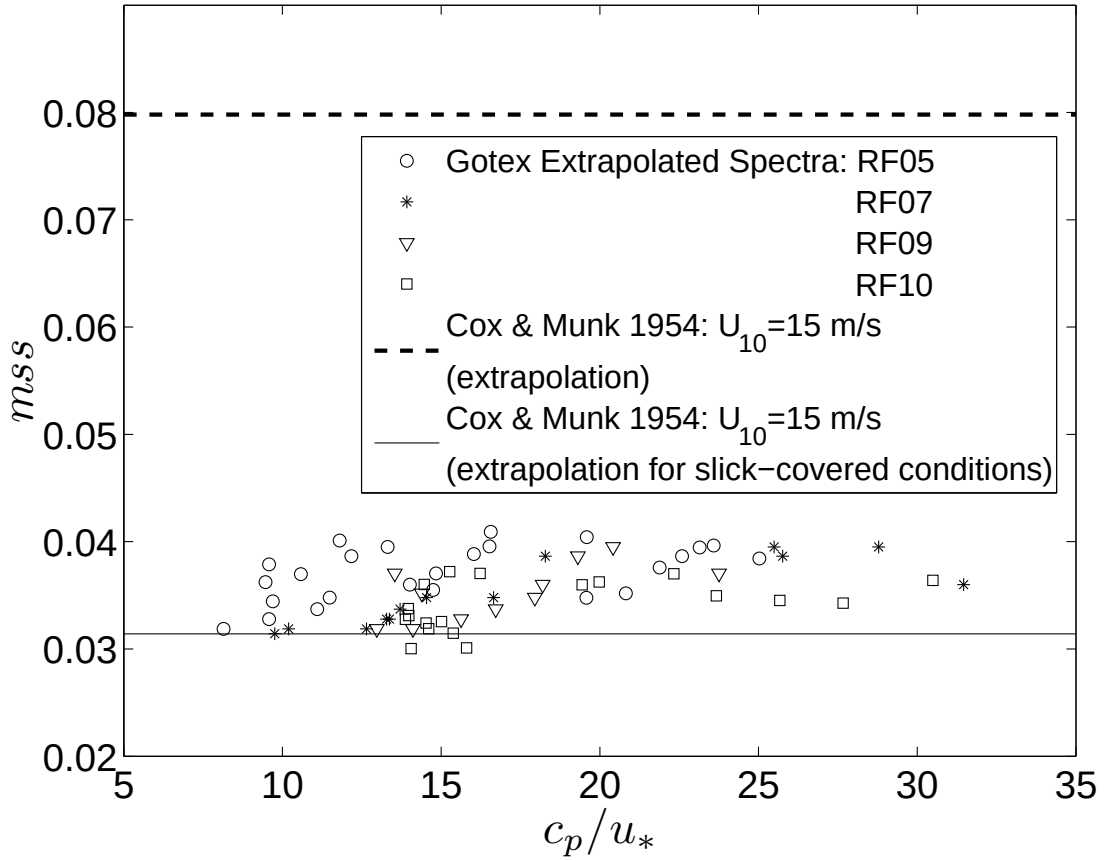

Figure I.16: Mean-squared-slope of the sea surface (mss) versus the local wave wage for wavelengths of 30cm or larger. The various symbols correspond to different research flights. The dashed and solid lines correspond to the extrapolation of the results by Cox and Munk (1954) for surface wind speeds of 15 m s^{-1} under clean and slick-covered conditions, respectively.

can be estimated from the first moment over one side of the spectrum:

$$\sigma_\theta(k) = \frac{\int_0^{\pi/2} F(k,\theta)\theta d\theta}{\int_0^{\pi/2} F(k,\theta) d\theta}, \tag{I.39}$$

where $\theta = 0$ corresponds to the direction of the dominant waves. However, in a situation with turning winds, as in the Gulf of Tehuantepec, the directional spectra may not be symmetric (see for example Long and Resio, 2007). More generally, the directional spreading can be estimated as the average spreading from both sides of the spectrum:

$$\sigma_\theta(k) = \frac{\int_{-\pi/2}^{\pi/2} F(k,\theta)|\theta| d\theta}{\int_{-\pi/2}^{\pi/2} F(k,\theta) d\theta}. \tag{I.40}$$

Figure I.17a shows the observed directional spreading defined by equation (I.40), with each profile corresponding to a bin-average of 9 to 10 spectra according to the range of wave ages shown. The error bars shown correspond to the bin-averaged directional resolution $\langle d\theta \rangle$. The spreading, $\sigma_\theta(k)$, shows a weak dependence (indistinguishable within error bars) on the wave age, with younger waves having a spectrum narrower near the peak and broader for $k/k_p > 2$. The directional spreading is qualitatively in agreement with the observations by Hwang et al. (2000b) for a quasi-steady wave field and the spreading estimated from the $sech^2$ distribution proposed by Donelan et al. (1985).

All previous studies of wind-waves have focused on the directional spreading in the azimuthal direction. In this study, we present an alternative measure, the spreading in the k_2 direction as a function of k_1 (the component along the dominant wave direction) defined by:

$$\sigma_2(k_1) = \left[\frac{\int_{-k_{2_n}}^{k_{2_n}} F(k_1,k_2) k_2^2 dk_2}{\int_{-k_{2_n}}^{k_{2_n}} F(k_1,k_2) dk_2} \right]^{1/2}, \tag{I.41}$$

where $k_{2_n} = 0.5$ rad m^{-1}. When σ_2 is normalized by the peak wavenumber (k_p) and plotted against k_1/k_p the data collapse onto a single curve independent of wave age, as shown in Figure I.17b. This highlights the approximate self-similar

nature of the fetch-limited wave field and suggests the possibility of a simpler parameterization of the directional distribution in the (k_1, k_2) plane.

Socquet-Juglard et al. (2005) used the second moment of the spectrum in the k_2 direction integrated over all wavenumbers to define the mean crest length as:

$$\bar{\Lambda}_c = 2\pi \left[\frac{\int\int F(k_1,k_2) k_2^2 dk_1 dk_2}{\int\int F(k_1,k_2) dk_1 dk_2} \right]^{-1/2}. \tag{I.42}$$

Similarly from equation (I.41), the mean spectral crest length Λ_c with carrier wavenumber k_1 can be defined as:

$$\Lambda_c(k_1) = \frac{2\pi}{\sigma_2(k_1)}. \tag{I.43}$$

Thus, Figure I.17b suggests that, within the range $1 < k/k_p < 5$, Λ_c is linearly related to the carrier wavelength ($\lambda_1 = 2\pi/k_1$). $\sigma_2(k_1)/k_p$ yields a linear regression of:

$$\frac{\sigma_2(k_1)}{k_p} = 0.81\frac{k_1}{k_p} - 0.25. \tag{I.44}$$

I.5.D Bimodal Structure

Previous field studies of directional wind-wave spectra from both temporal and spatial measurements have shown narrow directional distributions around the peak of the spectrum followed by broader distributions toward higher and lower wavenumbers. Both temporal buoy measurements, such as Mitsuyasu et al. (1975), and Hasselmann et al. (1980), as well as the spatio-temporal measurements from a wave-gauge array by Donelan et al. (1985), obtained unimodal spreading functions, whereas airborne spatial measurements (Cote et al., 1960; Holthuijsen, 1983; Jackson et al., 1985b; Wyatt, 1995; Hwang et al., 2000a,b) reported bimodal distributions. However, more recently bimodal structures have also been extracted from buoy observations (Young et al., 1995; Ewans, 1998; Hwang and Wang, 2001) , but the buoy results are strongly dependent on the method used to process the data (Benoit, 1992; Krogstad, 1990). Numerical studies by Banner and Young

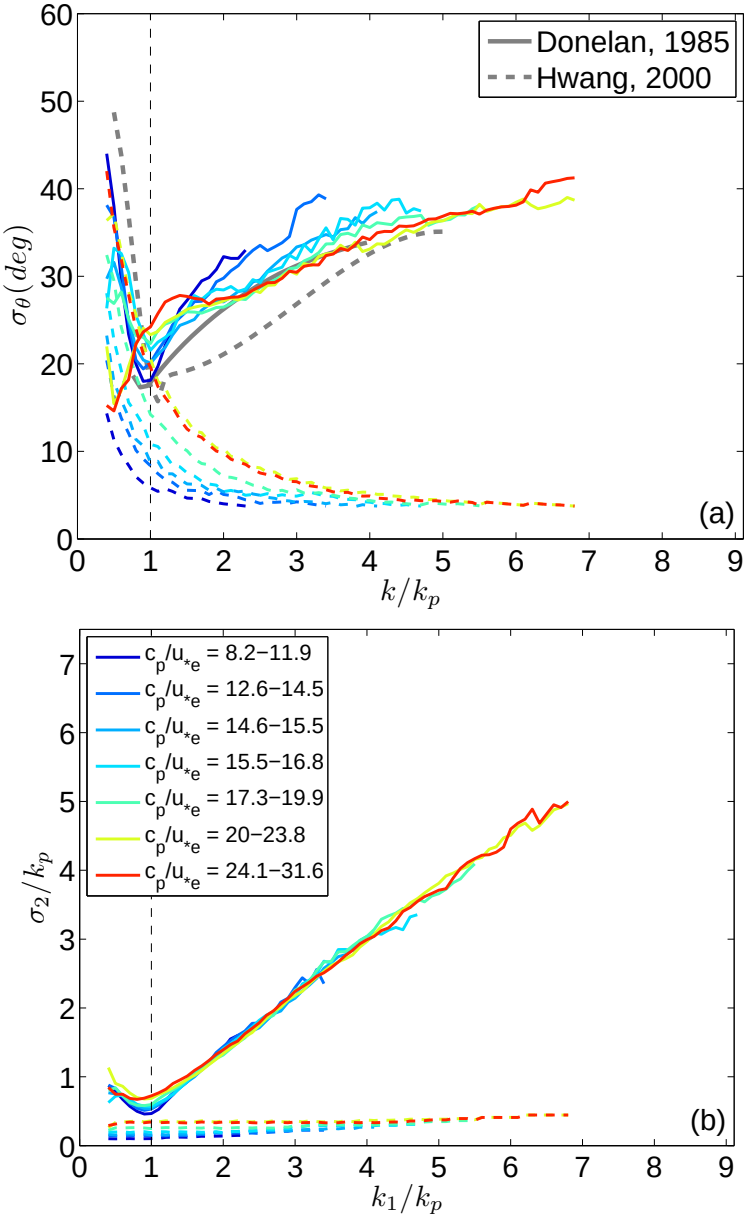

Figure I.17: Directional spreading (a) and spectral width (b) about the axis orthogonal to the dominant waves (k_2) calculated from equations (I.40) and (I.41). The curves shown correspond to bin-averages from 9 to 10 spectra for the range of wave ages (c_p/u_*) shown. The dashed lines show the bin-averaged resolution. The directional spreading estimated from the proposed distribution by Donelan et al. (1985) and the measurements by Hwang et al. (2000b) are shown in solid and dashed lines, respectively.

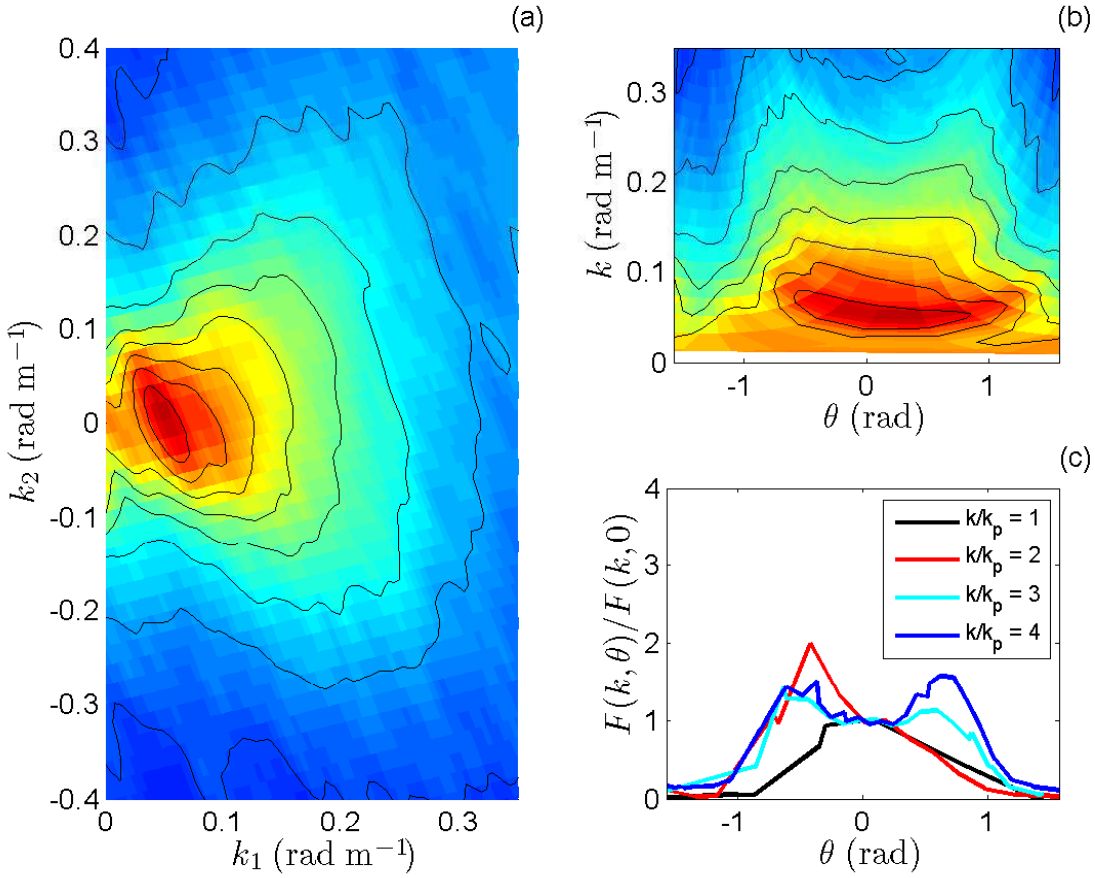

Figure I.18: Sample directional wavenumber spectra corresponding to RF05 from ATM measurements collected at a fetch of 200km. In (a) the spectrum is shown in cartesian representation $F(k_1, k_2)$, and in (b) it is plotted in polar representation $F(k, \theta)$. Panel (c) shows the normalized spectrum in polar coordinates at wavenumbers $k/k_p = 1$, 2, 3, and 4.

(1994), Dysthe et al. (2003), and Pushkarev et al. (2003) suggest that, due to nonlinear resonant interactions, the bimodal azimuthal spreading should be a robust feature of the wave spectrum.

Figure I.18 shows the typical directional wavenumber spectra in cartesian (I.18a) and polar (I.18b) representation. Panel I.18c shows the normalized spectrum $F(k,\theta)/F(k,0)$, where $\theta = 0$ corresponds to the dominant wave direction, for $k/k_p = 1, 2, 3, 4$. Near the spectral speak the directional distribution is unimodal, but becomes bimodal at higher wavenumbers. Following Wang and Hwang (2001), the bimodal structure at high wavenumbers can be characterized with two parameters, the first being the azimuthal separation between the bimodal lobes θ_{lobe} and the second being the average amplitude of the lobes relative to the spectral energy in the wind direction $r_{lobe}(k)$:

$$\theta_{lobe}(k) = \frac{\theta_1(k) + \theta_2(k)}{2} \tag{I.45}$$

$$r_{lobe}(k) = \frac{1}{2}\frac{F(k,\theta_1) + F(k,\theta_2)}{F(k,0)}, \tag{I.46}$$

where $\theta_1(k)$ and $\theta_2(k)$ are the azimuthal location of the maxima at a given wavenumber on each side of the spectrum relative to the dominant wave direction.

The buoy observations of Wang and Hwang (2001) suggest that the bimodal distribution is invariant with wave age. This contrasts with the buoy measurements by Ewans (1998) in conjunction with the results from a wave-gauge array by Long and Resio (2007) which suggest that the bimodal separation of the spectrum is weakly dependent on the wave age. The extensive data set of wavenumber spectra from GOTEX, covering a wide range of wave ages, permits the investigation of the dependence of the bimodal structure on the wave age.

Figures I.19a,b show bin-averages of $\theta_{lobe}(k/k_p)$ and $r_{lobe}(k/k_p)$ from 9 to 10 spectra, over the range of wave ages shown in the legend, with error bars corresponding to bin-averages of the directional resolution and the propagated uncertainty at the 95% confidence interval (see Section I.4I.4.B), respectively. θ_{lobe} shows a weak dependence on the wave age, with younger waves having a larger

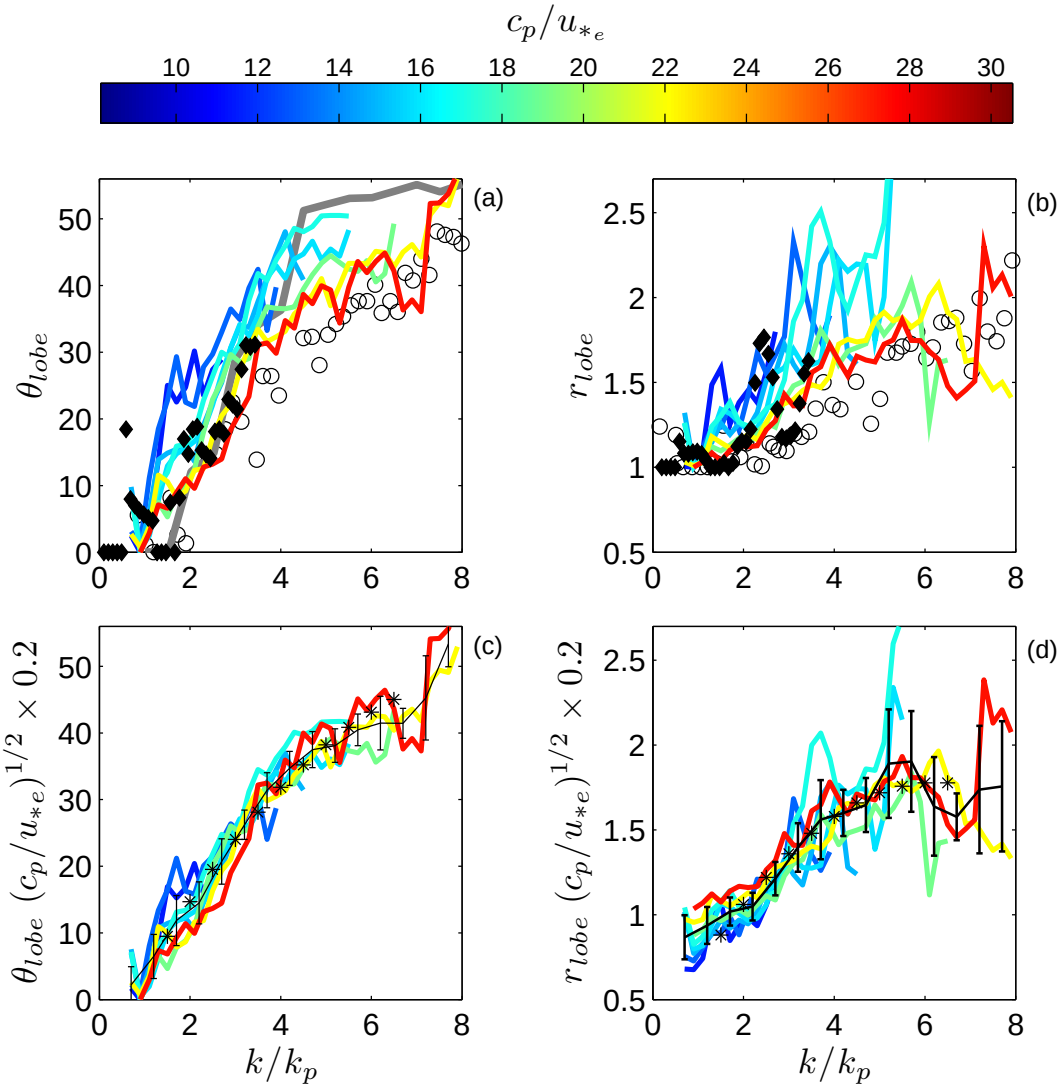

Figure I.19: (a,b) Bin-averaged lobe separation $\theta_{lobe}(k/k_p)$ and relative amplitude $r_{lobe}(k/k_p)$, respectively, over the range of wave ages shown. The curves shown correspond to bin-averages from 9 to 10 spectra for the range of wave ages (c_p/u_*) shown. The open circles correspond to the measurements by Hwang et al. (2000b). The solid gray line shows the field measurements by Long and Resio (2007). The black diamonds correspond to a sample spectrum obtained from a crosswind track during RF05, where c_p/u_* =12. In (c,d) θ_{lobe} and r_{lobe} are scaled with $(c_p/u_{*e})^{1/2}$. The solid black line is a bin-average with error bars of one standard deviation. The black asterisks are the polynomial best-fits from equations (I.47-I.48).

lobe separation, qualitatively consistent with Ewans (1998). r_{lobe} also shows a dependence on wave age, differing from the observations of Wang and Hwang (2001). The values of θ_{lobe} and r_{lobe} for mature waves reported by Hwang et al. (2000b) (open circles) show qualitative agreement with this study. Also shown (solid gray line) are the measurements of θ_{lobe} by Long and Resio (2007) for young waves, having an inverse wave age of $1.6 < U_{10}/c_p < 3.4$ corresponding to $7 < c_p/u_* < 16$ assuming a drag coefficient of 1.5×10^{-3}. Finally, the black diamonds are from a spectra measured while flying perpendicular to the wind, near shore, where c_p/u_{*_e} was approximately 12. The bimodal structure given by the spectrum from the crosswind leg shows qualitatively the same behavior as the downwind spectra, thus the bimodal distribution is irrespective of the flight orientation relative to the waves.

When θ_{lobe} and r_{lobe} are multiplied by $0.2\times(c_p/u_{*_e})^{1/2}$, both sets of curves collapse reasonably well, see Figures I.19c,d. Second-order polynomial fits, for $1.5 < k/k_p < 6.5$, yield:

$$\theta'_{lobe} = 0.2 \times (c_p/u_{*e})^{1/2}\theta_{lobe} = -0.736(c_p/u_{*e})^2 + 12.9(c_p/u_{*e}) - 8.35 \quad \text{(I.47)}$$

$$r'_{lobe} = 0.2 \times (c_p/u_{*e})^{1/2} r_{lobe} = -0.04(c_p/u_{*e})^2. + 4.9(c_p/u_{*e}) + 0.22 \quad \text{(I.48)}$$

I.6 Wavenumber Spectrum Parameterization

In this section, the observed self similar features of the wind-wave spectra are used to develop a parameterization of the k_1 spectrum with dependence on the fetch and the friction velocity. Figure I.20a shows typical k_1 spectra times k_1^3 versus k_1/k_p, suggesting that ϕ_1 can be approximated by a double power law model, with a spectral tail $\propto k_1^{-3}$ and the forward face $\propto k_1^4$, with a peak enhancement function between the two. Based on the JONSWAP peak enhancement function

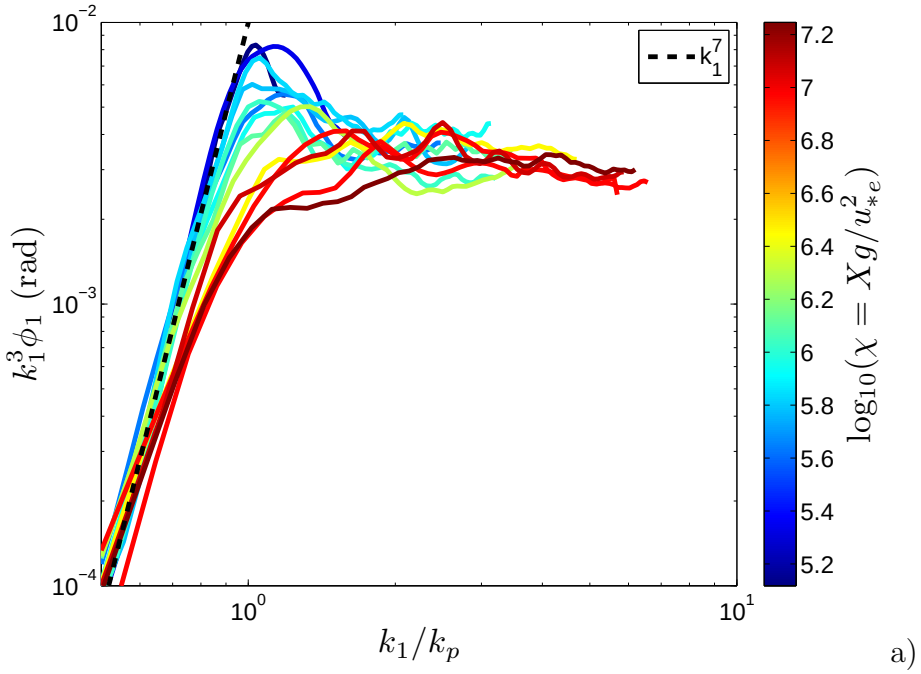

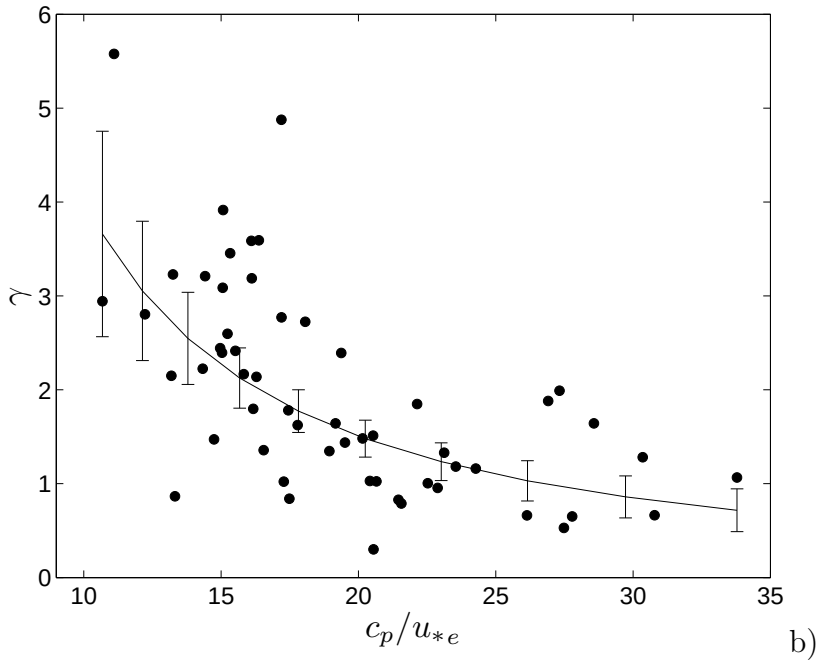

Figure I.20: a) Typical k_1 spectra times k_1^3 versus k_1/k_p for RF05 at various nondimensional fetches $Xg/u_{*_e}^2$, ranging from 10^5 to 10^7. The dashed black line is a reference spectral slope $\propto k_1^7$. b) k_1 spectrum peakedness factor γ versus the effective wave age. The solid line corresponds to the best-fit with 95% confidence intervals.

(Hasselmann et al., 1973), the following spectral parameterization is proposed:

$$\phi_1(k_1, X, u_{*_e}, g) = \frac{B_1 \gamma^{\exp \frac{-(1-(k_1/k_p)^2)^2}{2\sigma^2}}}{k_1^3 + k_p^3(\frac{k_1}{k_p})^{-4}}, \tag{I.49}$$

where B_1, σ, and γ are empirical parameters which may depend on the dimensionless fetch, or the wave age. B_1 is the degree of saturation in the k_1 direction, γ and σ represent the amplitude and width of the peak enhancement, respectively. Figures I.13 and I.20b show B_1, immediately after the peak, and γ against the effective wave age, both parameters decrease with increasing u_{*_e}/c_p according to following relations:

$$B_1 = \quad 7.01 \times 10^3 (c_p/u_{*_e})^{-3.2 \pm 0.2 \times 10^{-1}} \tag{I.50}$$

$$\gamma = \quad 1.05 \times 10^2 (c_p/u_{*_e})^{-1.42 \pm 0.07}, \tag{I.51}$$

with uncertainties corresponding to the 95% confidence intervals. The fit to the peakedness factor reaches unity at about $c_p/u_* = 28$, and continues to decrease at the larger wave ages, giving rise to a peak reduction. Of the other parameters, σ was kept constant with a value of 0.5, B_1 was estimated as described in Section (I.5I.5.B), and γ was fitted through standard iterative nonlinear regression algorithms (Bates and Watts, 1988). The spectral peakedness reduction with increasing wave age is consistent with the results by Mitsuyasu (1981), Donelan et al. (1985), and Long and Resio (2007) for frequency spectra. Figure I.21 shows a direct comparison between observed k_1 spectra and the parameterization using the measured values of k_p and $u*_e$ as input. The parametrization of the spectrum can reproduce the measurements fairly well (within the uncertainty at the 95% confidence interval) at young to intermediate wave ages. Towards full development, at very large fetches, the model cannot reproduce the measurements below the spectral peak because the forward face of the measured spectrum falls off less steeply than the imposed k_1^4 slope. This may be attributed to the reduced spectral resolution at low wavenumbers or the presence of swell from the North Pacific, orthogonal to the local wind sea outside the Gulf of Tehuantepec.

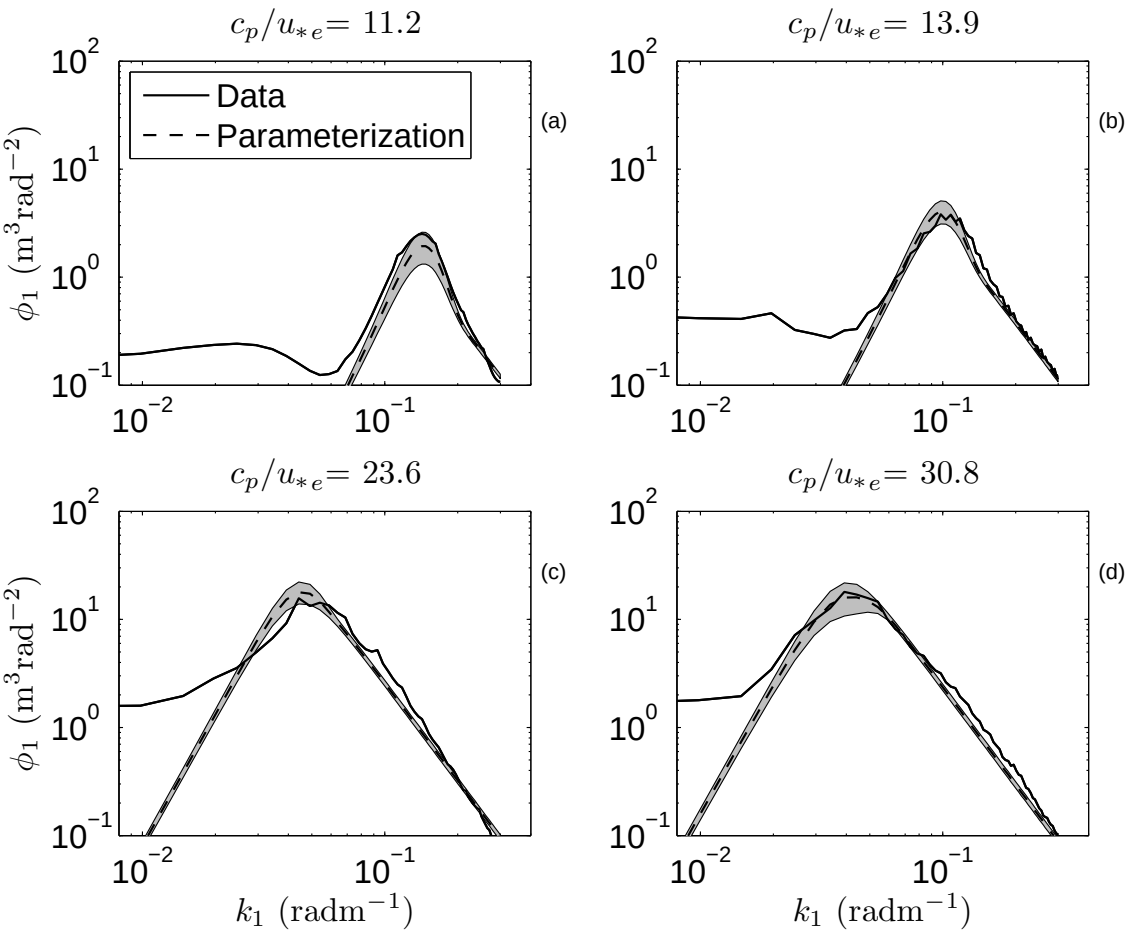

Figure I.21: Comparison between measured (solid lines) and parameterized k_1 spectra (dashed lines) according to equations (I.49-I.51). The gray shaded area represents the 95% confidence intervals.

I.7 Discussion and Conclusions

Our wind-wave measurements collected in the Gulf of Tehuantepec during strong offshore wind conditions are unique for having one- and two-dimensional wavenumber spectra, including the winds and turbulent fluxes, in fetch-limited conditions covering a wide range of wave ages, from very young to fully developed seas. Previous similar wind-wave studies are limited to frequency spectra and the mean winds, thus relying on parameterizations of the drag coefficient to infer the wind stress. Wind-wave measurements in the wavenumber domain are relatively rare in the literature, and those available are limited by the range of environmental conditions, primarily because of the difficulties involved in the acquisition process. However, wavenumber wind-wave observations are to be preferred over frequency spectra which can be distorted at high frequencies due to the Doppler shift induced by the steeper and longer dominant waves (Banner, 1990a; Kitaigordskii et al., 1975).

Our measurements conform with the well established fetch relations from previous observations. In particular, we find good agreement with the reanalysis by Kahma and Calkoen (1992) for waves generated during a stably stratified atmospheric boundary layer. Most of our measurements were collected in stable atmospheric conditions due to the strong upwelling induced by the strong offshore wind forcing bringing cooler water to the surface. In the context of wind-wave modeling, this suggests that to leading order the effects due to spatial changes in the wind field in GOTEX must be small compared to the net forcing, which includes the wind forcing, nonlinear energy flux due to resonant interactions and dissipation due to wave breaking. This is consistent with the numerical experiments by Young et al. (1987), where it was shown that for changes in wind direction of less than 60^o the entire spectrum rotated into the new wind direction, with high frequency components adjusting faster than the low frequencies. The rotation of the spectrum was directly forced by the wind input in the new wind direction, while

the dissipation was responsible for damping out the components in the old wind direction and the nonlinear transfer ensured a smooth the rotation preventing the appearance of the secondary peaks.

The measured wavenumber spectra exhibit self-similar properties having a weak, but significant, dependence on the effective wave age. The omnidirectional spectrum, within the equilibrium range, follows a power-law approximately proportional to $k^{-5/2}$. Following Toba's scaling, β is not constant, showing a increasing trend with increasing effective wave age, this is qualitatively consistent with frequency measurements by Donelan et al. (1985) and Resio et al. (2004). However, there is a clear discrepancy in the overall magnitude of β among the various observations. This could very well be attributed to differences in atmospheric stability, which are known affect growth rate of the wave field within a factor of 2, see for example Kahma and Calkoen (1992) and Young (1998). The GOTEX measurements, with lower values of β, were collected mainly under a stably stratified boundary layer. In contrast, the measurements of Donelan et al. (1985) include both stable and unstable conditions (Kahma and Calkoen, 1992). The measurements of Resio et al. (2004), although not explicitly addressed in their text, must also include data in both situations since they were collected in numerous locations around the world.

While the one-dimensional k_1 spectrum shows a consistent power-law proportional to k_1^{-3} over a wide range of wavenumbers, the k_2 spectrum is better described by two power-laws, $k_2^{-5/2}$ at low wavenumbers and k_2^{-3} at high wavenumbers. In the region immediately after the peak, the one-dimensional k_1 saturation (B_1) decreases with increasing effective wave age. However, at high wavenumbers within the saturation range, B_1 and B_2 are almost independent of the local forcing, with $B_2 = 4.1 \times 10^{-3}$ and $B_1 = 3.2 \times 10^{-3}$. This indicates that at such scales the directional distribution in polar representation may be slightly bimodal, this is in accord with the mean squared slope (mss) analysis by Hwang and Wang (2001),

where it was shown that a bimodal directional distribution is need at very high wavenumbers in order to reproduce the observed ratio of crosswind to upwind mss by Cox and Munk (1954) for a slick-covered surface. Moreover, although not clearly resolved from the uncertainty, the two-dimensional spectra reported by Banner et al. (1989), at higher wavenumbers, also show bimodal directional distributions (see their Figures 6 and 7).

By assuming an isotropic directional distribution for the saturation range, the omnidirectional saturation B becomes $2B_{1,2}$ (Phillips, 1977, p. 150) which is 30% lower than the saturation values reported by Forristall (1981) based on a large data set of frequency spectra over a similar range of forcing conditions and is in close agreement with the mean values reported by Banner et al. (1989). Extrapolation of the equilibrium spectrum to match the constant saturation region gives a transition wavenumber, k_o, which separates the equilibrium and saturation ranges. k_o/k_p increases with wave age, ranging between 10 and 23, differing from the results by Forristall (1981) that give a transition exclusively dependent on the local forcing. These results also contrast with the equilibrium range model of Hara and Belcher (2002) which predicts the power law transition at wavenumbers as high as 50 rad m^{-1}or greater.

The directional spreading and the normalized width of the spectrum in the direction orthogonal to the wind are almost independent of wave age. Both the amplitude and separation of the lobes decrease with increasing wave age, both parameters were shown to scale with $(c_p/u_{*_e})^{1/2}$. The observed dependence of θ_{lobe} on the wave age is more or less consistent with Ewans (1998) and Long and Resio (2007); however, to our knowledge no previous work had found a clear relationship between r_{lobe} and the wage age. Finally, the self similar features of the observed spectra were used to formulate a parameterization of the k_1 spectrum with parametric dependence on the effective friction velocity and fetch.

II

Numerical Simulations of Wind-Wave Spectra in the Gulf of Tehuantepec

II.1 Abstract

The Gulf of Tehuantepec is well known for having strong offshore winds, which occur predominantly during the winter months, when significant atmospheric pressure differences develop between the Gulf of Mexico and the Pacific Ocean, forcing winds through a mountain gap at the head of the gulf. During the Gulf of Tehuantepec Experiment (GOTEX), conducted in February 2004, we made surface-wave measurements using a scanning LIDAR (Airborne Topographic Mapper, ATM) on the NSF/NCAR C-130 aircraft during fetch-limited conditions with winds speeds ranging from 10 to 20 m s^{-1}. We present direct comparisons between the observed evolution of the wave field and numerical simulations using the saturation-based dissipation function proposed by Alves and Banner (2003). In particular, we compare the observed and computed evolution of the directional spectra for fetch-limited conditions under realistic wind forcing. All model sim-

ulations were carried out using the Alves and Banner (2003) dissipation parameterization along with exact computations of the nonlinear energy transfer due to four-wave resonant interactions (Tracy and Resio, 1982; Vledder, 2006) and the wind input functions by Snyder et al. (1981) and Yan (1987). The agreement of the integral parameters, the total energy and the wavenumber component at the spectral peak, between the observations and the simulations is within the typical scatter of field observations. The Alves and Banner (2003) dissipation formulation can maintain power-law behaviors within the tail of the omnidirectional and k_1 spectrum, consistent with the observations. However, the model spectra are always narrower than the observations by 10° to 15°. Similarly, the bimodal distribution produced in the model spectra exhibits a separation and amplitude of the lobes that is consistently narrower than the observations. We find a consistent characterization of the bimodal distribution for the measured and simulated spectra with respect to the wave age, where the average lobe separation (θ_{lobe}) and lobe amplitude (r_{lobe}) collapse when scaled with $(c_p/u_*)^{1/2}$. Another robust and consistent feature of the observed and computed spectra is the reduction of the peak enhancement with increasing wave age. The comparison between the observations and the numerical simulations highlights some of the issues associated with the source term balance in the tail of the spectrum. The performance of the model suggests that the saturation-based dissipation is a good first step towards realistic simulations of the wind-wave spectrum, but further work is needed to address the differences between measurements and the model.

II.2 Introduction

Numerical modeling and numerical prediction of surface gravity waves have improved our understanding of the various physical processes involved in wind-wave generation and evolution. The three main physical processes are the direct forcing by wind, the nonlinear energy transfer due to wave-wave interac-

tions, and the energy dissipation mainly due to wave breaking. Although our present knowledge of the wind input is far from being complete, there are several available field and laboratory measurements that give consistent growth rates within a factor of 5; for example, the measurements by Snyder et al. (1981), the collation by Plant (1982), and the laboratory and field measurements by Donelan (1987), among others. In contrast, the full expression for the nonlinear energy transfer due to four-wave resonant interactions has been known for a long time (Hasselmann, 1963; Webb, 1978). However, the energy dissipation due to wave breaking used in numerical wind-wave models has been formulated based on conceptual physical arguments (Hasselmann, 1974), leaving a few free parameters, which are tuned numerically by trial and error until the model can reproduce the available observations (Komen et al., 1984).

Present numerical prediction models that run on a daily basis at global and regional scales, commonly referred to as operational models, are limited to coarse spectral and spatial grids and with parameterizations or approximations of the nonlinear energy transfer due to wave-wave interactions constrained by the computational time. Thus present operational wind-wave models can only predict the standard integral parameters, which are the wave height, period, and direction of the dominant waves. Due to the large number of operations required, models with good spatial and spectral resolution, that use the complete computations of nonlinear energy transfer have been limited to academic investigations. The first study of this kind was by Komen et al. (1984), which focused on the dynamical balance of the spectrum for fully developed seas, which used a variant of the dissipation function by Hasselmann (1974). A subsequent study by Banner and Young (1994) showed that the model by Komen et al. (1984) could not reproduce the observations when applied to developing waves under idealized fetch-limited conditions. They concluded that a new dissipation function was needed to improve the model performance. A recent investigation by Alves and Banner (2003): "AB"

proposed an improved dissipation parameterization which can accommodate several wind input functions with the full computations of S_{nl}. The simulations by AB reproduce the integral parameters from field observations over a wide range of fetches, including the asymptotic behavior near full development. The improved dissipation function provided a good control over the tail of the spectrum, at wavenumbers between $6.25k_p$ and $25k_p$, where k_p corresponds to the wavenumber at the spectral peak. Recent advances on field measurements of the wave breaking probability have reported a threshold behavior with respect to the spectral saturation normalized by the directional spreading of the spectrum (Banner et al., 2002), which are being incorporated in a parameterization of spectral dissipation as a modification to the AB dissipation function (Banner and Morrison, 2006). Since the authors did not provide the necessary information to reproduce their results, the modifications to the AB dissipation function were not considered in this study.

The fetch-limited wind-wave observations collected during the Gulf of Tehuantepec Experiment (GOTEX) in February 2004 represent the largest available data set of wavenumber spectra, including winds and friction velocities, with good directional resolutions over a wide range of fetches and are described in detail in Romero and Melville (2008a): "RM". Thus, the GOTEX measurements provide an opportunity to test the AB model under realistic wind forcing, beyond just comparisons with the typical integral parameters. In this study we present a comparison between the measured spectra during GOTEX and numerical simulations using the AB model with good spectral resolution. All the simulations were carried out using the computational framework of WaveWatch III (WW3), version 2.22. The structure of the paper is as follows. In Section 2 we present an overview of numerical wind-wave models. In Section 3 we describe the wind-wave model used for the simulations. In Section 4 two-dimensional simulations over the Gulf of Tehuantepec are compared to the GOTEX observations. The results are summarized and discussed in Section 5.

II.3 Background

Spectral models for deep-water wind-waves are based on the radiative transfer equation:

$$\frac{\partial N(\mathbf{k})}{\partial t} + C_g \cdot \nabla N(\mathbf{k}) = S_{in} + S_{ds} + S_{nl} \tag{II.1}$$

where $N(\mathbf{k})$ is the wave action spectral density, $F(\mathbf{k})/\omega$, $F(\mathbf{k})$ is the directional wavenumber spectrum, ω is the radial frequency, C_g is the group velocity according to the linear dispersion relationship ($w^2 = gk$), and g is the gravitational acceleration. S_{in} is the wind input source function, S_{ds} corresponds to the wave energy dissipation, primarily due to wave breaking, and S_{nl} is the nonlinear energy transfer due to wave-wave interactions. State-of-the-art wind-wave models can do a very good job of predicting the total energy and peak frequency of the dominant waves under idealized conditions, which include spatially homogeneous and stationary winds blowing over an infinite area or off an infinite straight coastline. A recent study by Ardhuin et al. (2007) compares buoy observations of young fetch-limited waves in slant-fetch conditions against various parameterizations commonly used in present wind-wave models, with one of the most important outcomes being the inability of the models to correctly handle mixed wind-sea and swell conditions.

Following is a brief review of the parameterizations used in present wind-wave models. Hasselmann (1963) derived the first analytical expression of S_{nl} for deep water-waves satisfying the following resonant conditions:

$$\begin{aligned} \mathbf{k}_1 + \mathbf{k}_2 &= \mathbf{k}_3 + \mathbf{k}_4 \\ \omega_1 + \omega_2 &= \omega_3 + \omega_4, \end{aligned}$$

where the rate of change of wave action density due to all possible four-wave resonant interactions is given by:

$$\begin{aligned} \frac{\partial N_1}{\partial t} = \int\int\int G(\mathbf{k}_1, \mathbf{k}_2, \mathbf{k}_3, \mathbf{k}_4)\delta(\mathbf{k}_1 + \mathbf{k}_2 - \mathbf{k}_3 - \mathbf{k}_4)\delta(\omega_1 + \omega_2 - \omega_3 - \omega_4) \\ \times[N_1 N_3(N_4 - N_2) + N_2 N_4(N_3 - N_1)]d\mathbf{k}_2 d\mathbf{k}_3 d\mathbf{k}_4 \end{aligned} \tag{II.2}$$

where $N_i = N(\mathbf{k}_i)$, is the wave action density at $\mathbf{k}_i$, and G is the interaction coefficient (Hasselmann, 1962, 1963; Webb, 1978). Its worth mentioning that nonlinear energy transfer also occurs for nonresonant interactions, but such interactions occur as transients at shorter time scales which are not important for the slow evolution of the wave field for periods of 10 dominant waves or more (Janssen, 2003). The number of calculations required to compute S_{nl} is very large, thus the full solution of S_{nl} has been limited to research applications. Since Hasselmann (1963), there have been many efforts to increase the computational speed of S_{nl} by projecting the six dimensional integral to three dimensions (Webb, 1978). The wave-wave interactions generally transfer energy and momentum from intermediate wavenumbers to both higher and lower wavenumbers (Webb, 1978). Most of the transfer is toward lower wavenumbers just before the peak of the spectrum and toward high wavenumbers in a direction $\pm 45^o$ off the downwind direction. The numerical simulations of Banner and Young (1994) and Pushkarev et al. (2003), using a spectral model that computed S_{nl} exactly showed that the wavenumber spectrum develops a bimodal angular distribution at wavenumbers higher than the spectral peak. According to Young and Vledder (1993), four-wave resonant nonlinear interactions are of central importance in the development of the spectrum, smoothing out any perturbation (Resio and Perrie, 1991) and controlling the directional spreading.

One of the first effective theories of wind-wave generation was developed by Miles (1957), based on a shear flow instability mechanism through critical-layer interaction of the surface waves and the wave-induced pressure. Following the theoretical framework of Miles (1957), Snyder et al. (1981) examined field measurements of the pressure above the surface waves, and reported growth rates much larger than the predictions by Miles' theory. The theory by Miles (1957) assumed a drag coefficient independent of wave development, which is inconsistent with the measurements by Donelan (1982), where it was shown that the observed drag coefficient (C_d) was dependent on sea state. Janssen (1989, 1991) proposed

an analytical theory, as an extension to Miles (1957) theory, that accounts for the impact of the wave induced stress (τ_w) on the drag coefficient and consequently on S_{in}. Tolman and Chalikov (1996) introduced a wind input function consistent with Janssen's growth rates but also gave negative input rates for waves traveling faster than the wind or at large angles from the mean wind direction. This parameterization of S_{in} was obtained from numerical simulations of the wave boundary layer over monochromatic waves (Chalikov and Belevich, 1993; Burgers and Makin, 1993; Chalikov, 1986).

The dissipation function S_{ds} is the least understood source function. The first most widely used form of S_{ds} was proposed in general form by Hasselmann (1974). This function assumes that the loss due to wave breaking is linearly related to spectrum. In contrast, the equilibrium model by Phillips (1985) required a nonlinear form of S_{ds} to balance the source terms (S_{in}, S_{nl} and S_{ds}). The numerical experiments by Komen et al. (1984) showed that a variant of Hasselmann's S_{ds} could balance the source terms for fully developed conditions, producing frequency spectra consistent with the empirical Pierson-Moskowitz spectrum Pierson and Moskowitz (1964) for fully developed seas. According to Komen et al. (1984), this wind-wave model included a parametric tail, proportional to ω^{-5} at frequencies greater than 2.5 times that at the peak of the spectrum, ω_p, to give faster computation speeds with no significant effects on the spectrum. Banner and Young (1994) extended the numerical work of Komen et al. (1984) to test the sensitivity to modifications of the adjustable parameters of S_{ds} and the effect of the prognostic tail on the energy containing region of the spectrum. They performed fetch-limited numerical experiments using as diagnostics the JONSWAP fetch relations (Hasselmann et al., 1973), the high frequency spectral slope and energy level of Banner (1990a), and the directional spreading of Donelan et al. (1985). Their results showed that the evolution of the spectrum was sensitive to the prognostic tail, and that the model was not able to reproduce the JONSWAP observations regardless

of the modifications made to the free parameters of S_{ds}. The conclusion was that an alternate form of S_{ds} is required to reproduce the observations. A recent study by AB proposed a saturation-based nonlinear form of S_{ds}. Their numerical experiments showed an improvement, reproducing the integral parameters and the high wavenumber spectral shape and energy density of the spectrum. However, they could not accurately reproduce the empirical bimodal distribution for fully developed seas reported by Hwang et al. (2000b).

II.4 The Model

In this study the model WaveWatchIII (WW3), version 2.2, is used as the numerical framework to carry out the numerical wind-wave simulations. WW3 was developed at the National Centers for Environmental Prediction (NCEP) (Tolman, 2002), and is used operationally to produce global and regional forecasts on a daily basis at NCEP, and at the Fleet Numerical Meteorology and Oceanography Center (FNMOC). The source code is written in Fortran 90, and is fully parallelized to work across multiple processors with the Message Passing Interface (MPI).

The model has several explicit propagation schemes available. Following AB03, we used the first-order upwind scheme with fine spatial, temporal, and spectral resolutions. For the time-step integration, the default semi-implicit scheme without limiters was used for all the simulations presented here. Integration limiters are commonly used in wind-wave model simulations to ensure numerical stability by limiting the maximum change in energy or action density at each spectral component. In order to avoid any artificial effects on the shape of the spectrum, the integration limiters were turned off, but the solutions were free of integration instabilities at all times.

The model grid is in the frequency domain, in polar coordinates (ω, θ), having a constant bandwidth ($d\omega/\omega = \text{constant}$). In this study, the model spectra produced from the simulations were converted to the wavenumber domain (k, θ)

using the linear dispersion relationship for deep-water waves,

$$F(k,\theta) = \frac{1}{k}\frac{\partial \omega}{\partial k}\varphi(\omega,\theta) \quad \text{(II.3)}$$

$$= \frac{g^{1/2}}{2k^{3/2}}\varphi(\omega,\theta), \quad \text{(II.4)}$$

where φ is the directional frequency spectrum.

II.4.A Physics

All simulations were carried out with exact computations of the nonlinear energy transfer due to four-wave resonant interactions using the Webb-Resio-Tracy algorithm (Webb, 1978; Tracy and Resio, 1982) adapted by Vledder (2006) (version 5), referred to hereafter as S_{nl}^X. All of the available settings were kept as defauls. The computations of S_{nl}^X use a parametric tail of the form $\varphi(\omega,\theta) \sim \omega^{-5}$, or $F(k\theta) \sim k^{-4}$, for for frequencies larger than 0.75 times the maximum resolved frequency.

The wind input parameterization used was either Snyder et al. (1981) or Yan (1987) (hereafter referred to as S_{in}^S and S_{in}^Y, respectively), which are given by:

$$S_{in}^S = 0.25\frac{\rho_a}{\rho_w}\left(\frac{28u_*}{c}\cos\theta - 1\right)F(k,\theta)w \quad \text{(II.5)}$$

$$S_{in}^Y = \left[\left(0.04\left(\frac{u_*}{c}\right)^2 + 0.00544\frac{u_*}{c} + 0.000055\right)\cos\theta - 0.00031\right]F(k,\theta)w, \quad \text{(II.6)}$$

where ρ_a and ρ_w are the air and water densities, respectively, u_* is the friction velocity of the air, and c is the wave phase speed according to the linear dispersion relationship. Both functions of S_{in} give comparable growth rates for long, weakly forced, waves, but the wind forcing S_{in}^Y is larger than S_{in}^S for strongly forced short waves, having growth rates comparable to Plant (1982). The energy dissipation due to wave breaking was calculated according to the saturation-based function by AB:

$$S_{ds}^{AB}(k,\theta) = -C_{ds}\left(\frac{B(k)}{B_r}\right)^{p/2}(E_{tot}k_p^2)^m\left(\frac{k}{\overline{k}}\right)^n \omega F(k,\theta), \quad \text{(II.7)}$$

where $B(k) = \phi(k)k^3$ is the azimuth integrated saturation, with

$$\phi(k) = \int_{-\pi}^{\pi} F(k,\theta)kd\theta, \tag{II.8}$$

the total energy density or variance is given by:

$$E_{tot} = \langle \eta^2 \rangle = \int_{k_o}^{k_f} \phi(k)dk, \tag{II.9}$$

the lower and upper limits of the spectral grid are k_o and k_f, respectively. The wavenumber component at the spectral peak is k_p, the mean wavenumber component

$$\bar{k} = \frac{\int_{k_o}^{k_f} \phi(k)kdk}{Etot}, \tag{II.10}$$

and

$$p = \frac{po}{2}(1 + \tanh(10[\frac{B(k)}{B_r}]^{1/2} - 1)). \tag{II.11}$$

The coefficients C_{ds} and p_o, the exponents m and n, and the threshold saturation B_r were tuned numerically by AB using the empirical model of the spectrum by Banner (1990a). The numerical tuning procedure was repeated with using various wind input parameterizations, all simulations used the original Tracy and Resio (1982) model to compute S_{nl}^X. In this study most of the dissipation parameters used in the simulations were taken from AB, see Table II.1. The only parameter modified from its original value was C_{ds}, to be used with S_{in}^Y, which had to be reduced by a factor of ten in order for the model to reach the Pierson-Moskowitz limits at long fetches.

II.4.B Model Implementation and Testing

The exact computation of S_{nl} is extremely demanding, resulting in a significant constraint for large simulations. The simplest and least computationally demanding simulations correspond to duration-limited runs, which assume spatially homogeneous winds over and infinite ocean, using a single grid point to calculate and integrate the source terms forward in time without spatial propagation,

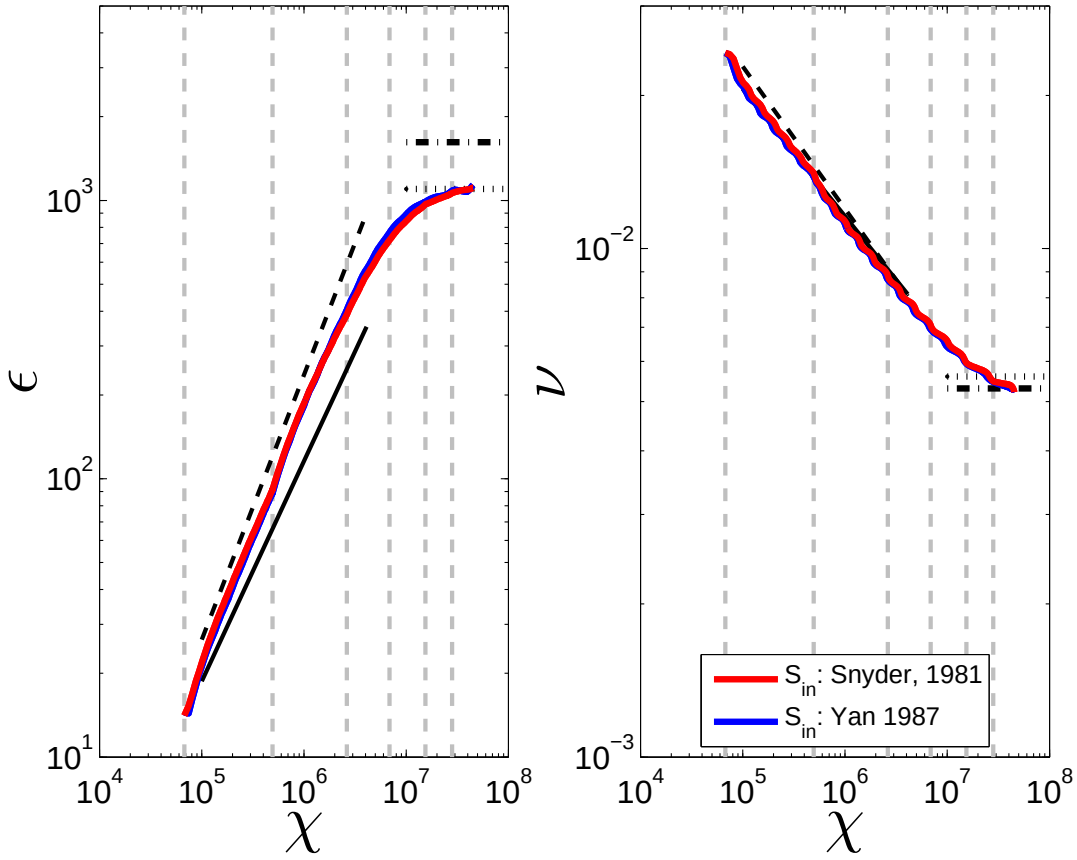

Figure II.1: Nondimensional energy and peak frequency versus nondimensional fetch. The red and blue lines correspond to simulations using the Snyder et al. (1981) and Yan (1987) wind input functions, respectively. The solid and dashed black lines correspond to the reanalysis by Kahma and Calkoen (1992) for stable and unstable atmospheric stratification, respectively. The dotted and dashed-dotted lines correspond to the limits for a Pierson-Moskowitz spectrum (Komen et al., 1984) and those by AB, respectively. The gray dashed lines indicate the location of the first grid point of each nested grid.

Table II.1: Spectral dissipation parameters used for the numerical simulations. Note that all of the parameters, except for C_{ds} with S_{in}^{Y}, are exactly as reported by AB.

S_{in}	C_{ds}	B_r	p_o	m	n
Snyder et al. (1981)	3.7×10^{-4}	3.8×10^{-3}	4	0.30	1
Yan (1987)	3.25×10^{-4}	4.12×10^{-3}	8	0.35	2

starting from some prescribed initial conditions. In this study, duration-limited simulations were valuable for implementing and testing the model.

The main goal of this study is to compare the fetch-limited wind-wave observations against two-dimensional numerical simulations with high spectral resolution. For fetch-limited simulations, the limitation imposed by the computations of S_{nl}^{X} require the use of nested grids. The model implementation in a one-way nested configuration was first tested with one-dimensional fetch-limited runs (see grid details in Table II.2), and the spatial resolution was gradually increased with increasing fetch. The one-dimensional simulations were carried out in sequence, running the model with a single grid at a time, starting at the shortest fetch and progressing towards longer fetches. For each run, the model was run until an approximatly stationary solution was reached. The output at the last grid point (at the longest fetch) was saved after each time-step integration to be used as a boundary condition for the next sequential run. The boundary conditions remain constant after reaching the end of the file, thus assuming stationarity. All simulations were initialized with a JONSWAP spectrum with a $\cos^2\theta$ directional distribution. Following Lewis and Allos (1990), the nondimensional energy and peak frequency was adjusted to match the composite growth curves by Kahma and Calkoen (1992), at short to intermediate fetches, and the Pierson-Moskowitz limits (Komen et al., 1984), at long fetches. Figure II.1 shows the nondimensional

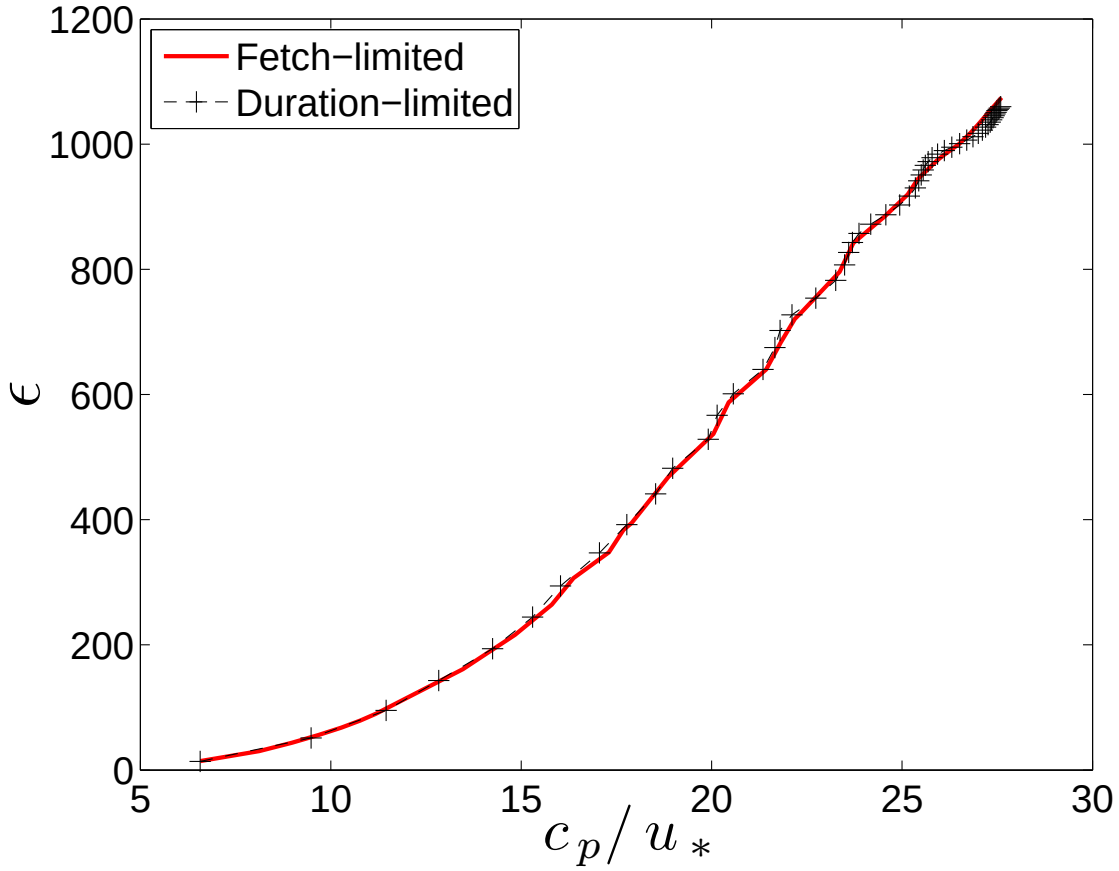

Figure II.2: Nondimensional energy ϵ versus wave age c_p/u_* using the wind input function by Snyder et al. (1981). The solid red line is a one-dimensional fetch-limited simulation and the black crosses correspond to a duration-limited run.

energy and peak frequency versus the nondimensional fetch from one-dimensional simulations carried out with S_{in}^{S} (blue line) and S_{in}^{Y} (red line). Both models do a good job reproducing the Kahma and Calkoen (1992) fetch relationships, matching the Pierson-Moskowitz limits at long fetches. The gray dashed lines indicate the location of the first grid point of each nested grid. Notice that in the transition between grids there small kinks in the model data, which is most noticeable in the energy, see for example ϵ at $\chi = 5 \times 10^5$. In order to ensure that the kinks due to nesting configuration have only minor effects on the overall development of spectrum, the one-dimensional fetch-limited simulations were validated against duration-limited runs using a single grid point without spatial propagation. In Figure II.2 two model runs using the same physics are compared, the red and black lines correspond to the one-dimensional nested simulation and a duration-limited limited run, respectively. The evolution of the nondimensional energy versus wave age is in excellent agreement between both models, suggesting that the one way nesting configuration does not have a significant effect on the evolution of the spectrum. This was further confirmed by comparing higher moments of the spectrum, such as one-dimensional spectra (omnidirectional and k_1 spectrum) and the directional spreading, over the entire evolution of the spectrum.

II.4.C Energy Partition

Based on field observations of the evolution of wind waves (Donelan et al., 1992) and a parameterization of the wind input from field and laboratory experiments (Donelan, 1987), Donelan (1998) suggests that the energy retained by the wave field is less than 5% of the total energy supplied by the wind, approaching 0% for fully developed seas. Figures II.3 and II.4 show the energy balance for the one-dimensional fetch-limited simulations. In both cases the total wind input $I = \int S_{in} d\mathbf{k}$ is greater or equal to the total dissipation $D = \int S_{ds} d\mathbf{k}$. The fraction of energy retained by the wave field P/I, where $P = \int DF/Dt d\mathbf{k}$, decreases with

Table II.2: One-way nested grid configuration for one-dimensional simulations. X_o corresponds to the initial location of each grid, Δx is the spatial resolution, Δt is time-step size for the spatial propagation and source term integration, N_x is the number of spatial grid points, N_t is total number of time-step integrations per grid, and CFL is the Courant-Friedrichs-Levy number. The spectral grid had a directional resolution of 4.5°between 0°and 360°and a constant bandwidth $d\omega/\omega$= 0.078, or dk/k= 0.156 according to the linear dispersion relationship, with a range of resolved frequencies between 0.443 and 141.4 rad s^{-1}(or between 0.020 and 0.6226 rad m^{-1}) having a total of 60 components in ω and 80 in direction.

Grid N.	X_o **(km)**	Δx **(km)**	Δt **(s)**	N_x	N_t	CFL
1	1.0	0.1	3	64	300	0.33
2	7.3	0.5	19	64	300	0.42
3	38.8	1.0	39	64	300	0.43
4	101.8	2.0	79	64	300	0.44
5	227.8	3.0	119	64	450	0.44
6	416.8	4.0	159	64	550	0.44

increasing wave age approaching zero for old seas. For both simulations P/I is as large as 20 to 25% for small wave ages, which is much greater that the suggested values by Donelan (1998).

II.5 Results

In this section we present a direct comparison between the ATM wind-wave observations of fetch-limited wavenumber spectra, collected during the Gulf of Tehuantepec Experiment (GOTEX), and two-dimensional simulations with good spectral resolution (for details see Table II.2). The two research flights (RF's) considered for this comparison are RF 05 and 10, when the environmental conditions were closest to idealized fetch-limited seas.

The two-dimensional simulations were carried out with a procedure similarly to the one used for the one-dimensional simulations from Section I.6 using a one-way nested configuration with high spatial resolution near shore, gradually decreasing with increasing fetch as shown in Table II.2. The model was initialized with a JONSWAP spectrum and Ewans (1998) bimodal directional distribution. The initial energy densities and peak frequencies were set homogenous longitudinally, varying only with latitude, approximately matching the ATM observations along the flight path. The model was run sequentially, starting with the grid closest to shore and progressing offshore. Within each grid, the model was run until reaching an approximate stationary solution. The data along the edge of the computational grid, at the lowest latitude, were saved to provide boundary conditions for the next run. The grid closest to shore had constant boundary conditions, corresponding to the initial conditions. One full simulation, over the 6 nested grids, took about two weeks running on parallel using MPI with 128 processors (1GHz each).

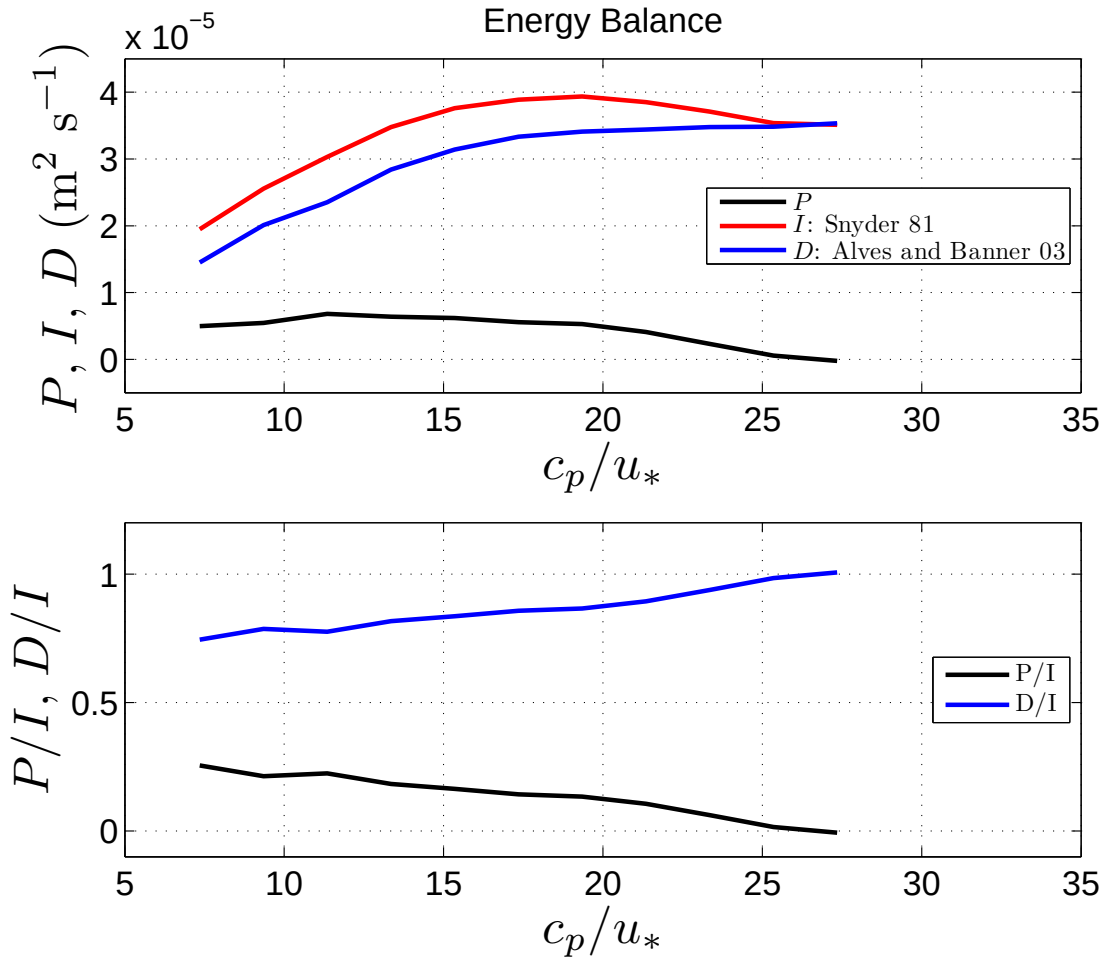

Figure II.3: Energy partition versus wave age (c_p/u_*) for the one-dimen- sional fetch-limited simulations. P, I and D are the total wave production, wind input, and dissipation, respectively. The model was forced with Snyder et al. (1981) wind input.

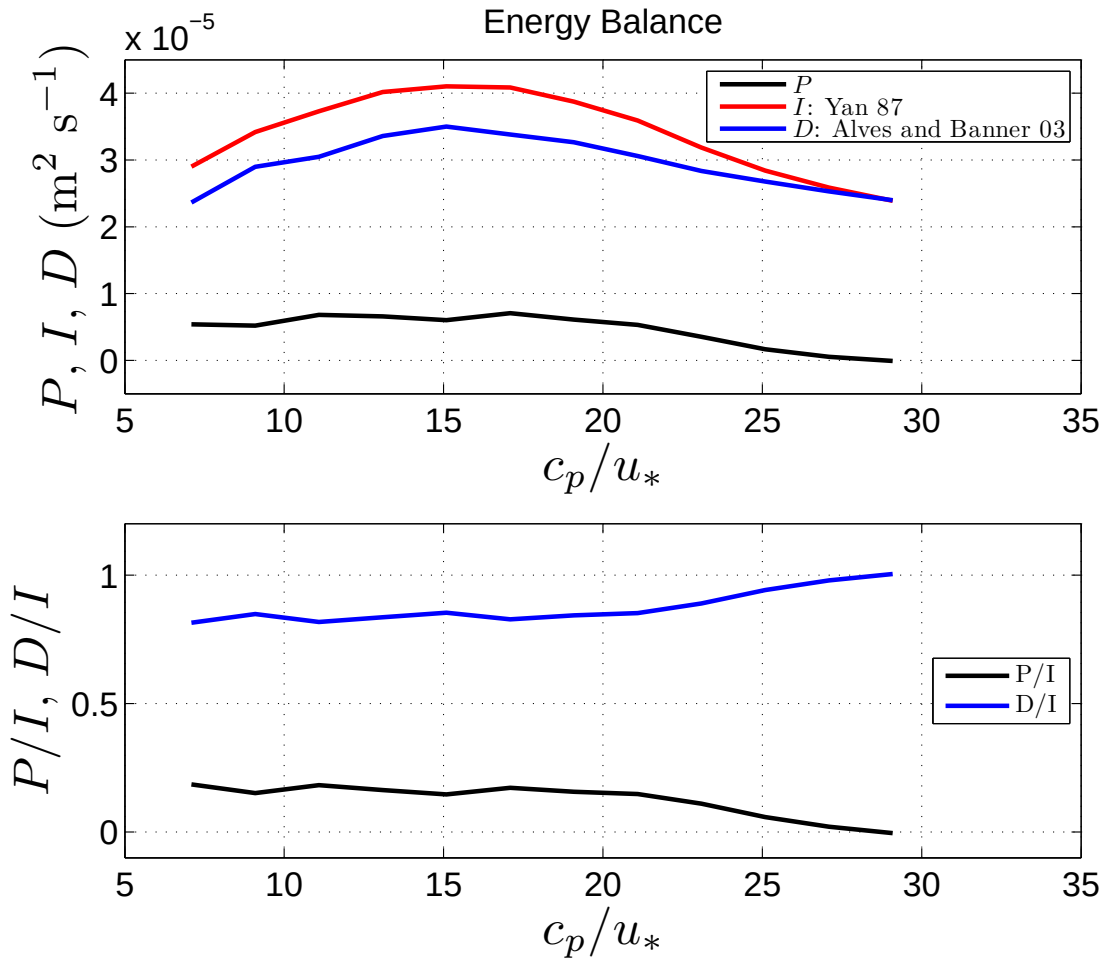

Figure II.4: Energy partition versus wave age (c_p/u_*) for the one-dimen- sional fetch-limited simulations. P, I and D are the total wave production, wind input, and dissipation, respectively. the model was forced with Yan (1987) wind input.

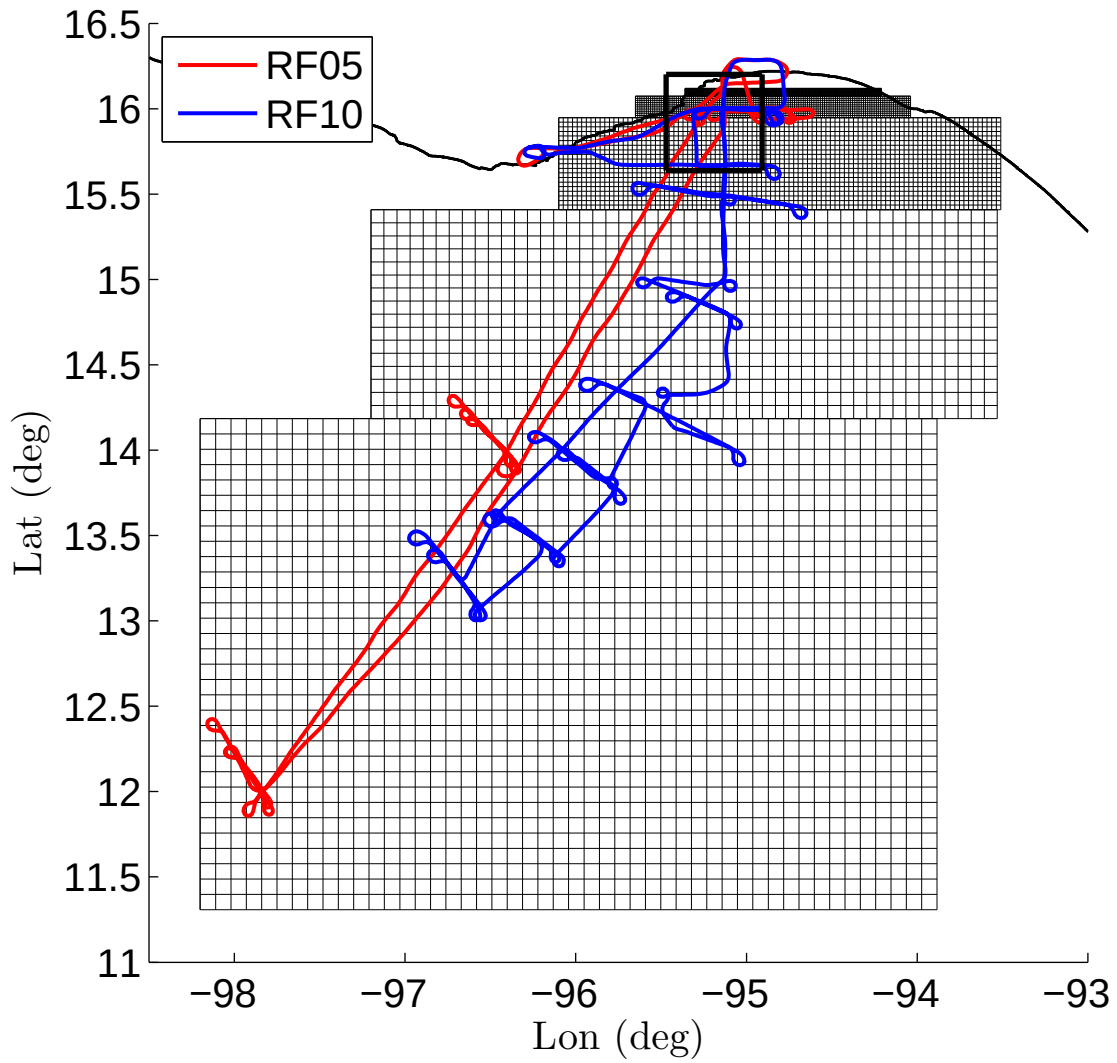

Figure II.5: Nested grid configuration for the two-dimensional simulations in the Gulf of Tehuantepec. The red and blue lines correspond to the flight tracks of RF 05 and 10, respectively. The area enclosed with thick black lines around 16°N is shown in Figure II.6.

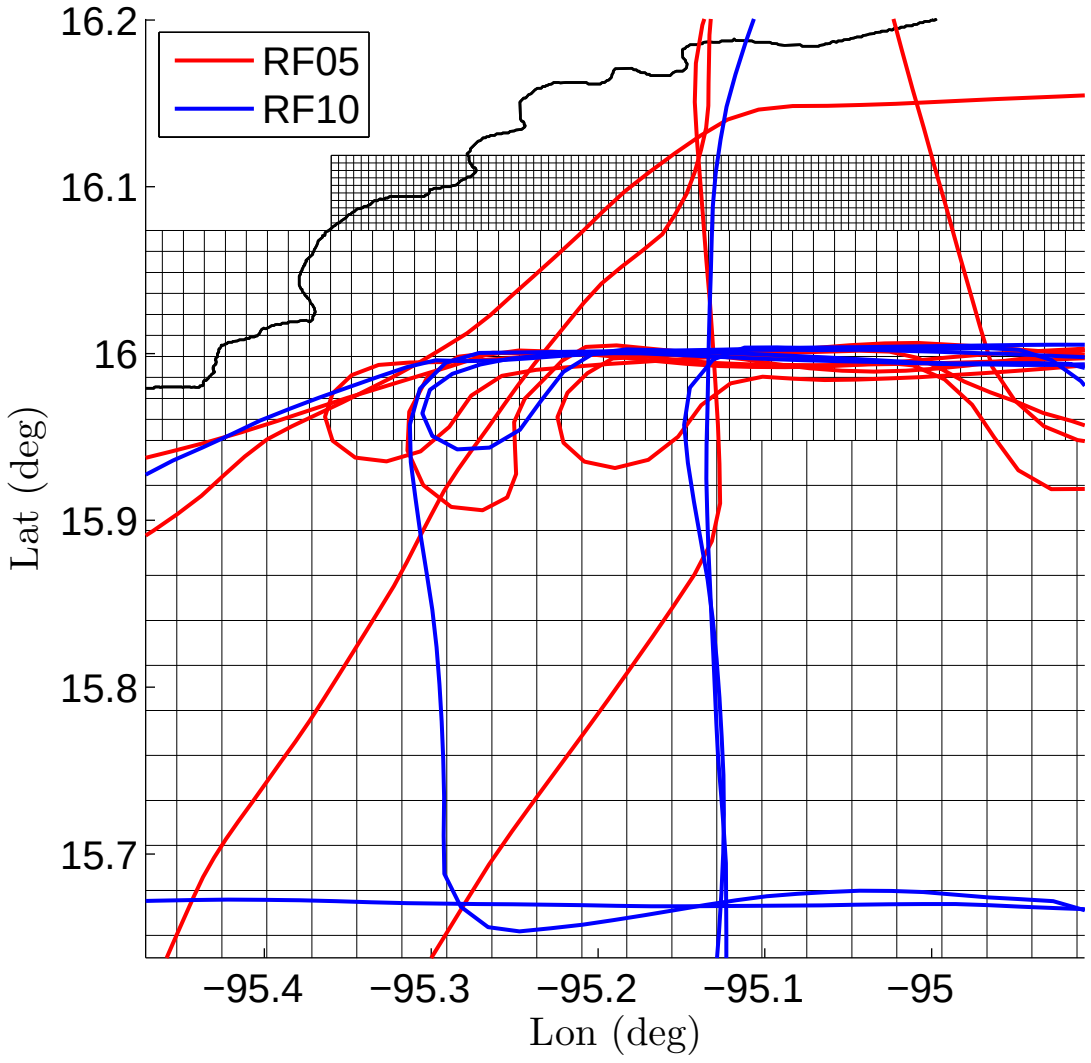

Figure II.6: Nested grid configuration for the two-dimensional simulations near the shore. Also see Figure II.5.

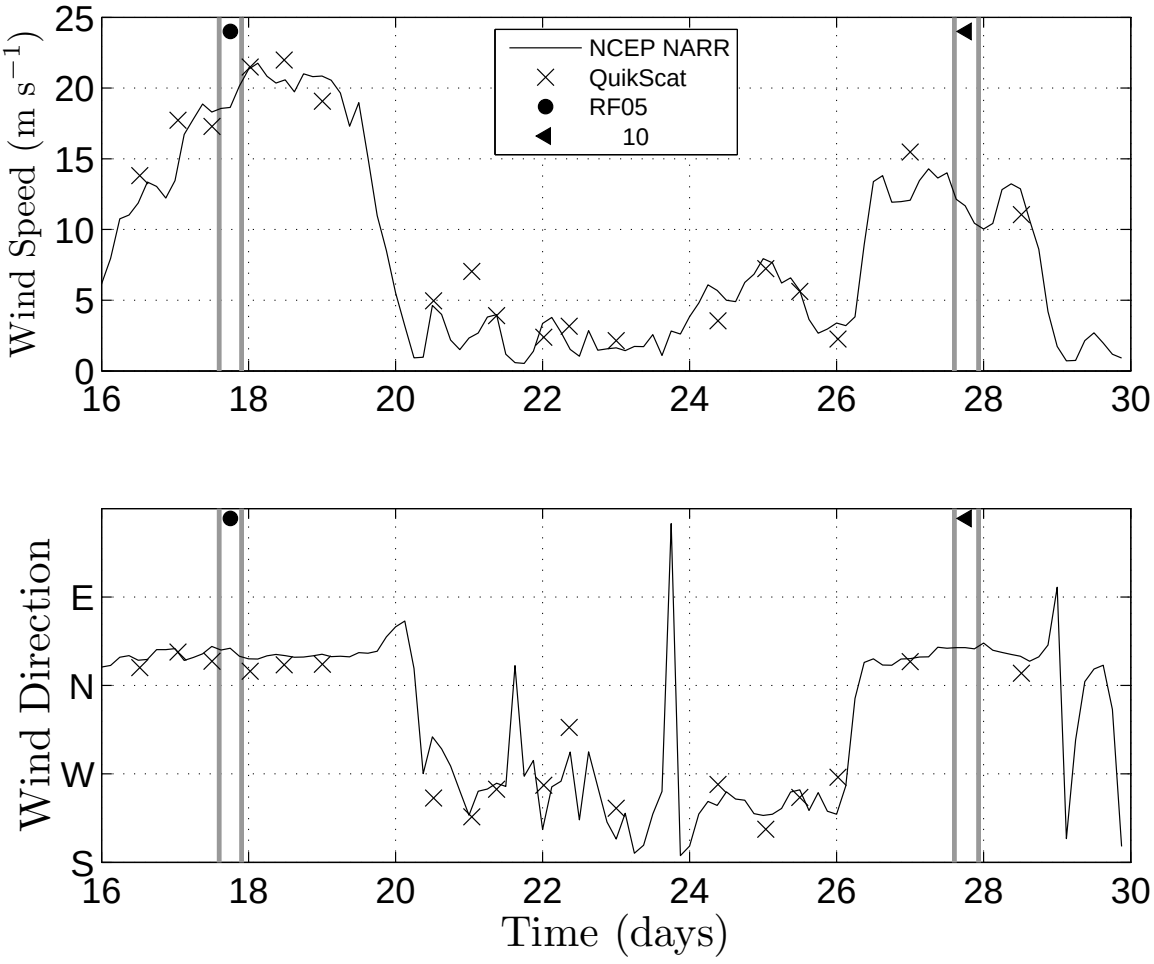

Figure II.7: Time history of the wind speed and direction at (15°N, 95W°) in the Gulf of Tehuantepec. The solid black line is corresponds to NCEP/NARR model wind data, and the crosses are the scatterometer winds. The durations of RF 05 and 10 are shown with solid gray lines.

Table II.3: One-way nested grid configuration for two-dimensional simulations over the Gulf of Tehuantepec. ($\mathbf{Lat}_o$,$\mathbf{Lon}_o$) correspond to the initial location of each grid, Δx and Δy correspond to the spatial resolution, Δt is time-step size for the spatial propagation and source term integration, N_x and N_y are the number of spatial grid points in each direction, N_t is total number of time-step integrations per grid, and CFL is the Courant-Friedrichs-Levy number. The spectral grid had a directional resolution of 4.5°between 0° and 360° and a constant bandwidth $d\omega/\omega$= 0.078, or dk/k= 0.156 according to the linear dispersion relationship, with a range of resolved frequencies between 0.263 and 14.066 rad s^{-1}(or between 0.007 and 20.188 rad m^{-1}) having a total of 54 components in ω and 80 in direction.

Grid N.	**Lat$_o$ (deg)**	**Lon $_o$ (deg)**	**Δx, Δy (km)**	**Δt (s)**	N_x	N_y	N_t	CFL
1	16.1188	-95.36	0.5	19	12	256	300	0.70
2	16.0693	-95.65	1.4	55	12	128	300	0.73
3	15.9308	-96.10	3.0	119	20	96	300	0.74
4	15.4182	-97.10	4.5	178	20	96	300	0.74
5	14.6493	-97.95	5.5	218	20	96	300	0.74
6	13.7095	-98.20	9.0	357	30	64	300	0.74

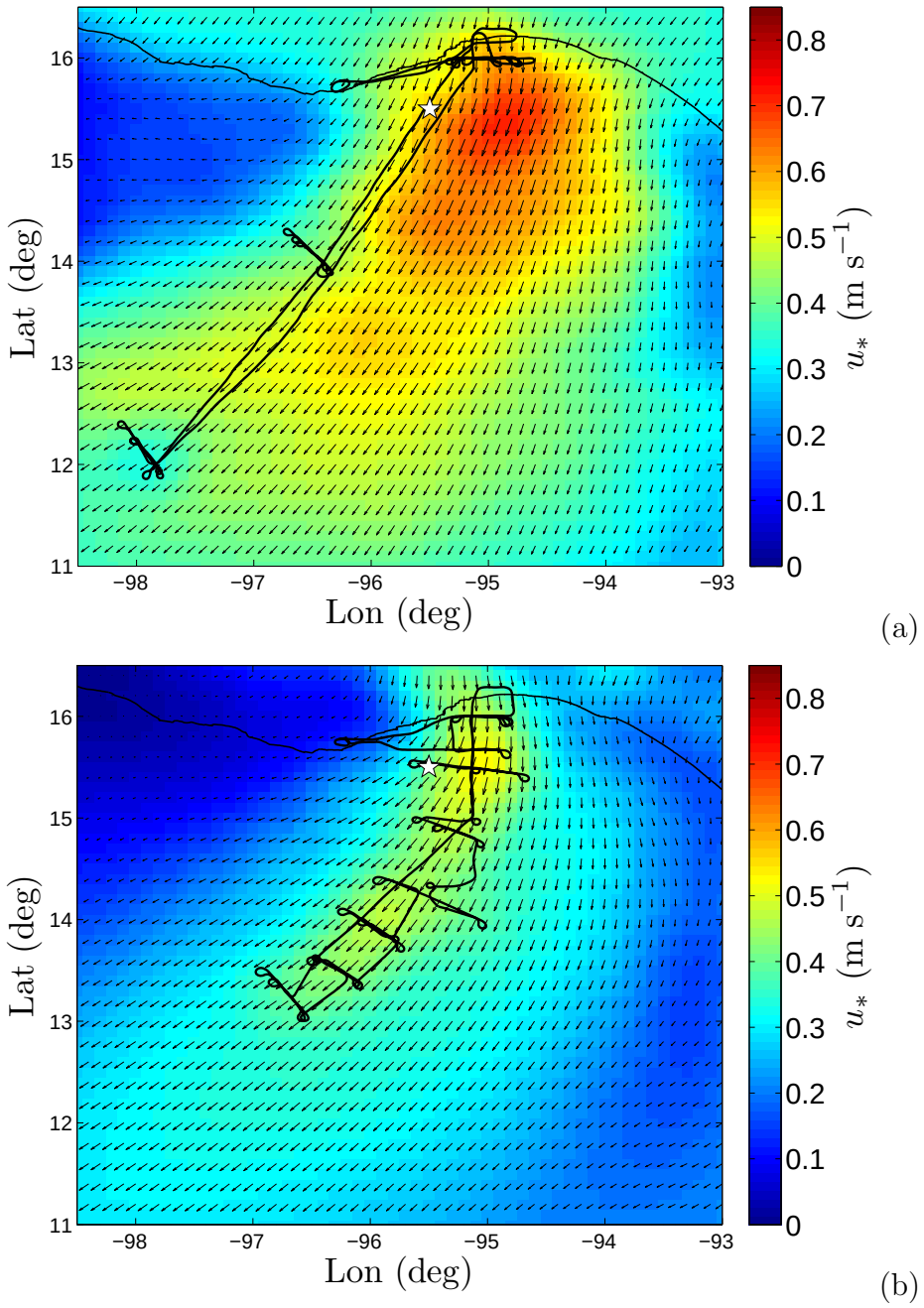

Figure II.8: Objective map of friction velocity (u_*) used as forcing for the two-dimensional simulations. (a) and (b) correspond to RF05 and RF10, respectively. The solid black lines indicate the flight paths. The white stars correspond to the location of the time series shown in Figure II.7.

II.5.A Winds

The two-dimensional simulations for RF 05 and 10 were forced with friction velocity fields calculated from an objective analysis (Bretherton et al., 1976) that combines the low level measurements, collected onboard the NSF/NCAR C-130 aircraft, and the available QuikScat scatterometer winds or model winds from the NCEP North American Regional Reanalysis (NARR). The measured friction velocities from low level flights were assumed to remain constant below the aircraft. As discussed by RM, the analysis of the GOTEX measurements reported by Friehe et al. (2006) showed stress divergence near the shore, which was in balance with the pressure gradient, however the scatter of the stress profiles was greater than the expected change due to extrapolation of the stress to the surface. NCEP/NARR winds have a relatively coarse resolution in space and time of 32 km and 3hrs, respectively. The QuikScat product used has a spatial resolution of 25 km and over the Gulf of Tehuantepec the satellite can have from zero to two passes per day. Following Perlin et al. (2004), the scatterometer neutral 10m winds velocities were inverted back to friction velocities using the drag coefficient by Large and Pond (1982), as were the NCEP/NARR 10m winds. The objective maps were calculated assuming an isotropic decorrelation length of 50 km, which is comparable to the downwind spatial resolution of the measured wind stress and is also reasonable given the coarseness of the scatterometer and model winds as well as the fact that the mountain gap, at the Tehuantepec Isthmus, is only 30 km wide. Each simulation was forced with the mapped friction velocity, assuming steady wind conditions. Figure II.7 shows the time history of the wind at (95W°,15°N), for geographical reference see Figure II.8.

For calculations of the objective map of friction velocities for RF05, there are two scatterometer QuikScat passes over the Gulf of Tehuantepec, one at 6 am and the other at 6 pm local time, corresponding to one hour prior to and 4 hours after the ATM data acquisition period. Both scatterometer passes were averaged

together, weighted towards 9 am local time, corresponding to the average time of the ATM data acquisition. The scatterometer data and the measured friction velocity from low altitude flights (at about 50m above the mean sea level) were used to produce a objective map (see Figure II.8a) which was used as input for the two-dimensional simulations.

For RF10, the QuikScat data available is limited to a single pass and misses most of the area of interest. However, the friction velocity measurements collected on board the NSF/NCAR C-130 aircraft had a good spatial coverage of the wind-jet. For the objective analysis, the measured friction velocity was combined with NCEP/NARR model data to produce an average wind map for the simulations. The NCEP/NARR model data were averaged between 4 am and 4 pm, local time, then converted to friction velocities using the drag coefficient by Large and Pond (1982), and were combined with the friction velocity measurements to estimate an objective map. During the mapping procedure, the friction velocity measurements were weighted more heavily, by a factor of 4, than the model winds. Figure II.8b shows the friction velocity map used in the two-dimensional simulations of RF10.

II.5.B Directional Spectra

Figure II.9 shows a sample comparison between various measured and simulated two-dimensional wavenumber spectra for RF05 using S_{in}^{S}, from short (24km) to very long fetches (473km). The simulated spectra are always narrower than the observations, particularly near the spectral peak. But nevertheless, the overall development of the spectrum with increasing fetch is similar between the measurements and the computations.

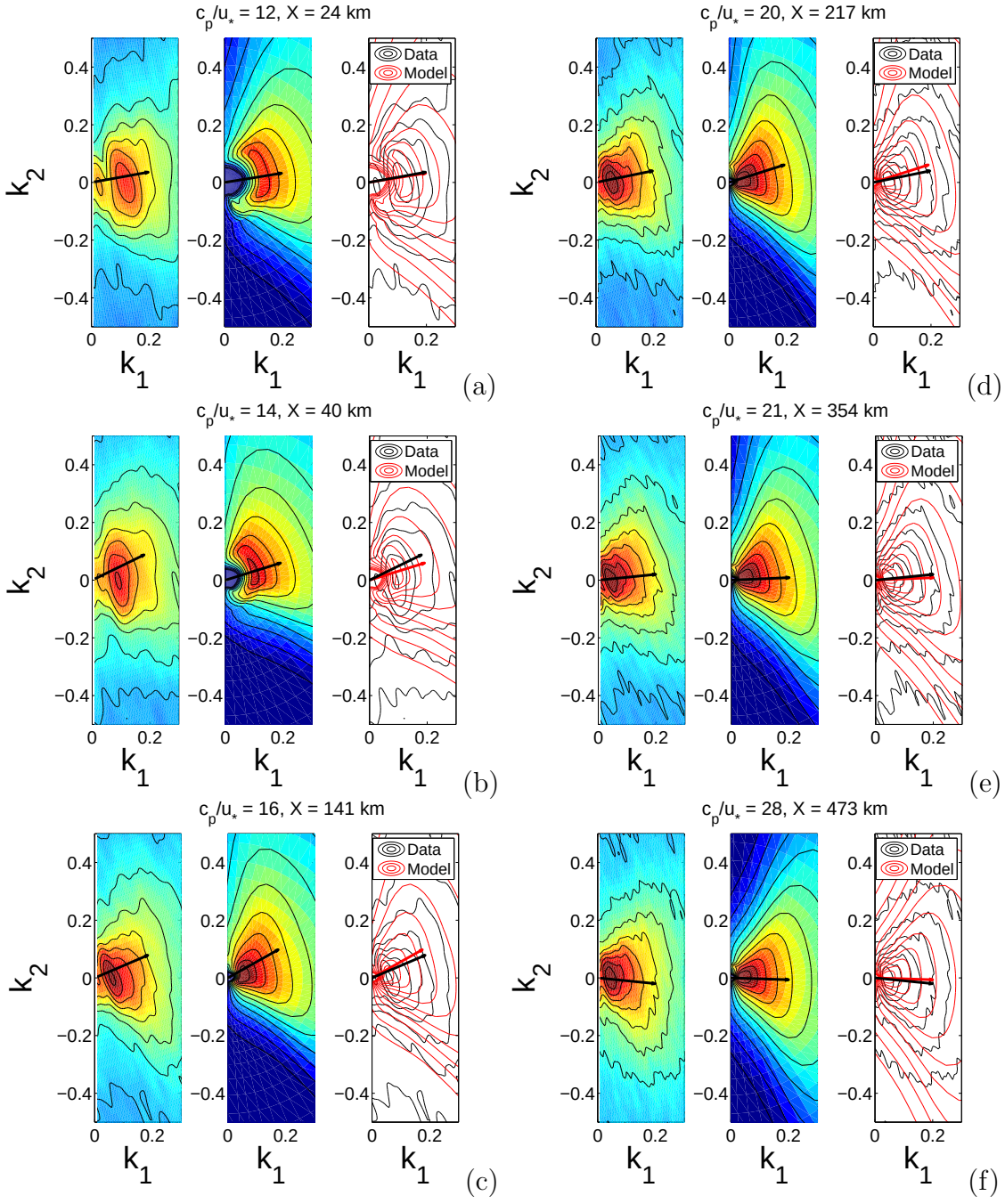

Figure II.9: Comparison of measured and simulated directional wave-number spectra in logarithmic scale for RF05. The corresponding fetches X are 24, 40, 141, 217, 354, and 473, respectively from (a-f). The black arrows indicate the local wind direction.

II.5.C Integral Parameters

In this section we present the standard nondimensional integral parameters, the energy density $\epsilon = \frac{\langle \eta^2 \rangle g^2}{u_{*e}^4}$ and peak frequency $\nu = \frac{f_p u_{*e}}{g}$, against the nondimensional effective fetch $\frac{X_e g}{u_{*e}}$, where the effective fetch X_e corresponds to the offshore displacement along the flight path projected along the dominant wave direction as described in RM. The measurements and simulations are compared in Figures II.10 and II.11 using the friction velocity from the measurements and objective map, respectively. The friction velocity from the objective map is more comprehensive and on average smaller than the instantaneous measurements. Figures II.10 and II.11 show the results from simulations forced with S_{in}^S, the results of the simulations using S_{in}^Y gave nearly identical results and therefore are omitted for clarity. Regardless of the scaling velocity used to nondimensionalize the data, the model and measurements are in reasonable agreement. The total energy of the model spectra is on average larger than the observations, this is expected because the measurements were collected under stable atmospheric stratification while the model was tuned against the composite growth rate by Kahma and Calkoen (1992), which is the average growth rate for waves generated under stable and unstable atmospheric stratifications. Tuning of the dissipation function by AB against the wave growth rate for stable atmospheric stratification was outside the scope of the present investigation due to time constraints. For reference, the one-dimensional simulation under constant winds is shown as solid gray line. At long fetches, regardless of the scaling velocity used, both the measured and modeled nondimensional peak frequency become lower than the expected limiting values at full development, suggesting that at such fetches the spectrum is locally overdeveloped due to the decreasing winds with increasing fetch, effectively becoming a young swell leaving the generation site.

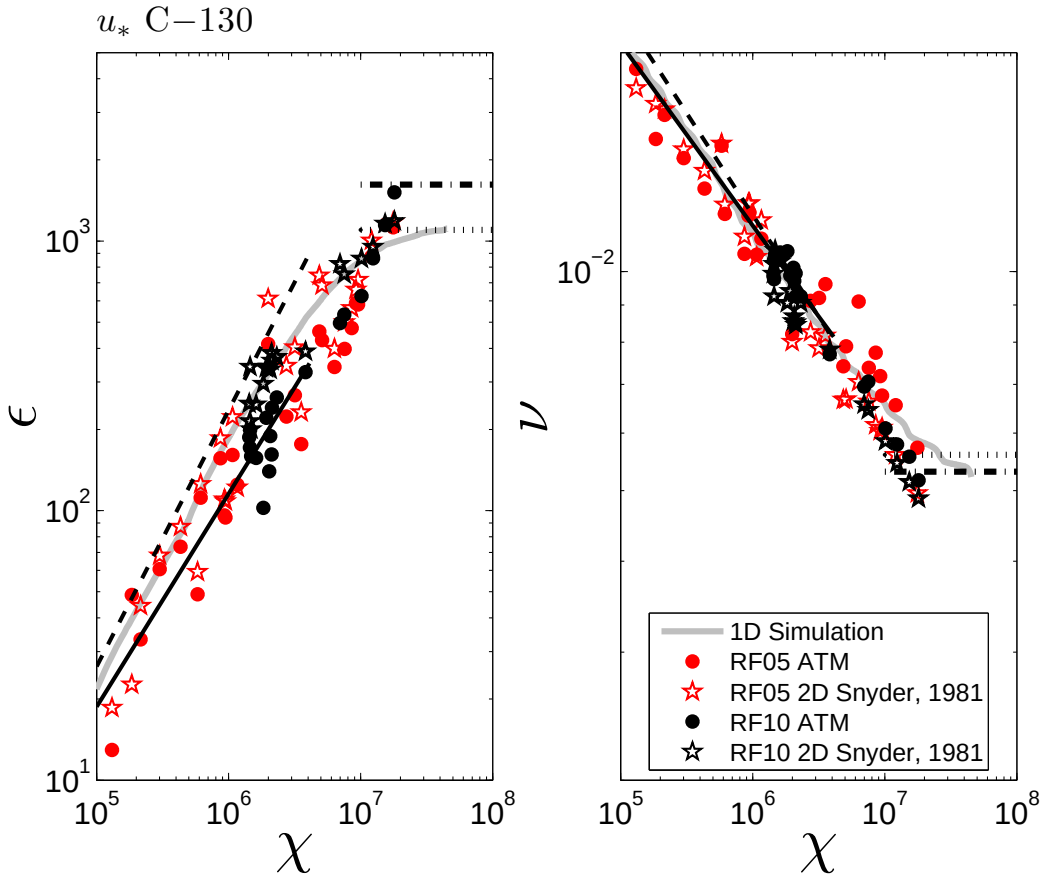

Figure II.10: Nondimensional energy and spectral peak frequency versus nondimensional fetch, scaled with the measured friction velocity. The red and black circles correspond to the ATM measurements for RF05 and RF10 , respectively. The red and black stars correspond to two-dimensional simulations for RF05 and RF10, respectively. The wind input function by Snyder et al. (1981) was used for the simulation. The solid gray line corresponds to the one-dimensional simulation with constant friction velocity. The solid and dashed black lines correspond to the reanalysis by Kahma and Calkoen (1992) for stable and unstable atmospheric stratification, respectively. The dotted and dashed-dotted correspond to the limits for a Pierson-Moskowitz spectrum (Komen et al., 1984) and those by Alves et al. (2003), respectively.

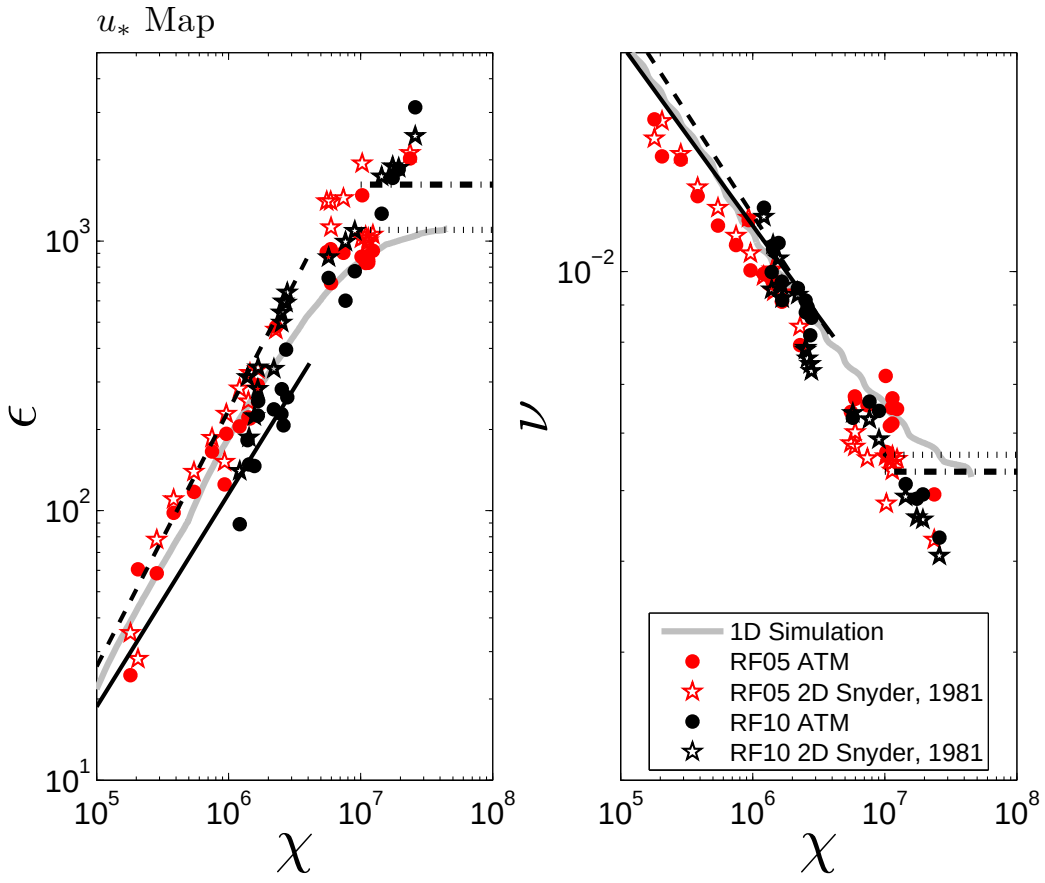

Figure II.11: Nondimensional energy and spectral peak frequency versus nondimensional fetch, scaled with the friction velocity from the objective map. The red and black circles correspond to the ATM measurements for RF05 and RF10 , respectively. The red and black stars correspond to two-dimensional simulations for RF05 and RF10, respectively. The wind input function by Snyder et al. (1981) was used for the simulation. The solid gray line corresponds to the one-dimensional simulation with constant friction velocity. The solid and dashed black lines correspond to the reanalysis by Kahma and Calkoen (1992) for stable and unstable atmospheric stratification, respectively. The dotted and dashed-dotted correspond to the limits for a Pierson-Moskowitz spectrum (Komen et al., 1984) and those by Alves et al. (2003), respectively.

II.5.D One-Dimensional Spectra

The one-dimensional spectra as given by:

$$\phi(k) = \int_{-\pi/2}^{\pi/2} F(k,\theta) k d\theta \tag{II.12}$$

and

$$\phi_1(k_1) = \int_{-0.5}^{0.5} F(k_1,k_2) dk_2, \tag{II.13}$$

where $\mathbf{k} = (k_1, k2) = (k, \theta)$ is the two-dimensional wavenumber in cartesian and polar coordinates, the unit vector $\hat{k}_1$ and $\theta = 0$ correspond to the dominant wave direction. The development $\phi(k)$ and $\phi_1(k_1)$ with increasing wave ages are shown in Figures II.12 and II.13, respectively. The left panels correspond to the ATM observations, the middle and right panels correspond to simulations using the wind input by Snyder et al. (1981) and Yan (1987), respectively. RF05 and RF10 are shown in the top and bottom panels, respectively. The energy density within the tail of the model spectra, for both ϕ and ϕ_1, is consistently larger than that of the observed spectra. This is consistent with the fact that the model spectra have larger net energy densities than the observations. Nevertheless, both the data and the models, except for the simulations with S_{in}^{Y} for old seas, show a power-law behavior where $\phi \sim k^{-5/2}$ and $\phi_1 \sim k^{-3}$. The spectral peakedness reduction with increasing fetch or wave age is a robust feature in both models and the observed spectra, for both ϕ and ϕ_1.

II.5.E Other Moments of the Spectrum

Banner and Young (1994) define the directional spreading using the first spectral moment over half of the spectrum. This can be generalized as:

$$\sigma_\theta(k) = \frac{\int_{-\pi/2}^{\pi/2} F(k,\theta)|\theta| d\theta}{\int_{-\pi/2}^{\pi/2} F(k,\theta) d\theta}, \tag{II.14}$$

where $\theta = 0$ corresponds to the dominant wave direction, providing a measure of the average half width of the spectrum. According to equation (II.14), the

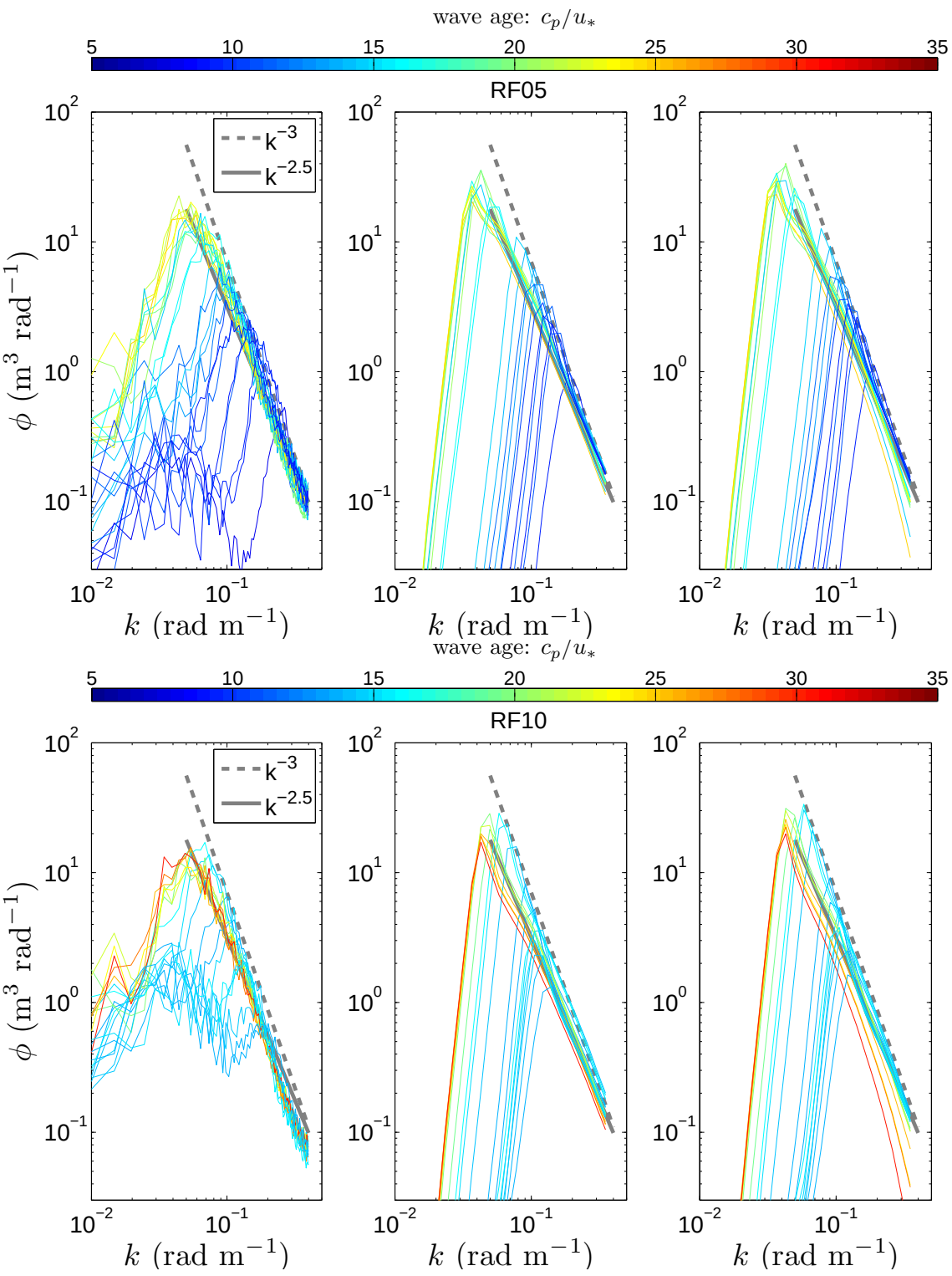

Figure II.12: Omnidirectional wavenumber spectra from ATM observations (left panel) and two-dimensional numerical simulations (middle and right panels) using Snyder et al. (1981) and Yan (1987) wind input functions, respectively.

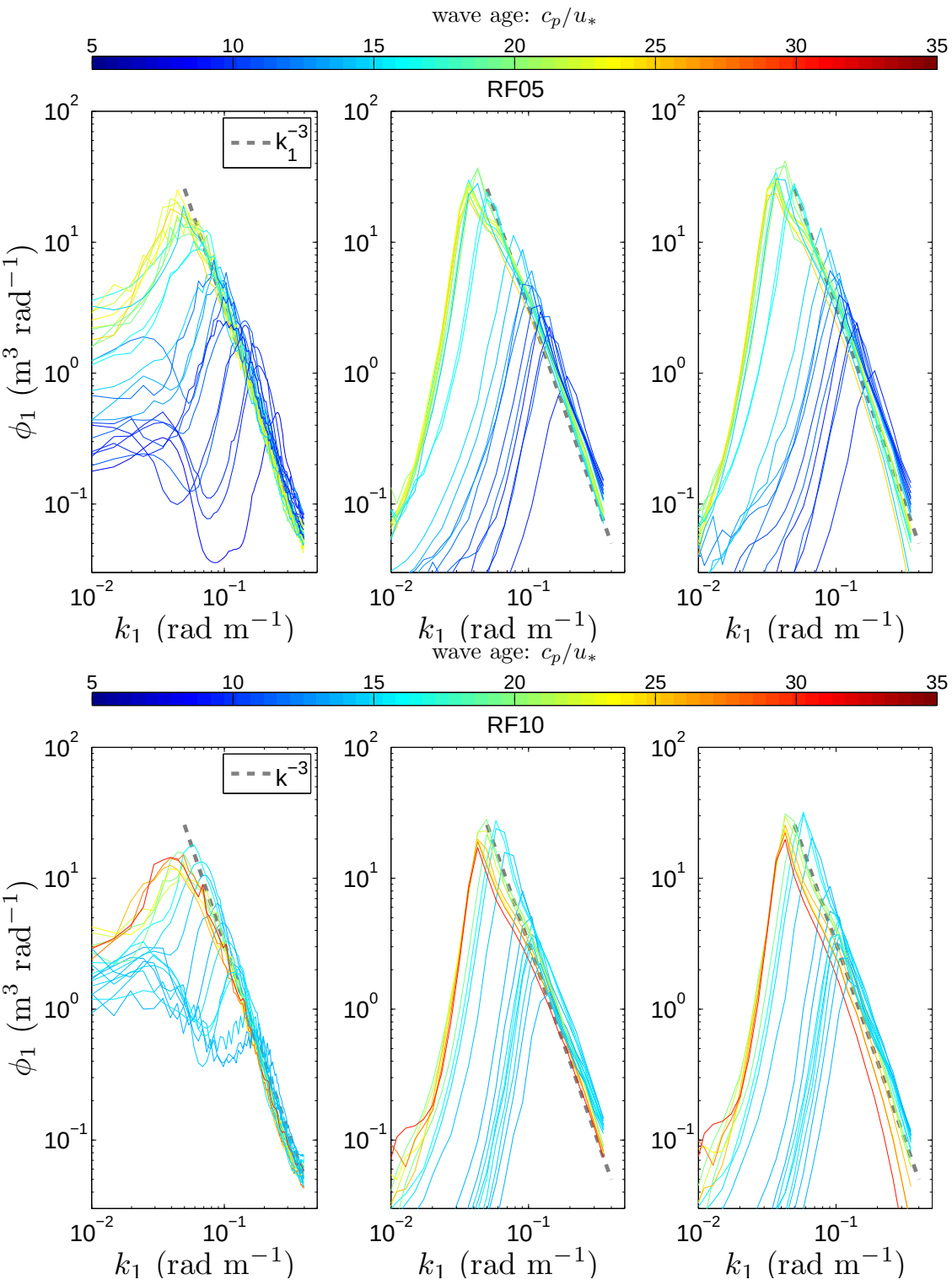

Figure II.13: One-dimensional k_1 spectra from ATM observations (left panel) and two-dimensional numerical simulations (middle and right panels) using Snyder et al. (1981) and Yan (1987) wind input functions, respectively.

spreading parameter for an isotropic spectrum becomes $\pi/4$. Figures II.14 and II.15 show the directional spreading for RF05 and RF10, respectively. The top panels correspond to the observations, the middle and bottom panels show the spreading from the computed spectra using S_{in}^{S} and S_{in}^{Y}, respectively. Both the measured and computed spectra are narrowest near the spectral peak, broadening towards both lower and higher frequencies. As expected from the comparisons of directional spectra shown in Figure II.9, the simulations are consistently narrower than the observations by about 10° to 15°. The model spectra forced with S_{in}^{Y} is narrower by about 5° than the model output using S_{in}^{S} for $k/k_p > 5$. The wiggles from the measured spectra are due to the discrete transformation of spectrum from cartesian to polar coordinates.

RM proposed an alternate metric to characterize the lateral spreading of the spectrum, the width of the spectrum in the direction orthogonal to the dominant wave direction as given by:

$$\mu_2(k_1) = \left(\frac{\int_{-0.5}^{0.5} F(k_1, k_2) k_2^2 dk_2}{\int_{-0.5}^{0.5} F(k_1, k_2) dk_2} \right)^{1/2}, \qquad \text{(II.15)}$$

where the limits of integration are in rad m^{-1} and are set according to the resolution of the observations as discussed in RM. Figure II.16 shows μ_2/k_p versus k_1/k_p for the observations (top panels) and the simulations using S_{in}^{S} and S_{in}^{Y} (middle and bottom panels,respectively). RF05 and RF10 correspond to the left and right panels, respectively. According to this alternate metric (μ_2), the model spectra is also consistently narrower than the observations. Nevertheless the model output shows a consistent trend, except for the spectra forced with S_{in}^{Y} for old seas, with little or no dependence on the wave age.

II.5.F The Bimodal Distribution

Direct comparisons of the measured and modeled normalized directional spectra $F(k,\theta)/F(k,0)$ for a constant k are shown in Figures II.17 and II.18. The

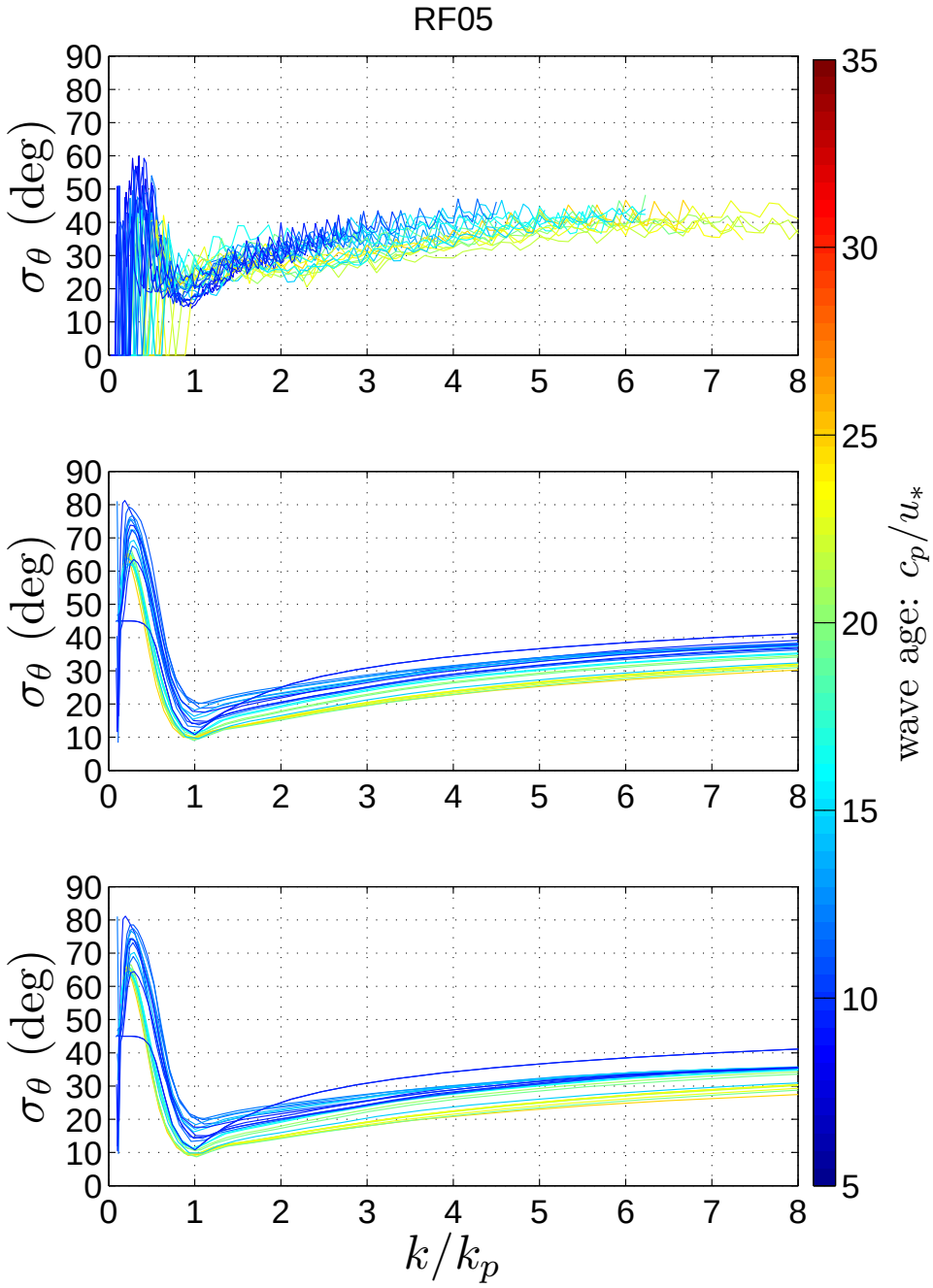

Figure II.14: Directional spreading (σ_θ) for RF05. The top panel corresponds to the observations, the middle and bottom panels are two-dimensional simulations using the wind input function by Snyder et al. (1981) and Yan (1987), respectively.

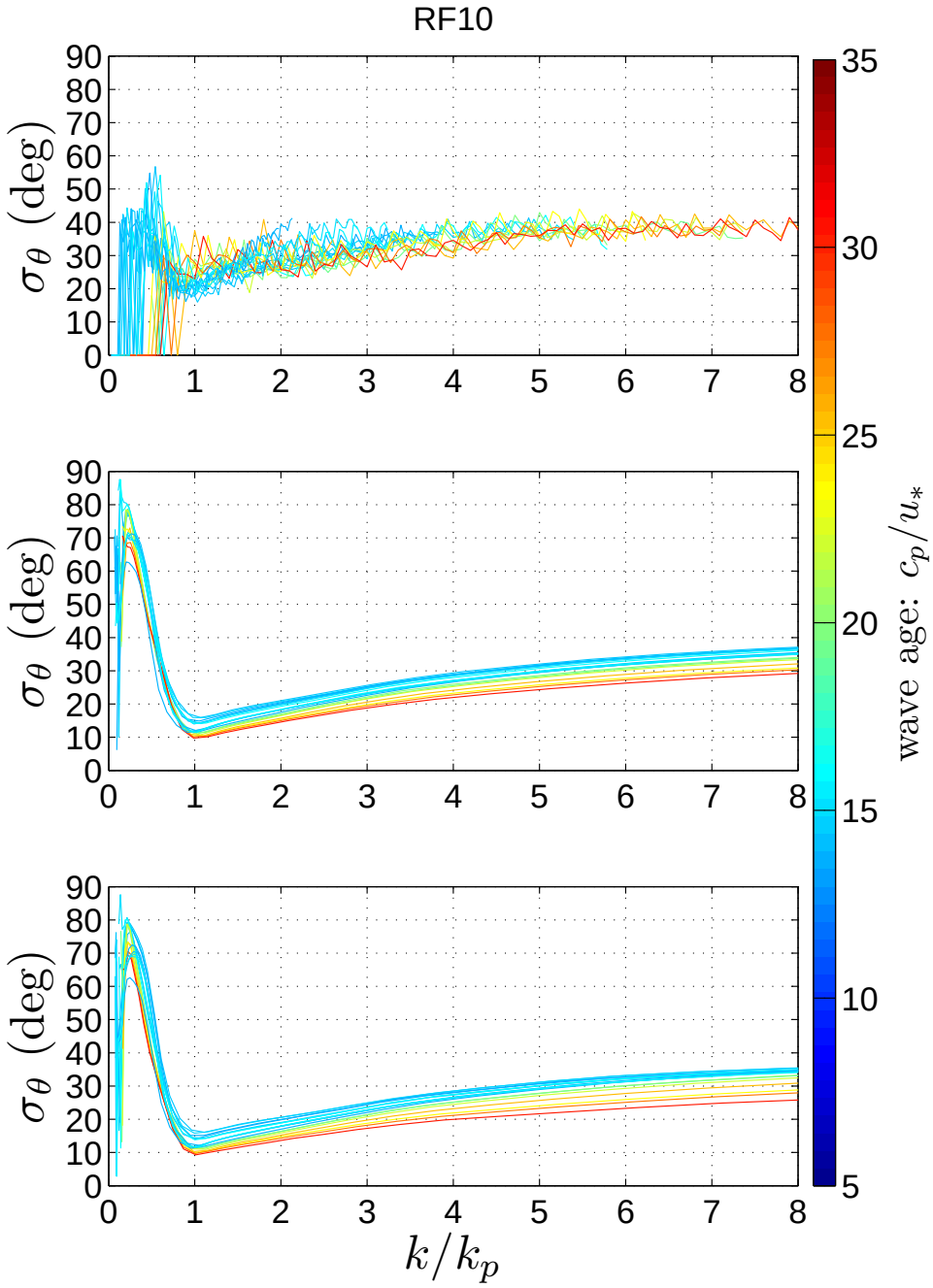

Figure II.15: Directional spreading (σ_θ) for RF10. The top panel corresponds to the observations, the middle and bottom panels are two-dimensional simulations using the wind input function by Snyder et al. (1981) and Yan (1987), respectively.

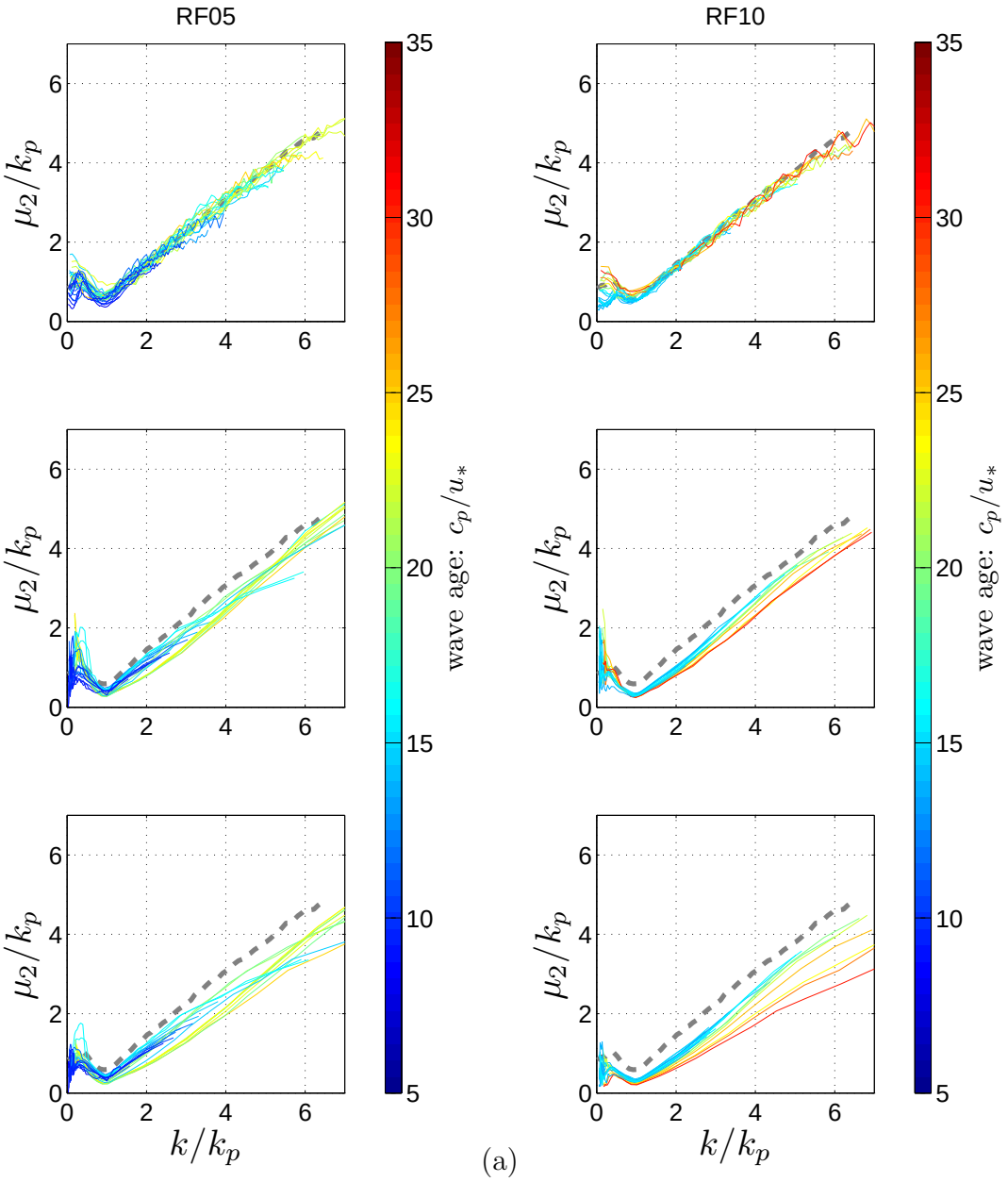

Figure II.16: Normalized spectral width in the direction orthogonal to the dominant waves (μ_2/k_p) versus k/k_p, for RF05 (a) and RF10 (b). The top panels correspond to the observations, the middle and bottom panels are from two-dimensional simulations using the wind input function by Snyder et al. (1981) and Yan (1987), respectively. The dashed gray line corresponds to the bin-average from the measured spectra for RF 05, 07, 09, and 10 (RM).

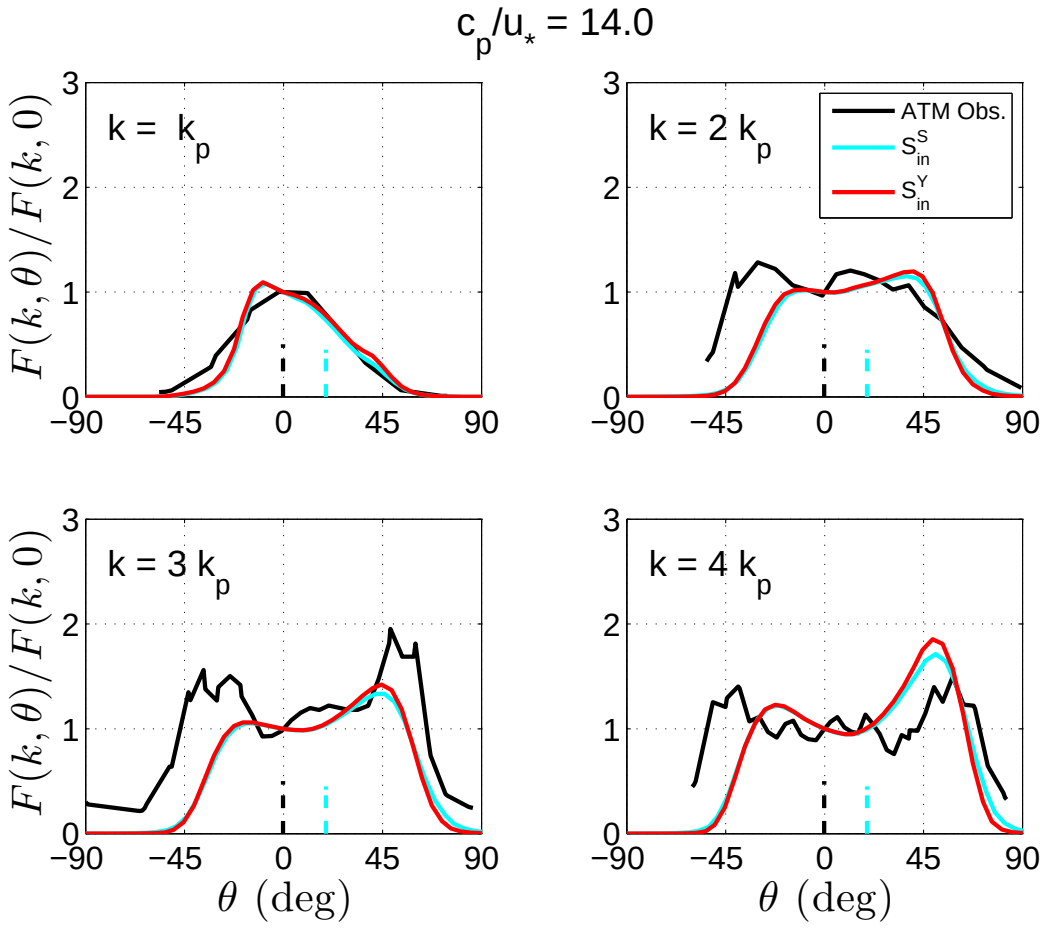

Figure II.17: Sample comparison between observed (solid black line) and simulated (solid cyan and red lines) normalized directional distribution of the spectrum, $F(k,\theta)/F(k,0)$, where $\theta = 0$ corresponds to the dominant wave direction. The local wave age $c_p/u_* = 14$. The directional distributions shown correspond to $k/k_p = 1$, 2, 3, and 4.

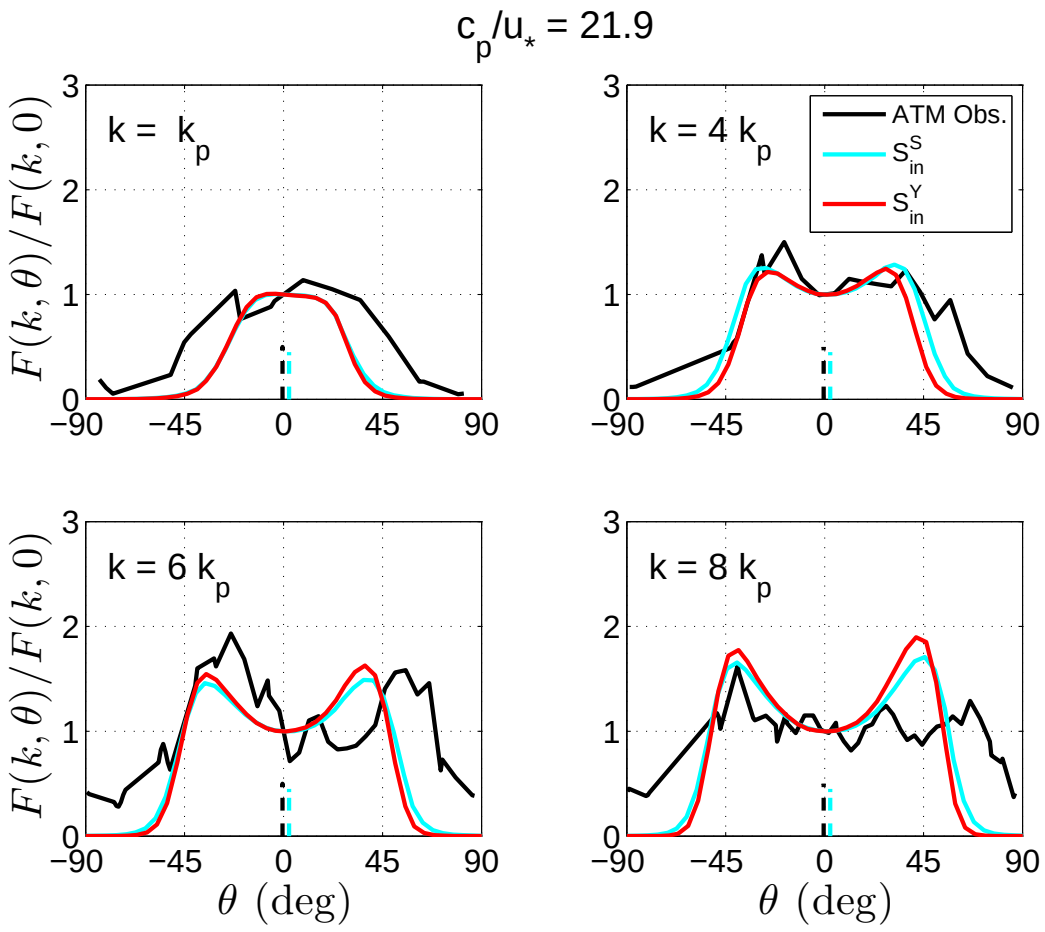

Figure II.18: Sample comparison between observed (solid black line) and simulated (solid cyan and red lines) normalized directional distribution of the spectrum, $F(k,\theta)/F(k,0)$, where $\theta = 0$ corresponds to the dominant wave direction. The local wave age $c_p/u_* = 21$. The distributions are shown for $k/k_p = 2$, 4, 6, and 8. The dashed vertical lines indicate the local wind direction.

directional wind-wave spectra at wavenumbers higher than the spectral peak, for both model and measured spectra, exhibit bimodal distributions, having extrema at a few degrees off the dominant wave direction. The lobe separation and amplitude are on average larger for the younger waves (a), for both simulated and measured spectra. Following Hwang et al. (2000b), the bimodal distribution can be characterized through the azimuthal lobe separation and relative amplitude as given by:

$$\theta_{lobe}(k) = \frac{\theta_1(k) + \theta_2(k)}{2} \tag{II.16}$$

$$r_{lobe}(k) = \frac{1}{2}\frac{F(k,\theta_1) + F(k,\theta_2)}{F(k,0)}, \tag{II.17}$$

where $\theta = 0$ corresponds to the dominant wave direction, $\theta_1(k)$ and $\theta_2(k)$ are the azimuthal locations of the maxima on each side of the spectrum. Figures II.19 and II.20 show θ_{lobe} and r_{lobe} for RF05 and RF10, respectively. The top panels correspond to the observations, the middle and bottom panels correspond to the computed spectra using S_{in}^S and S_{in}^Y, respectively. For both research flights, the separation and relative amplitude of the lobes for wavenumbers larger than the spectral peak are both larger in the observed spectra than the simulations. However, both simulated and measured spectra show a consistent trend where θ_{lobe} and r_{lobe} decrease with increasing wave age. RM showed a collapse in the trend in θ_{lobe} and r_{lobe} for the GOTEX measurements by scaling both parameters by $(c_p/u_*)^{1/2}$. Figure II.21 shows the scaled bimodal separation $\theta'_{lobe} = 0.2(c_p/u_*)^{1/2}\theta_{lobe}$ and the lobe amplitude $r'_{lobe} = 0.2(c_p/u_*)^{1/2}r_{lobe}$. Both θ'_{lobe} and r'_{lobe} collapse for both sets of computed spectra, but are consistently lower than the binned averages of the ATM observations reported by RM, which are shown which solid black lines.

II.6 Discussion and Conclusions

This study is concerned with the performance of the model by AB when compared to field observations of fetch-limited waves under realistic forcing in the

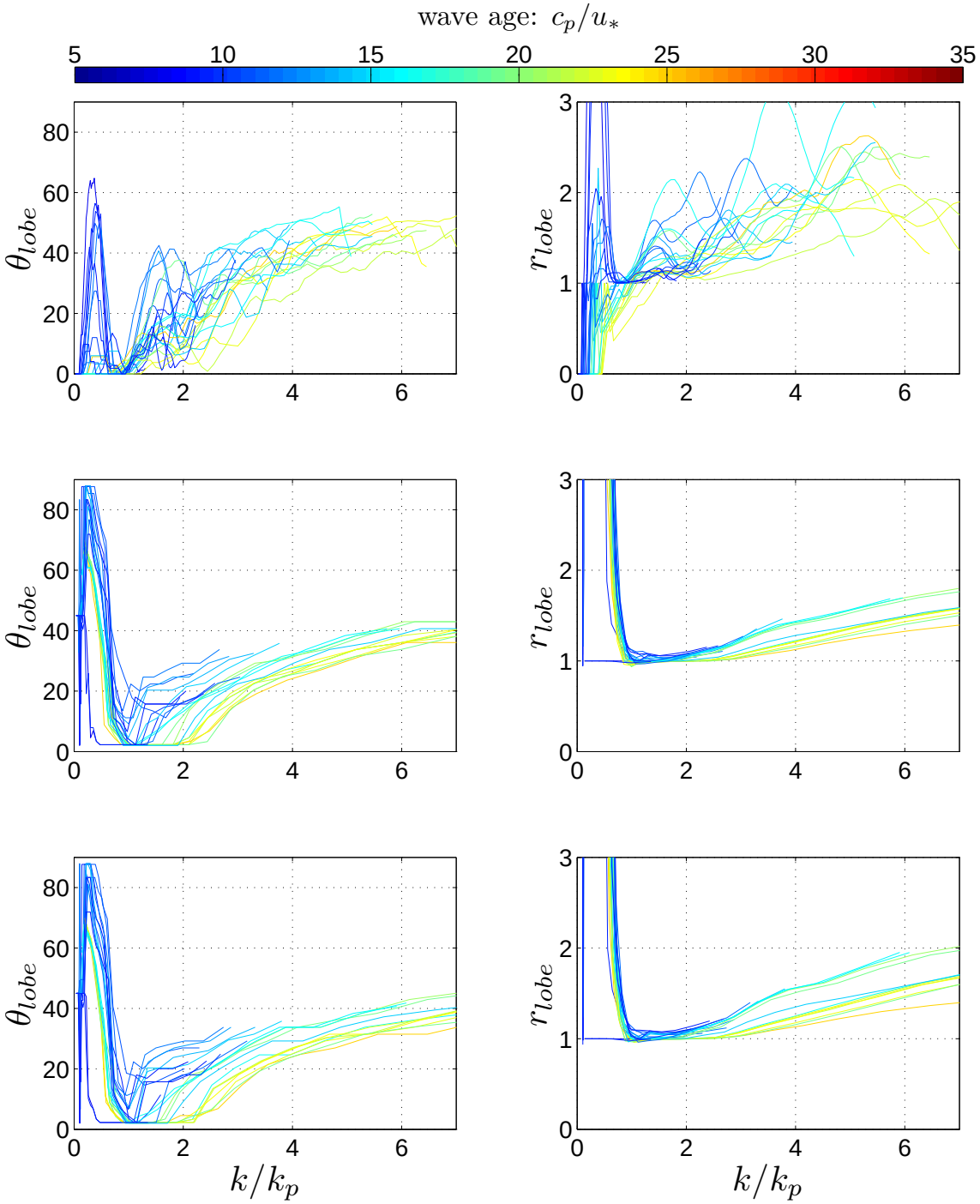

Figure II.19: Bimodal separation (θ_{lobe}) and relative amplitude (r_{lobe}) for RF05. The panels on the top correspond to measured spectra, the panels on middle and bottom panesl are two-dimensional simulations using as wind input the parameterization by Snyder et al. (1981) and Yan (1987), respectively.

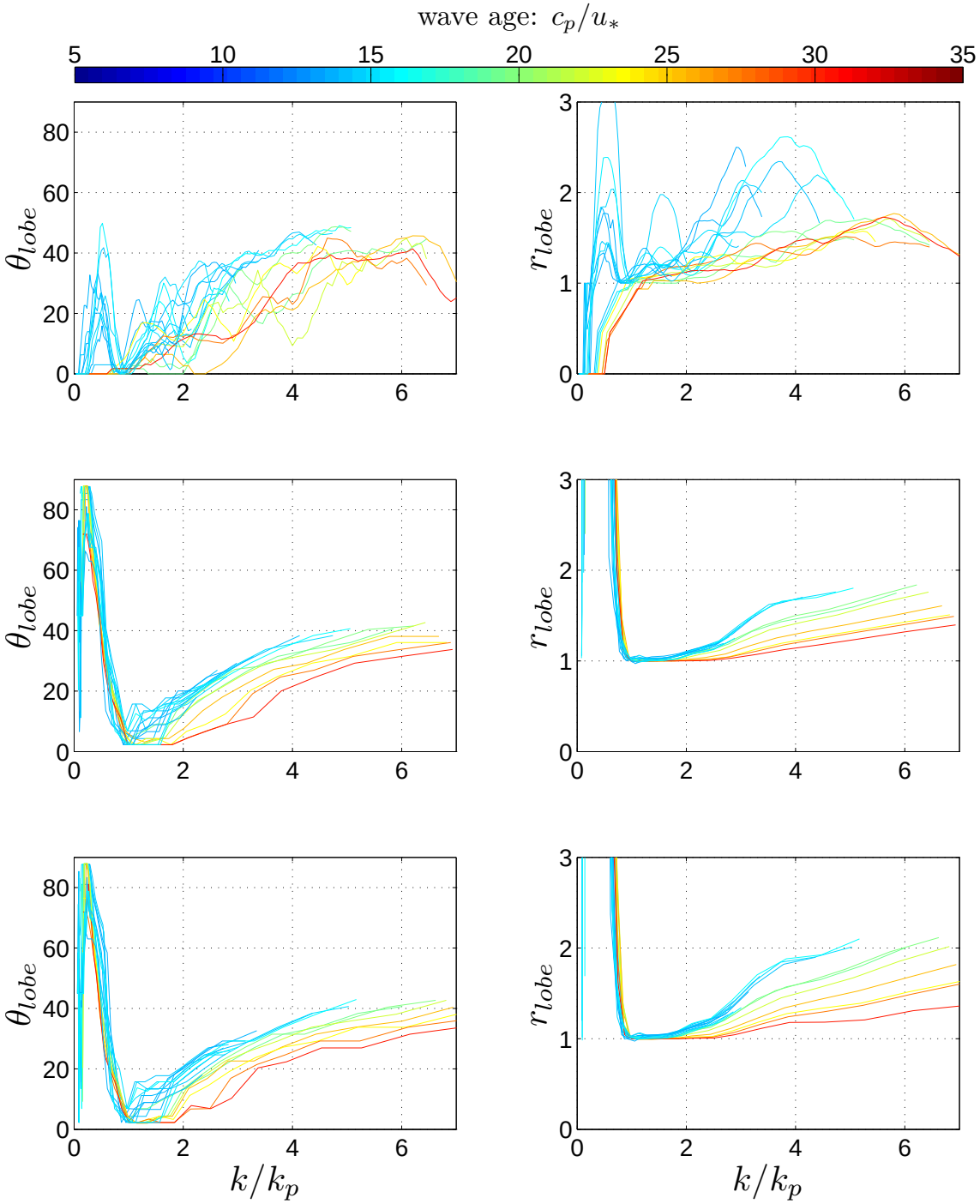

Figure II.20: Bimodal separation (θ_{lobe}) and relative amplitude (r_{lobe}) for RF10. The panels on the top correspond to measured spectra, the panels on middle and bottom panesl are two-dimensional simulations using the wind input parameterization by Snyder et al. (1981) and Yan (1987), respectively.

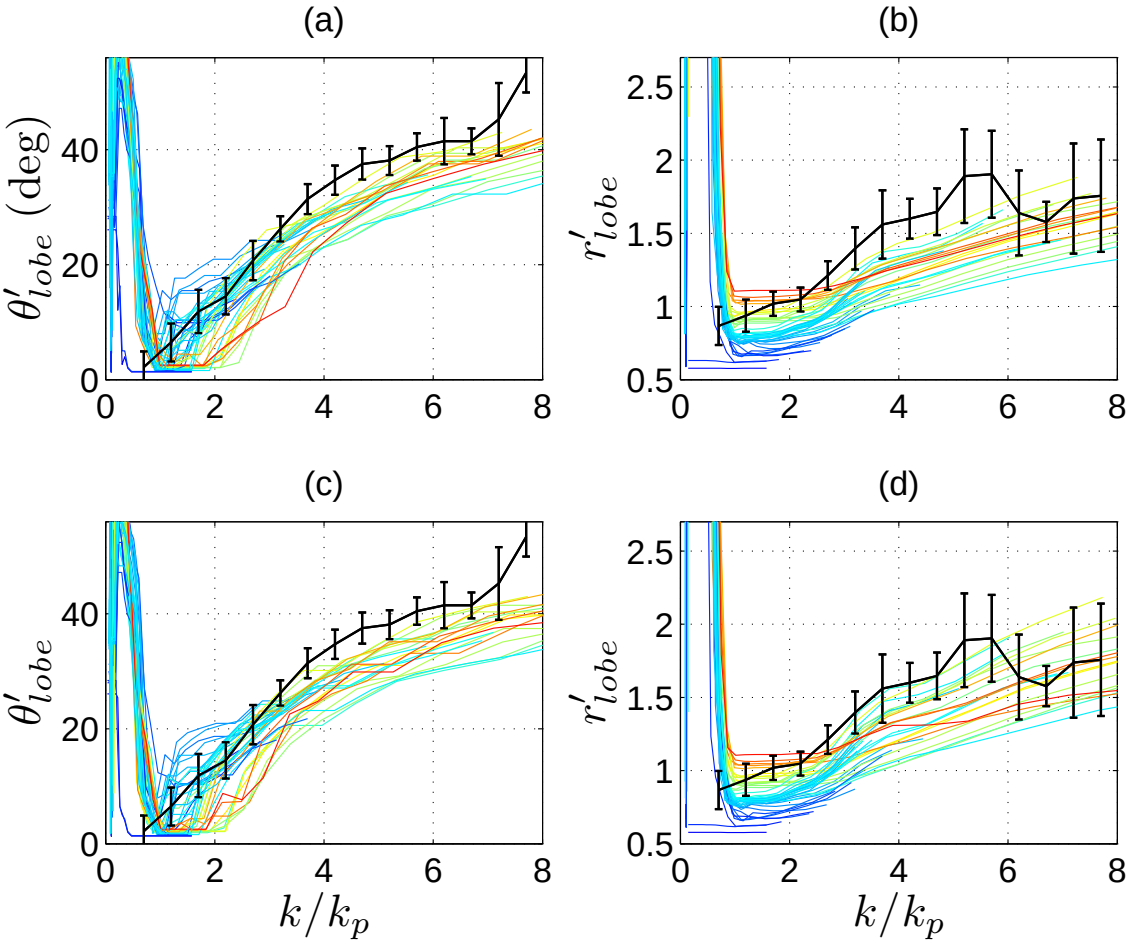

Figure II.21: Scaled bimodal separation (θ'_{lobe} =0.2 $\theta_{lobe}(c_p/u_{*_e})^{1/2}$) and relative lobe amplitude (r'_{lobe} =0.2 $r_{lobe}(c_p/u_{*_e})^{1/2}$) for RF05 and RF10 combined. Colored lines are from model runs with color scale as in Figure II.19. (a,b) and (c,d) correspond to simulations using the wind input parameterization by Snyder et al. (1981) and Yan (1987), respectively. The black lines correspond to the bin-average from measured ATM spectra for RF 05, 07, 09, and 10 (RM). The errorbars correspond to one standard deviation.

Gulf of Tehuantepec. This study used the wind-wave model WaveWatchIII as the numerical framework for the simulations. All model runs were carried out with exact computations of the nonlinear energy transfer due to wave-wave interactions as described by Tracy and Resio (1982) and VanVledder2006. The saturation-based dissipation function by AB was used in combination with the wind input by Snyder et al. (1981) or Yan (1987). The model was first implemented and tested in duration- and fetch-limited conditions. Then, the model was used for realistic two-dimensional simulations over the Gulf of Tehuantepec. The friction velocities used as input for the model were calculated from measurements at low altitudes (30 to 50 m above the mean sea level) and QuikScat scatterometer winds or NCEP/NARR model winds. The resulting two-dimensional average friction velocity maps show a two-dimensional wind-jet pattern which was assumed to be in steady state throughout the model computations.

The comparison between the observations and numerical simulations of wind-wave spectra is encouraging but not completely satisfactory. The numerical simulations with the wind input parameterization by Snyder et al. (1981) can maintaining power-law behaviors within the tail of the omnidirectional and k_1 spectrum, which are consistent with the observations. However, the dissipation by AB used with the wind input function by Yan (1987), can not balance the wind input at high wavenumbers, giving rise to a rapid decrease of the spectral energy, and therefore not maintaining a power-law behavior.

The simulated spectrum is always narrower than the measurements by about 10 degrees. This is consistent in all simulations regardless of the parameterization of the wind input used. The spectral width in the direction orthogonal to the dominant wave direction (μ_2) from computed spectra is always narrower than the field observations. This parameter also highlighted some of the problems at wavenumbers higher than the spectral peak associated with the simulations using the wind input by Yan (1987). At short to intermediate fetches, the data more or

less collapsed when scaled with k_p, but for older seas, the scaling no longer holds as the spectrum becomes much narrower.

An important result is the characterization of the bimodal distribution with increasing wave age. Although the measurements show wider lobe separations and larger lobe amplitudes when compared to the simulations, the scaling found in the measurements (RM), where θ_{lobe} and r_{lobe} collapse when scaled with $(c_p/u_*)^{1/2}$, was also found to apply for the computed spectra regardless of the wind input parametrization used.

The possible reasons for the discrepancies between the observations and the numerical simulations include the stationarity of the winds, wind gustiness, and uncertainties in the wind input and dissipation formulations, as well as higher order nonlinearities which are not accounted for in the computations.

References

Alves, J. H. G. M., and Banner, M. L., 2003: Performance of a saturation-based dissipation-rate source term in modeling the fetch-limited evolution of wind waves. *J. Phys. Oceanogr.*, **33**, 1274–1298.

Alves, J. H. G. M., Banner, M. L., and Young, I. R., 2003: Revisiting the Pierson-Moskowitz asymptotic limits for fully developed wind waves. *J. Phys. Oceanogr.*, **33**, 1301–1323.

Ardhuin, F., Herbers, T. H. C., Watts, K. P., Vledder, G. P. V., Jensen, R., and Graber, H., 2007: Swell and slanting fetch effects on wind wave growth. *J. Phys. Oceanogr.*, **37**(4), 908–931.

Badulin, S. I., Pushkarev, A. N., Resio, D., and Zakharov, V. E., 2005: Self-similarity of wind-driven seas. *Nonl. Proc. Geophys.*, **12**, 891–945.

Banner, M., 1990a: Equilibrium spectra of wind waves. *J. Phys. Oceanogr.*, **20**(7), 966–984.

Banner, M., Gemmrich, J., and Farmer, D., 2002: Multiscale measurements of ocean wave breaking probability. *J. Phys. Oceanogr.*, **32**, 3364–3375.

Banner, M., and Melville, W., 1976: On the separation of air flow over water waves. *J. Fluid Mech.*, **77**, 825–842.

Banner, M., and Morrison, R., 2006: On modeling spectral dissipation due to wave breaking for ocean wind waves. In *9th International Workshop on Wave Hindcasting and Forecasting*, 1–12. Environment Canada, the U.S. Army Engineer Research and Development Center's Coastal and Hydraulics Laboratory, and the WMO/IOC Joint Technical Commission for Oceanography and Marine Meteorology (JCOMM).

Banner, M. L., 1990b: The influence of wave breaking on the surface pressure distribution in wind-wave interactions. *J. Fluid Mech.*, **211**, 463–495.

Banner, M. L., Jones, I. S. F., and Trinder, J. C., 1989: Wavenumber spectra of short gravity waves. *J. Fluid Mech.*, **198**, 321–344.

Banner, M. L., and Young, I. R., 1994: Modeling spectral dissipation in the evolution of wind waves. part I: assessment of existing model performance. *J. Phys. Oceanogr.*, **24**, 1550–1570.

Barnett, T. P., and Wilkerson, J. C., 1967: On the generation of ocean wind waves as inferred from airborne radar measurements of fetch-limited spectra. *J. Mar. Res.*, **25**(3), 292–328.

Bates, D., and Watts, D., 1988: *Nonlinear regression analysis and its applications.* John Wiley and Sons, Inc.

Battjes, J. A., Zitman, T. J., and Holthuijsen, L. H., 1987: A reanalysis of the spectra observed in JONSWAP. *J. Phys. Oceanogr.*, **17**, 1288–1295.

Benoit, M., 1992: Practical comparative performance survey of methods used for estimating directional wave spectra form heavepitch roll data. *Proc. 23rd Int. Conf. on Coastal Engineering, Vol. 2, Venice, Italy, ASCE*, 162–175.

Bretherton, F. P., Davis, R. E., and Fandry, C. B., 1976: A technique for the objective analysis and design of oceanographic experiments applied to mode-73*. *Deep Sea Res.*, **23**, 559–582.

Bretschneider, C., 1952: The generation and decay of wind waves in deep water. *Trans. Am. Geophys. Union*, **33**(3), 381–389.

Brown, E. N., Friehe, C. A., and Lenschow, D. H., 1983: The use of pressure fluctuations on the nose of an aircraft for measuring air motion. *J. Climate and Appl. Met.*, **22**, 171–180.

Burgers, G., and Makin, V. K., 1993: Boundary-layer model results for wind-sea growth. *J. Phys. Oceanogr.*, **23**, 372–385.

Chalikov, D., 1986: Numerical simulation of the boundary layer above waves. *J. Fluid Mech.*, **34**, 63–98.

Chalikov, D. V., and Belevich, M. Y., 1993: One-dimensional theory of the wave boundary layer. *Boundary-Layer Meteorol.*, **63**, 65–96.

Cote, L. J., Davis, J. O., Marks, W., McGough, R. J., Mehr, E., Pierson, W. J., Jr., Ropek, J. F., Stephenson, G., and Vetter, R. C., 1960: The directional spectrum of a wind generated sea as determined from data obtained by the Stereo Wave Observation Project. Technical Report 6, N. Y. U. Coll. of Eng.

Cox, C., and Munk, W., 1954: Statistics of the sea surface derived from sun gliter. *J. Mar. Res.*, **13**, 198–227.

Dobson, F., Perrie, W., and Toulany, B., 1989: On the deep water fetch laws for wind-generated surface gravity waves. *Atmosphere Ocean*, **27**, 210–236.

Donelan, M., 1982: The dependence of aerodynamic drag coefficient on wave parameters. In *Proc. First Int. conf on Meteor. and Air-sea Interaction of the Coastal Zone*, p. 381. The Hague, American Meteorological Society.

Donelan, M., 1990: *The Sea*, volume 9 of *Ocean Engineering Science*, chapter Air-Sea Interaction, 239–292. Wiley and Sons.

Donelan, M., Skafel, M., Graber, H., Liu, P., Schwab, D., and Venkatesh, S., 1992: On the growth rate of wind-generated waves. *Atmosphere-Ocean*, **30**, 457–478.

Donelan, M. A., 1987: The effect of swell on the growth of wind waves. *Johns Hopkins APL Tech. Digest*, **8**, 18–23.

Donelan, M. A., 1998: Air-water exchange processes. In *Physical Processes in Lakes and Oceans*, editor J. Imberger, pages 18–36. American Geophysical Union, Washington, D.C. ISBN 0-87590-268-5.

Donelan, M. A., Hamilton, J., and Hui, W. H., 1985: Directional spectra of wind-generated waves. *Philosophical Transactions of the Royal Society of London. Series A, Mathematical and Physical Sciences*, **315**(1534), 509–562.

Dysthe, K. B., Trulsen, K., Krogstad, H., and Socquet-Juglard, H., 2003: Evolution of a narrow-band spectrum of random surface gravity waves. *J. Fluid Mech.*, **478**, 1–10.

Ewans, K. C., 1998: Observations of the directional spectrum of fetchlimited waves. *J. Phys. Oceanogr.*, **28**, 495–512.

Forristall, G., 1981: Measurements of a saturated range in ocean wave spectra. *J. Geophys. Res.*, **86**, 8075–8084.

Friehe, C. A., Khelif, D., and Melville, W. K., 2006: Aircraft air-sea flux measurements in the Gulf of Tehuantepec. *Paper presented at the 14th Conference on Interaction of the Sea and Atmosphere, AMS Annual Meeting, 29 January-2 February 2006, Atlanta, GA*.

Grachev, A. A., and Fairall, C. W., 2001: Upward momentum transfer in the marine boundary layer. *J. Phys. Oceanogr.*, **31**, 1698–1711.

Hara, T., and Belcher, S., 2002: Wind forcing in the equilibrium range of wind-wave spectra. *J. Fluid Mech.*, **470**, 223–245.

Hasselmann, D., Dunckel, M., and Ewing, J. A., 1980: Directional wave spectra observed during JONSWAP 1973. *J. Phys. Oceanogr.*, **10**, 1264–1280.

Hasselmann, K., 1962: On the nonlinear energy transfer in a gravity-wave spectrum, part 1: General theory. *J. Fluid Mech.*, **12**, 481–500.

Hasselmann, K., 1963: On the non-linear energy transfer in a gravity wave spectrum Part 2: conservation theorems; wave-particle analogy; irreversibility. *J. Fluid Mech.*, **15**, 273–282.

Hasselmann, K., 1974: On the spectral dissipation of ocean waves due to white capping. *Boundary-Layer Meteorol.*, **6**, 107–127.

Hasselmann, K., Barnett, T. P., Bouws, E., Carlson, H., Cartwright, D. E., Enke, K., Ewing, J. A., Gienapp, H., Hasselmann, D. E., Kruseman, P., Meerburg, A., Müller, P., Olbers, D. J., Richter, K., Sell, W., and Walden, H., 1973: Measurements of wind-wave growth and swell decay during the joint north sea wave project (JONSWAP). *Dtsch. Hydrogr. Z. Suppl. A*, **8**(12), 95pp.

Holthuijsen, L. H., 1983: Observations of the directional distribution of ocean wave energy. *J. Phys. Oceanogr.*, **13**, 191–207.

Hwang, P., Wang, D., Walsh, E., Krabill, W., and Swift, R., 2000a: Airborne measurements of the wavenumber spectra of ocean surface waves, part I: Spectral slope and dimensionless spectral coefficient. *J. Phys. Oceanogr.*, **30**(11), 2753–2767.

Hwang, P., Wang, D., Walsh, E., Krabill, W., and Swift, R., 2000b: Airborne measurements of the wavenumber spectra of ocean surface waves, part II: Directional distribution. *J. Phys. Oceanogr.*, **30**(11), 2768–2787.

Hwang, P. A., and Wang, D. W., 2001: Directional distributions and mean square slopes in the equilibrium and saturation ranges of the wave spectrum. *J. Phys. Oceanogr.*, **31**, 1346–1360.

Jackson, F. C., Walton, W. T., and Baker, P. L., 1985a: Aircraft and satellite measurement of ocean wave directional spectra using scanning-beam microwave radars. *J. Geophys. Res.*, **90**, 987–1004.

Jackson, F. C., Walton, W. T., and Peng, C. Y., 1985b: A comparison of in situ and airborne radar observations of ocean wave directionality. *J. Geophys. Res.*, **90**, 1005–1017.

Janssen, P., 2003: Nonlinear four-wave interactions and freak waves. *J. Phys. Oceanogr.*, **33**, 863–884.

Janssen, P., Komen, G., and de Voogt, W., 1987: Friction velocity scaling in wind wave generation. *Boundary-Layer Meteorol.*, **38**, 29–35.

Janssen, P. A. E. M., 1989: Wave-induced stress and the drag of air flow over sea waves. *J. Phys. Oceanogr.*, **19**, 745–754.

Janssen, P. A. E. M., 1991: Quasi-linear theory of of wind wave generation applied to wave forecasting. *J. Phys. Oceanogr.*, **21**, 1631–1642.

Jones, I. S. F., and Toba, Y., 2001: *Wind Stress over the Ocean*. Wind Stress over the Ocean, Edited by Ian S. F. Jones and Yoshiaki Toba, pp. 326. ISBN 0521662435. Cambridge, UK: Cambridge University Press, September 2001.

Kahma, K., 1981: A study of the growth of the wave spectrum with fetch. *J. Phys. Oceanogr.*, **11**, 1505–1515.

Kahma, K. K., and Calkoen, C. J., 1992: Reconciling discrepancies in the observed growth of wind-generated waves. *J. Phys. Oceanogr.*, **22**, 1389–1405.

Kitaigordskii, S., Krasitskii, V., and Zaslavskii, M., 1975: On Phillips' theory of equilibrium range in the spectra of wind-generated gravity waves. *J. Phys. Oceanogr.*, **5**, 410–420.

Kitaigorodskii, S. A., 1962: Applicaitions of the theory of similarity to the analysis of wind-generated wave motion as a stochastic process. *Bull. Acad. Sci. USSR, Gorphys. Ser.*, **1**, 105–117.

Komen, G. J., Cavaleri, L., Donelan, M., Hasselmann, K., Hasselmann, S., and Janssen, P. A. E. M., 1994: *Dynamics and modelling of ocean waves*. Cambridge University Press, Cambridge.

Komen, G. J., Hasselmann, S., and Hasselmann, K., 1984: On the existence of a fully developed wind-sea spectrum. *J. Phys. Oceanogr.*, **14**, 1271–1285.

Krabill, W. B., and Martin, C. F., 1987: Aircraft positioning using global positioning carrier phase data. *Navig.*, **34**, 1–21.

Krabill, W. B., Thomas, R. H., Jezek, K., Kuivinen, C., and Manizade, S., 1995: Greenland ice sheet thickness changes measured by laser altimetry. *Geophys. Res. Lett.*, **22**, 2341–2344.

Krogstad, H. E., 1990: *Directional Ocean Wave Spectra*, chapter Reliability and resolution of directional wave spectra from heave, pitch, and roll data buoys, 66–71. Johns Hopkins University Press.

Large, W. G., and Pond, S., 1982: Sensible and latent heat flux measurements over the ocean. *J. Phys. Oceanogr.*, **12**, 464–482.

Lewis, A., and Allos, R., 1990: Jonswap's parameters: sorting out inconsistencies. *Ocean Eng.*, **17**, 409–415.

Long, C. E., and Resio, D. T., 2007: Wind wave spectral observations in Currituck Sound, North Carolina. *J. Geophys. Res.*, **112**(C05001), 21pp.

Melville, W. K., 1996: The role of surface-wave breaking in air-sea interaction. *Annu. Rev. Fluid Mech.*, **28**, 279–321.

Melville, W. K., and Matusov, P., 2002: Distribution of breaking waves at the ocean surface. *Nature*, **417**, 58–63.

Melville, W. K., Romero, L., and Kleiss, J. M., 2005: Extreme waves in the Gulf of Tehuantepec. In *14th 'Aha Huliko'a Hawaiian Winter Workshop: Rogue Waves*, editors P. Muller, and D. Henderson, 23–28. University of Hawaii at Manoa.

Miles, J. W., 1957: On the generation of surface waves by shear flow. *J. Fluid Mech.*, **3**, 185–204.

Mitsuyasu, H., 1981: Directional spectra of ocean waves in generation area. In *Proc. conf. on Directional Wave Spectra Applications*, 87–101. ASCE, New York.

Mitsuyasu, H., 2002: A historical note on the study of ocean surface waves. *Journal of Oceanography*, **58**, 109–120.

Mitsuyasu, H., Tasai, F., Suhara, T., Mizuno, S., Ohkusu, M., Honda, T., and Rikiishi, K., 1975: Observation of the directional wave spectra of ocean waves using a cloverleaf buoy. *J. Phys. Oceanogr.*, **5**, 750–760.

Onorato, M., Osborne, A. R., Serio, M., Resio, D., Pushkarev, A. N., Zakharov, V. E., and Brandini, C., 2002: Freely decaying weak turbulence for sea surface gravity waves. *Phys. Rev. Lett.*, **89**(14), 144501.

Perlin, N., Samelson, R. M., and Chelton, D. B., 2004: Scatterometer and model wind and wind stress in the oregonnorthern california. *Mon. Weather Rev.*, **132**, 2110–2129.

Phillips, O. M., 1958: The equilibrium range in the spectrum of wind-generated waves. *J. Fluid Mech.*, **4**, 426–433.

Phillips, O. M., 1977: *The Dynamics of the Upper Ocean.* Cambridge University Press.

Phillips, O. M., 1981: The dispersion of short wavelets in the presence of a dominant long wave. *J. Fluid Mech.*, **107**, 465–485.

Phillips, O. M., 1985: Spectral and statistical properties of the equilibrium range in wind-generated gravity waves. *J. Fluid Mech.*, **156**, 505–531.

Pierson, W., Jr, and Moskowitz, L., 1964: A proposed spectral form for fully-developed wind seas based on the similarity theory of S. A. Kitaigorodskii. *J. Geophys. Res.*, **69**, 5181–5190.

Plant, W. J., 1982: A relationship between wind stress and wave slope. *J. Geophys. Res.*, **87**, 1961–1967.

Pushkarev, A., Resio, D., and Zakharov, V., 2003: Weak turbulent approach to the wind-generated gravity sea waves. *Physica D*, **184**, 29–63.

Resio, D., and Perrie, W., 1991: A numerical study of nonlinear energy fluxes due to wave-wave interactions. part 1: Methodology and basic results. *J. Fluid Mech.*, **223**, 609–629.

Resio, D. T., Long, C., and Vincent, C., 2004: The equilibrium-range constant in wind-generated wave spectra. *J. Geophys. Res.*, **109**(CO1018).

Romero, L., and Melville, W. K., 2008a: Airborne observations of fetch-limited waves in the gulf of tehuantepec. *J. Phys. Oceanogr.*, In Preparation.

Romero, L., and Melville, W. K., 2008b: Numerical simulations of wind-wave spectra in the gulf of tehuantepec. *J. Phys. Oceanogr.*, In Preparation.

Romero-Centeno, R., Zavala-Hidalgo, J., Gallegos, A., and O'Brien, J., 2003: Isthmus of tehuantepec wind climatology and ENSO signal. *J. Climate*, **16**, 2628–2639.

Schule, J. J., Simpson, L. S., and DeLeonibus, P. S., 1971: A study of wave spectra with an airborne laser. *J. Geophys. Res.*, **76**, 4160–4171.

Schultz, D. M., Bracken, W. E., and Bosart, L. F., 1998: Planetary- and synoptic-scale signatures associated with central american cold surges. *Mon. Weather Rev.*, **126**, 5–27.

Smith, W. H. F., and Sandwell, D. T., 1997: Global seafloor topography from satellite altimetry and ship depth soundings. *Science*, **277**, 1957–1962.

Snyder, R. L., Dobson, F., Elliott, J., and Long, R. B., 1981: Array measurements of atmospheric pressure fluctuations above surface gravity waves. *J. Fluid Mech.*, **102**, 1–59.

Socquet-Juglard, H., Dysthe, K., Trulsen, K., Krodgstad, H. E., and Liu, J. D., 2005: Probability distributions of surface gravity waves during spectral changes. *J. Fluid Mech.*, **542**, 195–216.

Steenburgh, W. J., Schultz, D. M., and Colle, B. A., 1998: The structure and evolution of gap outflow over the Gulf of Tehuantepec, Mexico. *Monthly Weather Review*, **126**(10), 2673–2691.

Sverdrup, H. U., and Munk, W. H., 1947: Wind, sea, and swell: theory of relations for forecasting. Technical Report 601, U. S. Hydrographic Office.

TheWiseGroup, 2007: Wave modelling the state of the art. *Prog. Oceanog.*, **75**, 603–674.

Toba, Y., 1973: Local balance in the air-sea boundary process. *J. Oceanogr. Soc. Japan*, **29**, 209–220.

Tolman, H., and Chalikov, D., 1996: Source terms in a third-generation wind wave model. *J. Phys. Oceanogr.*, **26**, 2497–2518.

Tolman, H. L., 2002: User manual and system documentation of wavewatch-iii, version 2.22. *NOAA / NWS / NCEP / MMAB*, Technical Note 222, 133 pp.

Tracy, B. A., and Resio, D. T., 1982: Theory and calculation of the nonlinear energy transfer between sea waves in deep water. Technical Report 11, U.S. Army Engineer Waterways Experiment Station, Vicksburg, U.S.A.

Vledder, G. P. V., 2006: The WRT method for the computation of non-linear four-wave interactions in discrete spectral wave models. *Coastal Eng.*, **53**, 223–242.

Walsh, E. J., Hancock, D. W., Hines, D. E., Swift, R. N., and Scott, J. F., 1985: Directional wave spectra measured with the surface contour radar. *J. Phys. Oceanogr.*, **15**, 566–592.

Wang, D. W., and Hwang, P. A., 2001: Evolution of the bimodal directional distribution of ocean waves. *J. Phys. Oceanogr.*, **31**, 1200–1221.

Webb, D., 1978: Non-linear transfers between sea waves. *Deep Sea Res.*, **25**, 279–298.

Wu, J., 1982: Wind-stress coefficients over sea surface from breeze to hurricane. *J. Geophys. Res.*, **87**, 9704–9706.

Wyatt, L. R., 1995: The effect of fetch on the directional spectrum of celtic sea storm waves. *J. Phys. Oceanogr.*, **25**, 1550–1559.

Yan, L., 1987: An improved wind input source term for third generation ocean wave modelling. *Royal Netherlands Meteorological Institute Scientific Rep.*, **WR-87-9**, pp. 10.

Young, I. R., 1995: The determination of confidence limits associated with estimtes of the spectral peak frequency. *Ocean Eng.*, **22**(7), 669–686.

Young, I. R., 1998: An experimental investigation of the role of atmospheric stability in wind wave growth. *Coastal Eng.*, **34**, 23–33.

Young, I. R., 1999: *Wind generated ocean waves*. Elsevier Science, Oxford.

Young, I. R., Hasselmann, S., and Hasselmann, K., 1987: Computations of the response of a wave spectrum to a sudden change in wind direction. *J. Phys. Oceanogr.*, **17**, 1317–1338.

Young, I. R., Verhagen, L. A., and Banner, M. L., 1995: A note on the bimodal directional spreading of fetch-limited wind waves. *J. Geophys. Res.*, **100**, 773–778.

Young, I. R., and Vledder, G. P. V., 1993: A review of the central role of nonlinear interactions in wind-wave evolution. *Phil. Trans. Roy. Soc. London A*, **342**, 505–524.

Zakharov, V. E., and Filonenko, N. N., 1967: Energy spectrum for stochastic oscillations of the surface of a liquid. *Soviet Phys. Dokl.*, **11**, 881–883.